SAPIENZA
UNIVERSITÀ DI ROMA

Development of Passive Bistatic Radars based on Orthogonal Frequency-Division Multiplexing modulated signals for short and medium range surveillance

Facoltà di Ingegneria dell'Informazione, Informatica e Statistica

Dottorato di Ricerca in Telerilevamento

XXVIII Ciclo

Candidato

Claudio Palmarini

1151374

Tutor

Prof. Pierfrancesco Lombardo

INDEX

1 INTRODUCTION

In the last years the interest in passive bistatic radar (PBR) for surveillance purposes has significantly grown up for the potential role it could play in both civilian and military applications ([1]-[3]). PBR exploits an existing transmitter as an illuminator of opportunity; thus it is characterized by low environmental impact and is well suited for covert operation. In fact, it can be regarded as 'invisible' system catching extremely weak signals that are usually 'invisible' to the ordinary users of the employed transmitter.

Numerous transmitters for telecommunications, radio navigation and remote sensing applications can be used as sources of opportunity; however among them broadcast transmitters represent some of the most attractive choices for surveillance purposes owing to their excellent coverage ([4] -[10]).

Table 1 summarizes the main characteristics of several waveforms of opportunity for surveillance at short, medium and long range that are: frequency modulated (FM) radio, Digital Audio Broadcasting (DAB) and Digital Video Broadcasting – Terrestrial (DVB-T).

Table 1 Broadcast signals of opportunity for long and medium range surveillance applications.

Waveform	Bandwidth [MHz]	Channel Bandwidth [MHz]	Range Resolution	Doppler resolution	Surveillance application	Targets
FM	88÷108	0.2	Poor	Very Good	Long Medium	Aircrafts
DAB	174÷240	1.5	Good	Good	Medium Short	Aircrafts Boats
DVB-T	474÷858	8	Very Good	Good	Long Medium Short	Aircrafts Boats

Due to the high power of analogue transmissions, an FM radio based PBR is able to achieve detection ranges up to 150 kilometres. Digital waveforms of opportunity provide limited detection range; however, their higher bandwidth guarantees a finer range resolution (tens of meters against about 1-2 kilometres provided by FM radio). Finally, target Doppler discrimination capability is related to the maximum coherent processing interval that could be processed without experiencing a range cell migration for the target of interest; thus it depends on the maximum targets' speed and on the extension of the range cell. As a consequence the limited range resolution provided by FM radio allow to obtain very good Doppler resolution.

As shown in Figure 1, PRB system involves the utilization of at least two receiving antennas: one directive antenna (surveillance antenna) steered toward the area of interest collecting the low target echo and an auxiliary antenna (the reference one) which is steered toward the transmitter in order to collect the unknown transmitted signal.

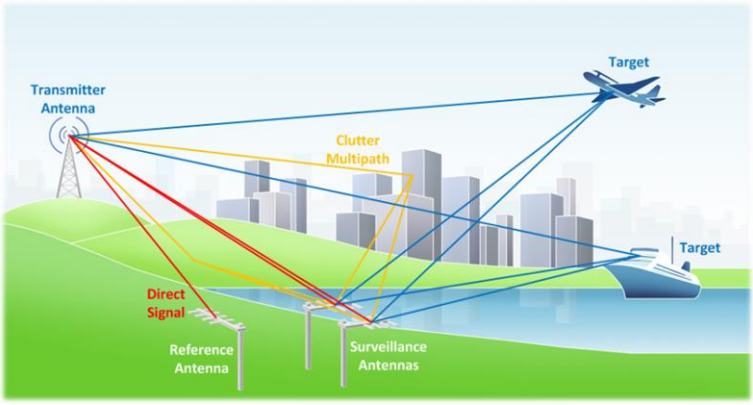

Figure 1 PBR antennas configuration.

The signal collected at the reference channel is typically used to remove undesired contributions received together with the moving target echo on the surveillance channel. Such disturbances result from direct signal breakthrough (e.g. fraction of the direct signal coming from the transmitter and received by the sidelobes or backlobes of the surveillance antenna) as well as strong clutter/multipath echoes. After the cancellation stage, the detection process is based on the evaluation of the bistatic two-dimensional (range-velocity) cross-correlation function (2D-CCF) – or equivalently the bistatic Range-Doppler map (RDM) – between the surveillance and the reference signal. A constant false alarm rate (CFAR) threshold can be then applied on the obtained map to automatically detect the potential targets according to a specific CFAR detection scheme. Increasing the number of surveillance antennas, one is able to perform target localization in the dimension along which the antennas are aligned (e.g. azimuth or elevation).

The main activity conducted during the research activity is the development of PBR systems based on OFDM signals of opportunity. In particular, a DAB based PBR for air traffic control (ATC) applications and a DVB-T based PBR for maritime surveillance have been objects of study.

Section 2 is dedicated to the description of the exploited waveforms of opportunity. In particular, the transmission standards will be presented and some considerations about their usage for radar purposes will be provided.

Section 3 describes in detail the signal processing chain of a DVB-T based PBR for quasi real-time maritime surveillance. For each block of the chain, state of the art of existing algorithm and the work conducted to improve performance is presented. DVB-T signal is only recently exploited for maritime surveillance; prior to it, transmitters of the GSM mobile network have been largely used as they were proved to have nice tracking capability of small and fast boats at short ranges ([11]-[13]). Aiming at increasing the range coverage, transmission of DVB-T signals represents one of the most attractive choice. Although preliminary results have been presented ([14]-[16]), many aspects related to the problematics of maritime surveillance need to be addressed yet. Those are:

(i) low speed of the targets,

(ii) the possibility of having close targets with very high difference in radar cross sections,

(iii) sea clutter and multipath.

For the purpose a great effort has been devoted to develop effective disturbance cancellation techniques able to enhance the system's detection capability. Equally important is the capacity of the system in localizing targets with high accuracy; as a consequence, a theoretical analysis has been conducted in order to obtain high accuracy direction of arrival estimation in a wide angular sector exploiting few receiving elements.

Furthermore, real time surveillance is a rather tricky feature as the wide band associated with DVB-T transmission results in a very high computational load. This aspect becomes a growing need with the introduction of novel signal processing techniques ([17]-[18]) trying to increase systems' reliability (e.g. multiple receiving channels simultaneously collecting and processing multiple signals received at different frequencies or receivers could be exploited).

In Section 4, a DAB based experimental setup for ATC applications is presented. Such system was entirely designed and fielded at DIET department thus a detailed description of the receiver analogue front-end and of the acquisition board is provided prior to the discuss the experimental results. In ([19]-[22]), potentialities of several prototypes developed by other research groups have been demonstrated. DAB signal is shown to provide good detection capability for targets at up to 30 km from the receiver. However, those systems did not show good detection continuity as very short acquisitions have been considered. During the research activity special care has been given to the configuration of the acquisition board in order to perform very long acquisitions of up to four frequencies for up to four receiving antennas. Obtained results showed the potentialities of the system in obtaining very good detection continuity at up to 40/50 monostatic kilometres from the receiver thus increasing ambitions of DAB based PBR for ATC applications.

Finally, in Section 5 the conclusions are drawn.

2 EXPLOITED SIGNALS OF OPPORTUNITY

A brief introduction of the exploited OFDM signals of opportunity is appropriate as the achievable performance of a passive radar greatly depends on the characteristics of the signals that are not under the control of the radar operator.

Orthogonal frequency division modulation (OFDM) is a digital modulation format that has been adopted for a number of broadcast standards. It has been developed in order to overcome the main limitations concerning analog transmission systems such as the medium-related severe quality problems and the low spectral efficiency. Thanks to the higher efficiency achievable with a digital transmission, a remarkable transmitting power reduction is possible. Digital Video Broadcast (DVB), Digital Audio Broadcast (DAB), Digital Radio Mondiale and Wi-Fi (802.11a, 802.11n, 802.11ac and more) are all OFDM based standards.

The main advantage of such systems relies on the higher robustness against distortions introduced by the propagation medium. In traditional modulating systems, i.e. those exploiting a single carrier, it may happen that the transfer function of the medium significantly varies within the modulated signal bandwidth; this may cause severe inter-symbol interference and thus the need for a proper equalization. OFDM consists in parallelizing the data to be transmitted on a number of closely spaced modulated carriers, thus even though the transmission medium still produces linear distortions, the reduced bandwidth of each modulator entails a reduced distortion that may be so low that it does not require an equalization stage.

In 2.1 some details about OFDM modulation are given prior to describe the transmission standard of DVB (2.2) and DAB (2.3). Finally a more radar related aspect is investigated in 2.4, aiming at understanding the potentialities as well as the weaknesses of such signals when used for radar detection purposes.

2.1 OFDM MODULATION

OFDM consists in a digital multi-carrier modulation scheme based on the transmission of the content using multiple subcarriers rather than a single subcarrier modulation. Rather than transmit a high rate stream of data with a single carrier, OFDM exploits a large number of closely spaced orthogonal subcarriers that are simultaneously transmitted.

OFDM is based on the well-known technique of Frequency Division Multiplexing (FDM). In FDM different streams of information are mapped onto separate parallel frequency channels. A frequency guard band is introduced between adjacent channels in order to reduce interference among them. In an OFDM system, the sub-carrier frequencies are chosen in a way that they result to be orthogonal to each other and thus inter-carrier guard bands are no longer needed. This greatly simplifies the design of the transmitting and receiving parts of the communication system as a separate filter for each sub-channel is not required.

Figure 2 illustrates the main concepts of an OFDM signal and the inter-relationship between the frequency and time domains ([23]). In the frequency domain, multiple adjacent subcarriers are each independently modulated with complex data. An Inverse FFT transform is performed on the frequency domain subcarriers to produce the OFDM symbol in the time domain. Then in the time domain, guard intervals are inserted between each of the symbols. Multiple symbols are concatenated to obtain the final OFDM burst signal. At the receiver an FFT is performed on the OFDM symbols to recover the original data bits.

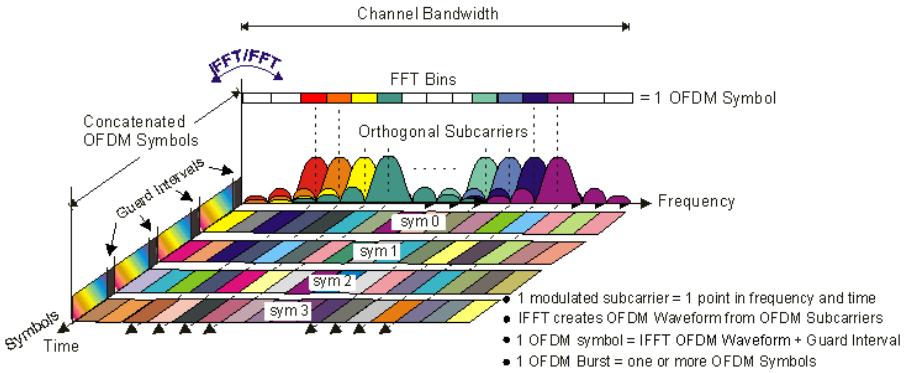

Figure 2 Frequency-Time representative of an OFDM signal.

OFDM requires very accurate frequency synchronization between the transmitter and the receiver as a frequency deviation compromises the sub-carriers' orthogonality, causing inter-carrier interference (ICI). Frequency offsets are typically due to mismatched transmitter and receiver oscillators or by Doppler shift due to movement.

Guard intervals are inserted at the beginning of each OFDM symbol to prevent inter-symbol interference at the receiver caused by multipath delay spread in the radio channel. With the term multipath one indicates the situation in which signals travel from the transmitter to the receiver by more than one path. Whether those paths have different lengths, their contributions arrive at the receiver with different delays, and obviously with different amplitudes. As a result, the direct symbol, at the receiver site, is affected both in amplitude and phase by an amount that depends on the time difference between the paths. It is possible to overcome such problem by inserting a guard interval between adjacent useful symbol. Such interval should be chosen large enough to not have reflections arriving at the receiver with a delay greater than the interval itself, or at least they arrive with such low amplitudes that no effect is experienced on the amplitude and phase of the resulting received symbol. Thus longer guard interval durations allow more distant echoes to be tolerated, but they also reduce the channel efficiency.

It is worth nothing that a long guard interval may prevent the interference of a given symbol on the next one, however it cannot prevent the possible amplitude and phase alteration of the received symbols. To deal with this, a regular pattern going under the name of *Pilot symbols* (in DVB standard) or *Reference symbol* (in DAB standard) is usually inserted in the transmitted stream. This pattern also helps the receiver to understand what amplitude or phase corresponds to a given symbol.

2.2 DVB-T SIGNAL CHARACTERISTICS

DVB-T refers to a technical standard that specifies the framing structures, channel coding and modulation for digital terrestrial television (DTT) broadcasting, [24]. DVB-T is a flexible system that allows networks to be designed for the delivery of a wide range of services, from HD (high definition) TV to multichannel SD (standard definition) TV, fixed, portable, mobile and even handheld reception. The DVB Project, which developed the first version of the standard, has now created a next generation terrestrial specification, DVB-T2, designed to meet the needs of countries after they have completed the Analogue Switch-Off.

DVB-T has technical characteristics that make it a very flexible system:

- 3 modulation options (QPSK, 16QAM, 64QAM)
- 5 different FEC (forward error correction) rates
- 4 Guard Interval options
- Choice of 2k or 8k carriers
- Possibility to operate in 6, 7 or 8 MHz channel bandwidths.

Using different combinations of the above parameters a DVB-T network can be designed to match the requirements of the network operator, finding the optimal balance between robustness and capacity.

The flexible size of the guard interval has been adopted to allow optimal trade-off between network topology and frequency efficiency. This will enable the system to support different network configurations, such as large area SFN and single transmitter, while keeping maximum frequency efficiency.

The DVB-T signal exploits an OFDM modulation whose main parameters are listed in Table 2 for typical 8 MHz channels, distinguishing between the 2k mode and 8k mode specifications. The 2k mode is suitable for single transmitter operation and for small SFN networks with limited transmitter distances. The 8k mode can be used both for single transmitter operation and for small and large SFN networks. Exclusively for use in DVB-H (DVB-Handheld) systems, a third transmission mode – the 4k mode – is defined; it aims to offer an additional degree of flexibility for DVB-H network planning.

Table 2 Main parameters of 2k and 8k modes DVB-T signals.

Parameter		*2k mode*	*8k mode*
Number of subcarriers		1705	6817
Useful symbol duration	T_u	224 μs	896 μs
Guard interval T_g	$T_u/32$	7 μs	28 μs
	$T_u/16$	14 μs	56 μs
	$T_u/8$	28 μs	112 μs
	$T_u/4$	56 μs	224 μs
Bandwidth		7.61 MHz	7.61 MHz

The system allows different levels of QAM modulation and different inner code rates to be used to trade bit rate versus ruggedness. The system also allows two level hierarchical channel coding and modulation, including uniform and multi-resolution constellation. In this case the functional block diagram of the system shall be expanded to include the modules shown dashed in Figure 3. Two independent MPEG transport streams, referred to as the high-priority and the low-priority stream, are mapped onto the signal constellation by the Mapper and the Modulator which therefore has a corresponding number of inputs.

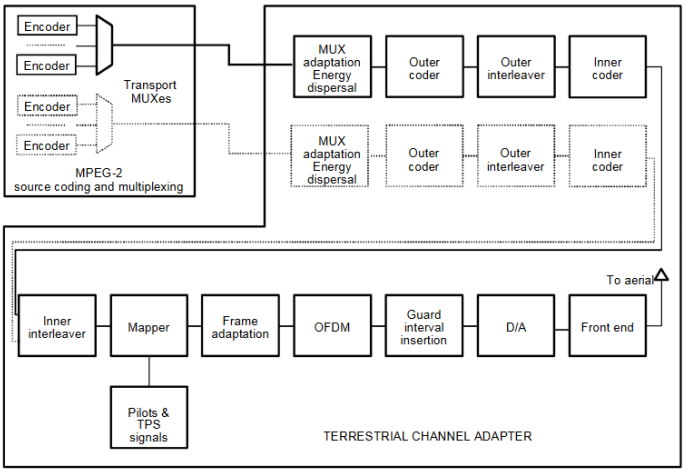

Figure 3 Functional block diagram of the DVB system.

As the multiplexing and coding processes lie do not have impact on the performance of a radar system based on such radar, no further details will be provided about them. In contrast some words are spent on some of the blocks shown in the lower row of the block diagram in Figure 3.

As already said, OFDM modulation consists in modulating the data stream over a number of evenly spaced orthogonal subcarrier frequencies, contemporaneously transmitted for a time interval equal to T_u. A guard interval of duration T_g is inserted by cyclically extending each OFDM symbol so the total symbol duration is equal to $T_s = T_u + T_g$. The subcarriers are separated by $\Delta f = 1/T_u$ and the number of sub-carriers depends upon the considered mode. However, the above parameters are scaled so that the subcarriers span the 7.61 MHz bandwidth allocated to the DVB-T channel. The DVB-T signal structure is organized in frames with each frame consisting of 68 OFDM symbols. Four frames constitute one super-frame. Each symbol is constituted by a set of $K = 6817$ carriers in the 8k mode and $K = 1705$ carriers in the 2k mode. The carriers are indexed by $k \in [K_{\min}, K_{\max}]$ and determined by $K_{\min} = 0$ and $K_{\max} = 1704$ in 2k mode and 6816 in 8k mode respectively.

The emitted signal is described by the following expression:

$$s(t) = \mathrm{Re}\left\{ e^{j2\pi f_c t} \sum_{m=0}^{\infty} \sum_{l=0}^{67} \sum_{k=K_{\min}}^{K_{\max}} c_{m,l,k} \cdot \psi_{m,l,k}(t) \right\} \tag{1}$$

where:

$$\psi_{m,l,k}(t) = \begin{cases} e^{j2\pi \frac{k'}{T_u}(t - \Delta - l \cdot T_s - 68 \cdot m \cdot T_s)} & (l + 68 \cdot m) \cdot T_s \leq t \geq (l + 68 \cdot m + 1) \cdot T_s \\ 0 & else \end{cases} \tag{2}$$

where:

- k denotes the carrier number;
- l denotes the OFDM symbol number;
- m denotes the transmission frame number;
- K is the number of transmitted carriers;
- T_s is the symbol duration;
- T_u is the inverse of the carrier spacing;
- Δ is the duration of the guard interval;
- f_c is the central frequency of the RF signal;
- k' is the carrier index relative to the center frequency, $k' = k - (K_{\max} + K_{\min}) / 2$;
- $c_{m,0,k}$ is the complex symbol for carrier k of the Data symbol no. 1 in frame number m;
- $c_{m,1,k}$ is the complex symbol for carrier k of the Data symbol no. 2 in frame number m;
- …
- $c_{m,67,k}$ is the complex symbol for carrier k of the Data symbol no. 68 in frame number m.

In addition to the data carriers, the DVB-T signal contains pilot carriers and transport parameter signaling (TPS) carriers, which are used for receiver synchronization, channel estimation and system parameters transmission. To this aim, the pilots carriers are transmitted at boosted power level $E_P = 16/9$ while the power level of data carriers and TPS pilots is normalized to 1. The pilot and TPS carriers are scattered at given frequencies, and according to a known rule. Each continual pilot coincides with a scattered pilot every fourth symbol; the number of useful data carriers is constant from symbol to symbol. For the symbol of index 1 (ranging from 0 to 67), carriers for which index k belongs to the subset $\{k = K_{\min} + 3 \cdot (l \bmod 4) + 12p \mid p \text{ integer}, p \geq 0, k \in [K_{\min}, K_{\max}]\}$ are scattered pilots. Where p is an integer that takes all possible values greater than or equal to zero, provided that the resulting value for k does not exceed the valid range $[K_{\min}, K_{\max}]$.

The pilot insertion patter is shown in Figure 4.

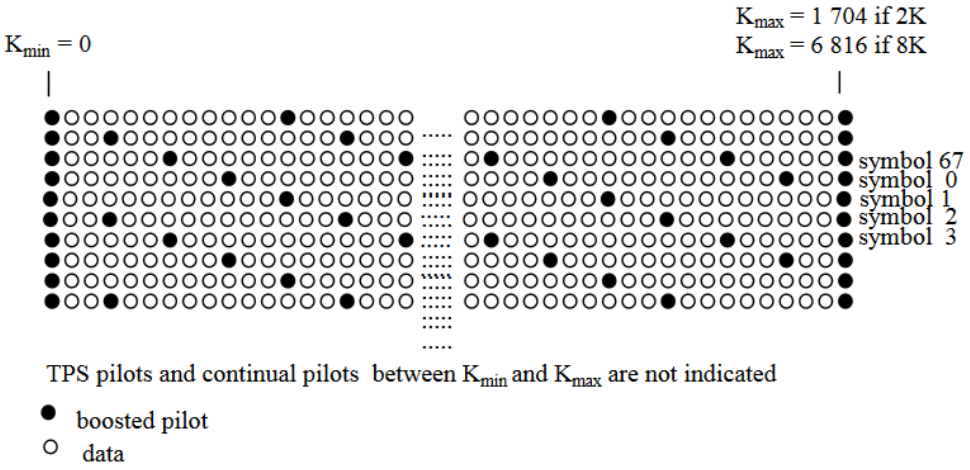

Figure 4 Frame structure.

In addition to the scattered pilots described above, 177 continual pilots in the 8k mode and 45 in the 2k mode, are inserted according to the following table.

Continual pilot carrier positions (index number k)														
2K mode							8K mode							
0	48	54	87	141	156	192	0	48	54	87	141	156	192
201	255	279	282	333	432	450	201	255	279	282	333	432	450
483	525	531	618	636	714	759	483	525	531	618	636	714	759
765	780	804	873	888	918	939	765	780	804	873	888	918	939
942	969	984	1 050	1 101	1 107	1 110	942	969	984	1 050	1 101	1 107	1 110
1 137	1 140	1 146	1 206	1 269	1 323	1 377	1 137	1 140	1 146	1 206	1 269	1 323	1 377
1 491	1 683	1 704					1 491	1 683	1 704	1 752	1 758	1 791	1 845
							1 860	1 896	1 905	1 959	1 983	1 986	2 037
							2 136	2 154	2 187	2 229	2 235	2 322	2 340
							2 418	2 463	2 469	2 484	2 508	2 577	2 592
							2 622	2 643	2 646	2 673	2 688	2 754	2 805
							2 811	2 814	2 841	2 844	2 850	2 910	2 973
							3 027	3 081	3 195	3 387	3 408	3 456	3 462
							3 495	3 549	3 564	3 600	3 609	3 663	3 687
							3 690	3 741	3 840	3 858	3 891	3 933	3 939
							4 026	4 044	4 122	4 167	4 173	4 188	4 212
							4 281	4 296	4 326	4 347	4 350	4 377	4 392
							4 458	4 509	4 515	4 518	4 545	4 548	4 554
							4 614	4 677	4 731	4 785	4 899	5 091	5 112
							5 160	5 166	5 199	5 253	5 268	5 304	5 313
							5 367	5 391	5 394	5 445	5 544	5 562	5 595
							5 637	5 643	5 730	5 748	5 826	5 871	5 877
							5 892	5 916	5 985	6 000	6 030	6 051	6 054
							6 081	6 096	6 162	6 213	6 219	6 222	6 249
							6 252	6 258	6 318	6 381	6 435	6 489	6 603
							6 795	6 816					

The TPS carriers are used for the purpose of signaling parameters related to the transmission scheme, i.e. to channel coding and modulation. The TPS is transmitted in parallel on 17 TPS carriers for the 2k mode and on 68 carriers for the 8k mode. Every TPS carrier in the same symbol conveys the same differentially encoded information bit. In the following is reported the list of the carriers for the two transmission modes.

2K mode					8K mode							
34	50	209	346	413	34	50	209	346	413	569	595	688
569	595	688	790	901	790	901	1 073	1 219	1 262	1 286	1 469	1 594
1 073	1 219	1 262	1 286	1 469	1 687	1 738	1 754	1 913	2 050	2 117	2 273	2 299
1 594	1 687				2 392	2 494	2 605	2 777	2 923	2 966	2 990	3 173
					3 298	3 391	3 442	3 458	3 617	3 754	3 821	3 977
					4 003	4 096	4 198	4 309	4 481	4 627	4 670	4 694
					4 877	5 002	5 095	5 146	5 162	5 321	5 458	5 525
					5 681	5 707	5 800	5 902	6 013	6 185	6 331	6 374
					6 398	6 581	6 706	6 799				

As it will be shown in 3.3, such fixed pattern will cause the occurrence of unwanted structures in the ambiguity function of the signal and proper technique able to remove such structures need to be used in order to fully exploit the potentialities of such waveform in radar purposes.

2.3 DAB SIGNAL CHARACTERISTICS

DAB is a digital radio technology for broadcasting radio stations ([25]). Its objective is to deliver high-quality digital audio programs and data services for mobile, portable and fixed reception from terrestrial or satellite transmitters. DAB channels have been allocated in the VHF and UHF frequency bands. Its system is designed to provide spectrum and power efficient techniques in terrestrial transmitter network planning, known as the Single Frequency Network (SFN) and the gap-filling technique.

Figure 5 reports the conceptual block diagram of the emission part of the DAB system. Data are transported recurring to two mechanisms: Fast Information Channel (FIC) and Main Service Channel (MSC). The primary function of the FIC is to carry control information necessary to interpret the configuration of the MSC. The essential part of this control information is the Multiplex Configuration Information (MCI), which contains information on the multiplex structure and, when necessary, its re-configuration. In order to allow a rapid and safe response to the MCI, the FIC is transmitted without time interleaving, but with a high level of protection against transmission errors. On the other hand the MSC, which is used to carry audio and data service components, is scrambled and time-interleaved before being multiplexed.

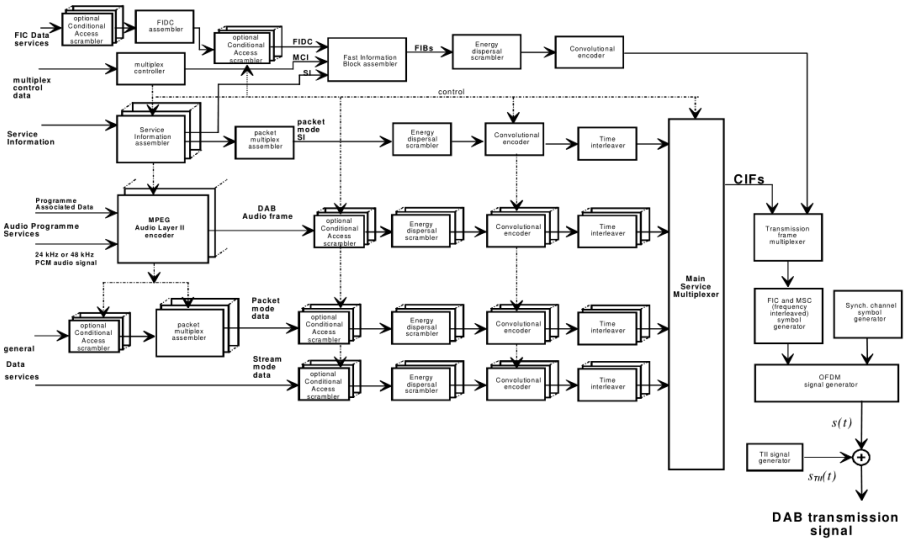

Figure 5 Conceptual DAB emission block diagram.

The transmission frame multiplexer combines the outputs of FIC and MSC, called Fast Information Blocks (FIBs) and Common Interleaved Frames (CIFs), respectively. Those are used to generate OFDM symbols which length and organization is a function of the transmission mode. In fact, to allow the DAB system to be used in different transmission network configurations and over a wide range of operating frequencies, four transmission modes have been defined. The transmitted signal has a frame structure of 96 ms duration (Transmission mode I), 24 ms (Transmission modes II and III) and 48 ms (Transmission mode IV). Table 3 reports the characteristics of the transmission frame for each transmission mode.

Table 3 General transport characteristics of the transmission frame.

Transmission Mode	Frame duration	FIBs/frame	CIFs/frame
I	96 ms	12	4
II	24 ms	3	1
III	24 ms	4	1
IV	48 ms	6	2

The generation of the OFDM signals involves the processes of Differential Quadrature Phase Shift Keying (D-QPSK), frequency interleaving, and D-QPSK symbols frequency multiplexing (OFDM generator).

The transmission frame consists of a sequence of three groups of OFDM symbols: synchronization channel symbols, Fast Information Channel symbols and Main Service Channel symbols. The synchronization channel symbols comprise the null symbol and the phase reference symbol. The null symbols are also used to allow a limited number of OFDM carriers to convey the Transmitter Identification Information (TII).

The first OFDM symbol of the transmission frame is the Null symbol of duration T_{NULL}. The remaining part of the transmission frames is composed by the juxtaposition of OFDM symbols of duration T_S. Each of these OFDM symbols consist of a set of equally spaced carriers with a carrier spacing equal to $1/T_u$. The main signal $s(t)$ is defined as:

$$s(t) = \mathrm{Re}\left\{ e^{j2\pi f_c t} \sum_{m=-\infty}^{+\infty} \sum_{l=0}^{L} \sum_{k=-K/2}^{K/2} z_{m,l,k} \cdot g_{k,l}(t - m\,T_F - T_{NULL} - (l-1)\,T_S) \right\} \tag{3}$$

with

$$g_{k,l}(t) = \begin{cases} 0 & \text{for } l = 0 \\ e^{j2\pi \frac{k}{T_u}(t-\Delta)} & \text{for } l = 1,2,\ldots,L \end{cases} \tag{4}$$

and $T_S = T_U + \Delta$.

The various parameters and variables are defined as follows:

- L is the number of OFDM symbols per transmission frame (the Null symbol being excluded);
- K is the number of transmitted carriers;
- T_F is the transmission frame duration;
- T_{NULL} is the Null symbol duration;
- T_s is the symbol duration;
- T_u is the inverse of the carrier spacing;
- Δ is the duration of the guard interval;
- f_c is the central frequency of the RF signal;
- $z_{m,l,k}$ is the complex D-QPSK symbol associated to carrier k of OFDM symbol l in transmission frame m. Their values are defined in [25]. For $k = 0$, $z_{m,l,k} = 0$ so that the central carrier is not transmitted.
- f_c is the central frequency of the signal.

These parameters are specified in the Table 4 for transmission modes I, II, III and IV. The values of the various time-related parameters are given in multiplies of the elementary period $T = 1/2'048'000$ seconds.

Table 4 DAB signal parameters.

Parameter	Transmission mode			
	I	II	III	IV
L	76	76	153	76
K	1536	384	192	768
T_F	196 608 T	49 152 T	49 152 T	98 304 T
T_{NULL}	2 656 T	664 T	345 T	1 328 T
T_S	2 552 T	638 T	319 T	1 276 T
T_u	2 048 T	512 T	256 T	1 024 T
Δ	504 T	126 T	63 T	252 T

2.3.1 DAB IN ITALY

Figure 6 shows the diffusion of DAB over the entire world up to 2012. Dark blue countries benefit of regular services, while dark purple ones are testing the transmissions. Lavender countries have just shown interest in such service while light yellow indicates countries no longer using DAB.

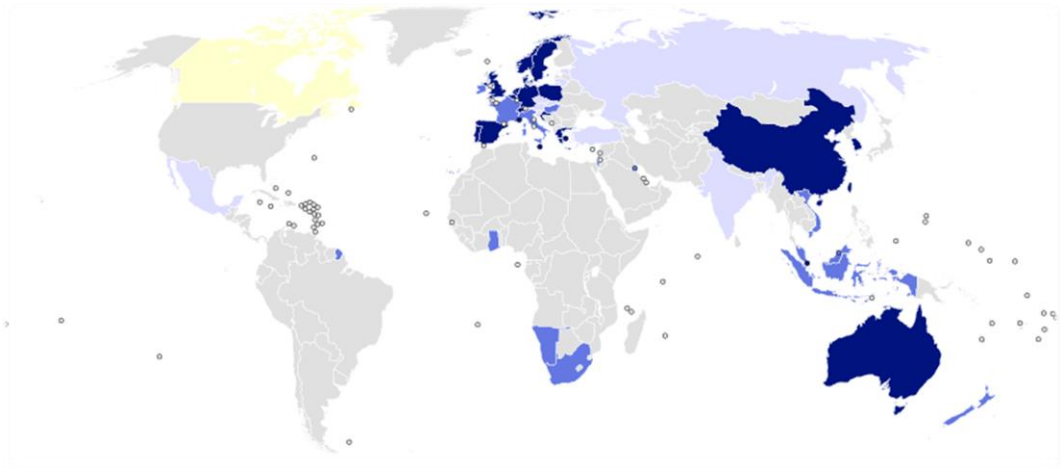

Figure 6 Diffusion of DAB in the world (last update 2012). Dark blue: Countries with regular services, Dark purple: Countries with trials/tests, Lavender: Countries with interest, Light yellow: DAB no longer used.

As in 2012, Italy is still testing DAB transmission with the exception of some regions. The main stages of DAB transmission introduction in our country can be summarized in the following key dates:

- 1992. For the first time in Italy, the DAB system is presented at "*Conferenza Internazionale IBTS '92*" by "Centro Ricerche Rai di Torino".
- 1995. Three synchronized transmitters operating in the same frequency (Band III, channel H2) start operating in Valle d'Aosta. They have been installed at the RAI's transmitting center of St. Vincent, Gerdaz and Blavy. During the experimentation of the DAB service on different routes (highway, urban and mountain environment), it were simultaneously recorded by a moving equipped car the FM, DAB and video image of the route: the result is an

audiovisual contribution that has been presented in May '95 at the Radio Expo held in Bologna and in November at the Radio exhibition held in Rome. In July, RAI participated at the Wiesbaden Conference CEPT where the frequency allotment for the DAB service have been defined.

- 1996. The same audiovisual contribution is also presented at the Third DAB Symposium held in Montreux in June. A fourth transmitter is switched on at Col de Courtil. The four DAB transmitter network covers Aosta, the A5 highway, large areas adjacent to it and the coverage is extended to the town of Ivrea in Piemonte. In June, the results of the experimentation are collected in a technical report which is then presented to the Ministry of Communications: they confirm the excellent performance of DAB in terms of sound quality and availability even in case of mobile reception; in addition they provide guidelines for future service planning in the national context. In September, during the Venice Film Festival a diffusion system located in Compalto is activated allowing the listening of the broadcasted programs at the Technology pavilion of the Venice's Lido.
- 1997. In Milan, during SMAU '97 a demonstration of a DAB experimental system is performed; it allows to listen several RAI radio programs at the stand of exhibition. In agreement with the Ministry of Communications, it is established in Turin a collaboration between RAI and the private Club DAB Italia for an additional experimentation of DAB transmissions in the cities of Turin and Milan with the objective of creating optimal conditions for the introduction of the service. DAB service introduction in Bolzano's area allows to cover Brennero's highway.
- 1998. In May 25 transmitters in Andrate and Torino Eremo come into operation. In October 14 a transmitter is activated in Milano. On the same day it is also activated the Club DAB Italia's transmitter hosted at the transmitting centre "Ponti Fissi" in Milano. A total audience of about 4 million listeners is estimated (representing almost 10% of the Italian population).

RAI has been appointed by the Ministry of Communications to extend, from 1999 onwards, the DAB service aiming at cover about 60% of the Italian population. Regular services in Italy started December 2012 in the Trentino region following a decree by AGCOM published in May 2012 assigning one block for national public radio and two blocks for national commercial (12A, 12B and 12C) and additional blocks for local services (12D, 10A, 10B 10C and 10D).

Currently the Department of Communications released the licenses to the private national operator Club DAB Italia and to local consortia DTTAA and Digiloc for the Trentino area. The standard adopted for digital radio receivers in Italy, developed by the Associazione per la Radiofonia Digitale in Italia (ARD) includes WorldDMB Profile 1, FM with RDS, Band III and L Band. The receiver certification website www.arditalia.it was launched in 2010 and has been developed in collaboration with broadcasters, network operators and receiver manufacturers. It provides guidance so that receivers certified in Italy work everywhere in Europe. There are three trial national multiplexes, three regular regional multiplexes and six trial regional multiplexes on air broadcasting a total of 20 DAB+ simulcast services, 4 DAB+ exclusive services, one DMB exclusive service and one exclusive Data service.

Acquisition campaigns of DAB signals have all been held in Rome were DAB transmissions are still under test. At the date of the acquisitions (2013), six DAB channels were transmitted in the III Band VHF (very high frequency) of the electromagnetic spectrum. A list of the channels, with their carrier frequencies, and a capture of the spectrum is reported in Figure 7.

Canale	f [MHz]
7B	190,640
12A	223,936
12B	225,648
12C	227,360
12D	229,072
13F	239,200

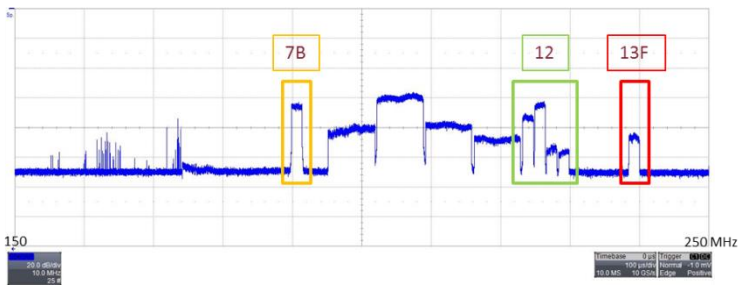

Figure 7 List of DAB channels transmitted in Rome at the time of acquisitions (2013).

2.4 OFDM MODULATED SIGNALS AS OPPORTUNITY SIGNALS

In this section, DVB-T and DAB signals will be investigated in terms of ambiguity function characteristics. In addition, a comparison against an extensively used signal for medium/long range surveillance is provided: the FM radio signal. This comparison allows to better highlight the differences between digital and analogic signals.

Performance of a PBR system highly depends on the kind of exploited waveform. Indeed, the PBR capability to distinguish close targets in the range dimension is determined by the bandwidth of the waveform of opportunity. The dimension of the range resolution cell indirectly affects the Doppler resolution; in fact, depending on its size and on the expected speed of the targets of interest, a narrow range cell implies an upper bound on the achievable Doppler resolution cell in order to avoid range cell migration during the coherent processing interval (CPI).

The most widely used waveforms of opportunity for target detection and localization at short, medium and long range are the FM radio, DVB-T and DAB signals. In the literature many contributions may be found regarding their exploitation.

FM radio signals are especially attractive for the generally high level of transmitted power which offers wide coverage. DVB-T and DAB signals are characterized by wide coverage and wider bandwidth than FM signals. As is known, the wider the bandwidth the better the range resolution. FM signals however are characterized by better Doppler resolution.

In [26] an interesting comparison in terms of ambiguity function is presented for those signals. It has been shown that the ambiguity behavior of FM signals, as well as other analog modulation formats, highly depends on the instantaneous program content. This has been confirmed against experimental data sets by our research group that developed an experimental setup for air traffic control applications ([27]). Experimental results have shown that the detection performance of an FM based PBR are highly affected by the time varying characteristics of both the transmitted waveform and the propagation channel conditions. To make the detection scheme robust with respect to those issues and to possibly improve the localization capability of the system, multichannel processing solutions have been proposed. In particular, the potential advantages yielded by the joint exploitation of multiple receiving channels collecting signals at received at different frequencies, different polarizations or properly displaced antenna elements have been addressed ([17],[18]).

DVB-T and DAB signals are characterized by a much more stable behavior; indeed, their ambiguity function does not depend on the transmitted content. In Figure 8 it is possible to compare the ambiguity functions of (a) radio FM transmission broadcasting jazz music at 102.2 MHz, (b) DAB signal at 222.4 MHz and (c) DVB-T signal at 505 MHz.

Ambiguity functions of the latter two signals are much more favorable in terms of mainlobe shape and sidelobe level. Indeed, they provide a better approximation of the ideal ‘thumbtack’ form. This can be expected because those signals, coded with OFDM modulation, are subjected to a randomization process in order to gain robustness against burst errors. However, to allow the receiver to adequately restore the original transmission, some periodic structures are inserted within the signal. As will be seen, those structures may be an impediment on target detection. Therefore, the following two paragraphs are devoted to briefly describe the main characteristics of those signals.

In 2.2 the main characteristics of the DVB-T signal are presented and their impact on the ambiguity function will be shown. DAB signal characteristics are addressed in 2.3.

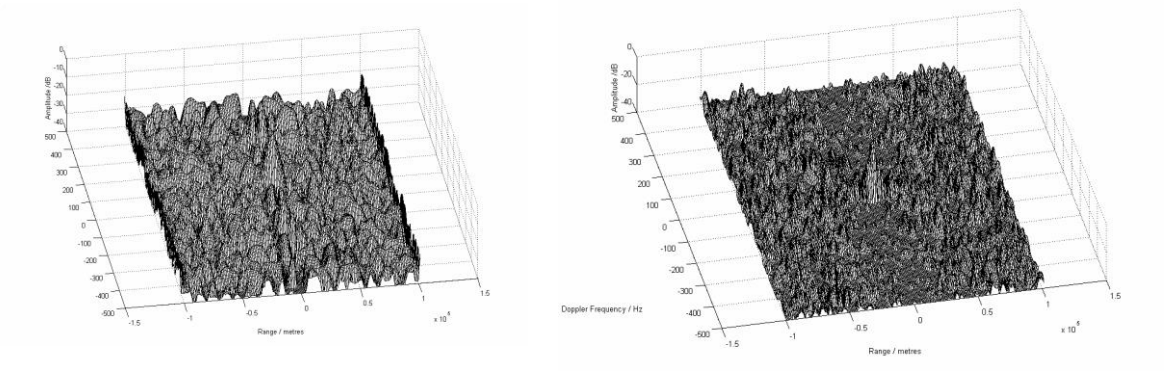

(a) (b)

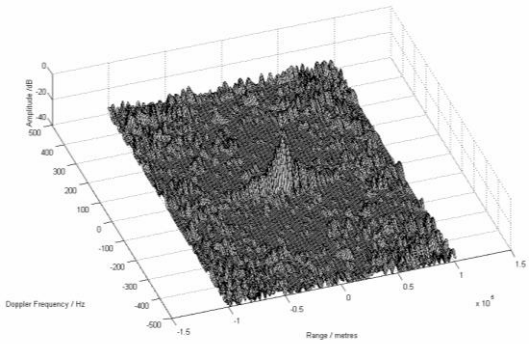

(c)

Figure 8 Ambiguity function of: (a) FM signal at 102.2 MHz (Jazz music); (b) DAB signal at 222.4 MHz and (c) DVB-T signal at 505 MHz

3 DVB-T BASED PBR

3.1 INTRODUCTION

Most studied transmitters of opportunity for maritime surveillance are those of the GSM mobile network, that were proved to have nice tracking capability of small and fast boats at short ranges ([11]-[13]). Aiming at increasing the range coverage and the range resolution, transmission of DVB-T signals represents one of the most attractive choice.

Up to know the potentialities of a DVB-T based PBR system for maritime surveillance have been only preliminary demonstrated. In [14], a preliminary investigation has been conducted: a large ship approximately 170 m long was detected at about 2 nm (about 3,7 km). In [15], our research group showed that such sensor might be successfully employed for monitoring typical maritime traffic offering good detection capability even for small boats within the territorial waters (<12 nm). Further studies ([16]) proved that a DVB-T based PBR can offer even high potentialities in detecting targets at much longer ranges. In fact, due to the low carrier frequency, the radio wave is expected to travel well beyond the normal line of sight thanks to the combination of several propagation mechanisms. This fact is enhanced over sea paths where super-refractive conditions are prevalent.

During the research activity, a great effort has been devoted to the implementation of the signal processing chain of a DVB-T based PBR system for maritime surveillance at short, medium and long range. The system was required to perform a quasi-real-time operation and for this reason an efficient implementation of all the applied techniques in the processing chain has been done. In addition, computing on graphing processing unit (GPU) has been considered to reduce the elaboration time required by the algorithms.

This work has been conducted upon a contract between Selex ES and DIET Dept and represents an extension of a previous research activity that allowed to state the potentialities of the DVB-T signal as an opportunity signal for air traffic control purposes. With respect to ATC applications, maritime surveillance requires a proper modification of the signal processing in order to account for the following problems:

- very low speed of naval targets,
- the chance to have close targets with very high difference in radar cross sections,
- sea clutter and multipath.

A great emphasis has been devoted to (i) the development of algorithms better suited for maritime surveillance with respect to those already developed by our research group for air traffic control applications and (ii) the implementation of the processing chain on different architectures in order to identify the faster one to perform quasi real-time surveillance.

Among all the PBR systems described in literature, no one is capable of performing quasi real-time operation. In addition, some issues are still not being solved such as: proper sea clutter cancellation and target direction of arrival estimation in a wide unambiguous angular sector. Those points have been faced during the research activity and the results will be presented in the following. In addition, the multi-frequency integration, which is a well-known and used topic in FM radio based PBR, it hasn't still been implemented for DVB-T signals both for the high data rate required by the signal processing chain and for some limitations due to the too fine range resolution. Some details on a preliminary analysis about this topic will be provided too.

This chapter is organized as follows. The receiver architecture and the radar signal processing chain are described in 3.2. All the main blocks will be treated in detail from Sections 3.3 to 3.6. For each of them it will be provided the description about faced issues and solution that have been proposed. In Section 3.7 some hints on the multi-frequency integration are provided. Section 3.8 contains detail about the implementation of the radar signal processing chain on the GPU.

3.2 RECEIVER ARCHITECTURE AND SIGNAL PROCESSING CHAIN

As the receiver was completely developed by Selex ES, all its characteristics constitute sensible data that cannot be provided in detail. Enough to know that the system allows the down-conversion of up to 8 DVB-T channels for up to 4 receiving antennas. In particular, the acquisition campaigns have been conducted using one reference antenna and up to three surveillance antennas. Analog signals captured by the antennas are passed through an analogic front-end constituted by band-pass filtering and low-noise amplifier before entering the acquisition board for digitization and down-conversion. Signals are digitized with a sampling frequency equal to $f_s = 64/7$ MHz which is the inverse of the fundamental period of the DVB-T signal.

Then signals are passed through a processing chain whose main functions are depicted in Figure 9. As the knowledge of the transmission mode and the guard interval size is propaedeutic for the application of some of the developed techniques, a proper block for 'DVB-T mode understanding' is inserted at the beginning of the chain. It works by looking for some specific features of the signal which position is a function of the transmission mode and guard interval size.

The main blocks of the processing chain are:

1. Sidelobe level control (SLL)

   The intrinsic characteristics of the DVB-T signal gives rise to periodic structures that cause the arising of undesired peaks in the ambiguity function of the signal. Those peaks may cause severe masking effects and/or additional false alarms producing a degradation of the radar system performance. Main responsible of such structures are the guard interval and the pilot carriers that are introduced in the signal to facilitate its demodulation. The level of those peaks cannot be reduced neither enlarging the CPI or recurring to tapering windows (e.g. Hamming windows, etc.). For this reason, a pre-filtering stage is performed on the reference signal.

2. Disturbance cancellation

   Surveillance signals carry useful target echoes as well as direct signal breakthrough, clutter and multipath. Such disturbance contributions may be responsible for weak target masking and an increase of the false alarm rate. For this reason, they need to be removed from the surveillance signals to enable the detection of the weak target echoes. Later on this chapter existing techniques for disturbance removal will be presented; however as will be highlighted they do not always provide adequate performance against maritime disturbance scenarios, therefore an extension of such techniques will be presented which is able to overcome such limitations.

3. Range-Doppler map (RDM) evaluation

   After disturbance removal the RDM is evaluated; this operation corresponds to the implementation of a bank of matched filters, each one tuned to a specific target bistatic velocity. In this chapter several existing optimum and sub-optimum techniques for RDM evaluation will be described. Among them the ones better suited for maritime surveillance will be identified; in addition a novel technique, extensively used in various acquisition campaigns conducted for system validation, will be presented.

4. Constant False Alarm Rate (CFAR)

   Detection process is performed comparing the power contained in each RDM pixel with the power contained in a set of neighboring cells that are assumed to carry only disturbance. They contribute to set the threshold level and allow to maintain the false alarm rate at a constant level.

5. M/N integration criterion and DoA estimation

By using at least two surveillance antennas, one is able to perform direction of arrival (DoA) estimation of the potential targets. DoA estimation is conducted for each pixel of the RDM that satisfied the integration criterion among the surveillance channels. For example, if we use an $N = 3$ surveillance element array to watch over a certain region and we set $M = 2$, a detection will be declared – and therefore we will estimate the DoA – if and only if we had in a certain pixel of the map at least two detections over the three surveillance channels.

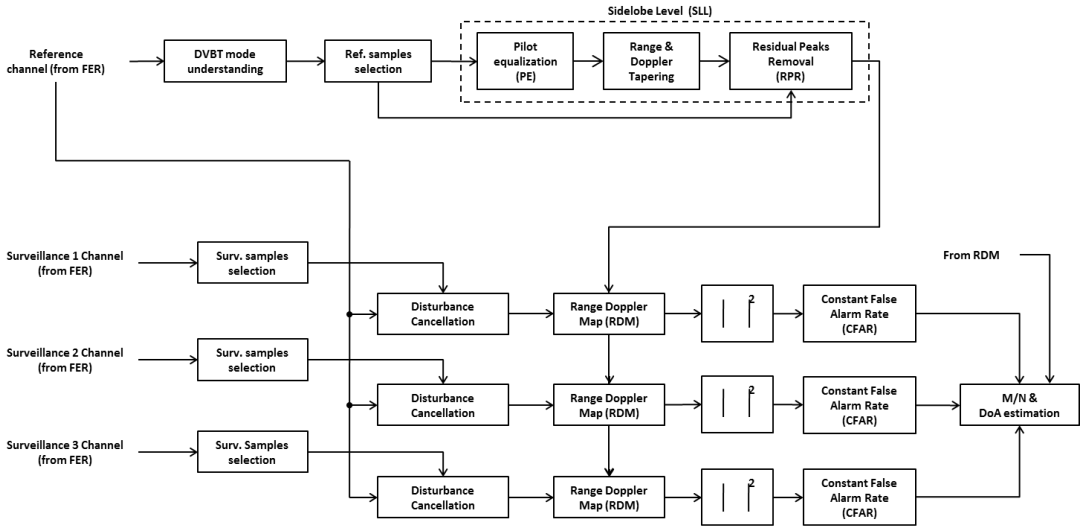

Figure 9 Radar signal processing chain.

Data at the output of the last block represent the input for the target tracking stage, that was not a topic covered during the thesis. The following paragraphs will cover each of the listed blocks and special attention will be kept for those blocks that have been mostly studied in deep to meet the desired requirements for maritime surveillance.

3.3 SIDELOBE LEVEL CONTROL

In this paragraph some hints about the technique for sidelobe level control will be provided. For a while such problem has been a hot topic for the research community. As already anticipated, the presence of particular characteristics in the DVB-T signal gives rise to a number of complications as soon as the signal is exploited for radar purposes. Actually those structures are inserted to facilitate the demodulation of the carried information, however they yield undesired peaks in the ambiguity function (AF) of the signal and may cause severe masking effect limiting the overall system capability in detecting targets.

As reported in [28], the DVB-T signal is composed by:

- data and TPS (transmission parameter signaling) components that are transmitted with unity power level,
- continual and scattered pilots, both transmitted at a boosted power level ($E_P = 16/9$).

Continual and scattered pilots give rise to undesired peaks in the ambiguity function of the signal. Depending on whether those peaks come from the correlation of the same or consecutive OFDM symbols, they are identified as 'inter' or 'intra-symbol' peaks. An additional peak is due to the insertion of the guard interval at the beginning of each OFDM symbol.

In Figure 10 the 2D view of the AF is reported versus delay and Doppler frequency in T_s and $1/T_s$ units, respectively. Those units have been considered as they allow a unified treatment of the 2k and 8k mode as well as of different guard intervals. Black dots identify Delay-Doppler locations characterized by a peak-to-sidelobe ratio lower than 40 dB; thus they represent – except for the one located in the center – the position of the undesired peaks which appear quite regularly spaced in the Delay-Doppler domain. Exact position of each undesired peak can be analytically calculated simply knowing the signal transmission mode and the guard interval size; details about their position are provided in [28].

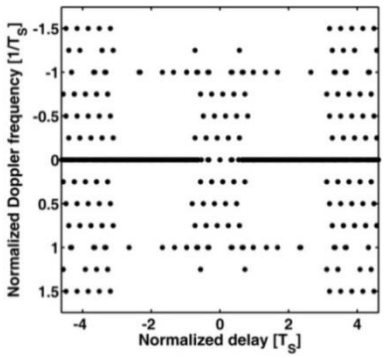

Figure 10 2D view of DVB-T signal AF with side peaks identification.

The technique proposed by our research group to remove such peaks consists of two filters (see Figure 11) going under the name of Pilots Equalization (PE) and Residual Peaks Removal (RPR).

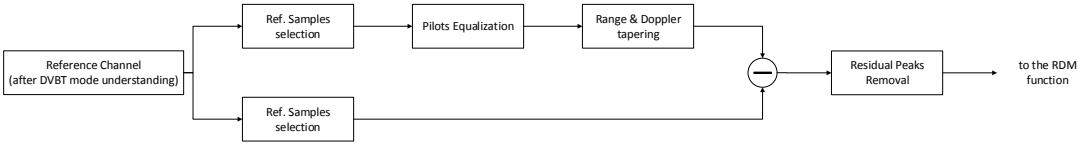

Figure 11 Block diagram of the SLL control technique.

The former filter acts over the amplitude of the pilot carriers of the reference signal in a way that their amplitude, after the cross-correlation with the surveillance signal results to be normalized and does not provide any undesired

peaks. The application of the PE filter allows the complete removal of 'intra-symbol' peaks (i.e. thus appearing at a distance than the symbol duration T_s) as can be seen in Figure 12(a).

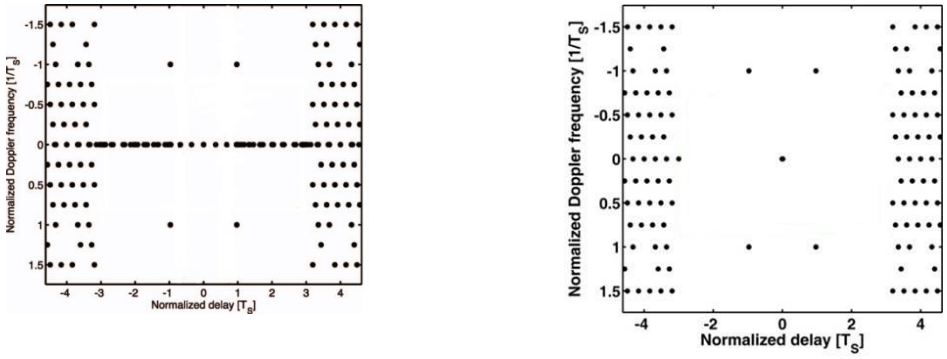

(a) (b)

Figure 12 DVB-T signal AF after the application of (a) PE filter, (b) PE + RPR filter.

PE filter is based on the observation that the signal contributions due to continual and scattered pilots have frequency positions that are fixed from symbol to symbol or at maximum changed over four symbols period, respectively. Those contributions are transmitted at boosted power level ($E_P = 16/9$), in fact the DVB-T signal $s[n]$ can be expressed as:

$$s[n] = s_D[n] + \frac{4}{3}s_P[n] \tag{5}$$

where $s_D[n]$ is the contribution resulting from the data and TPS subcarriers, while $s_P[n]$ is the contribution resulting from both continual and scattered pilots. As anticipated due to the periodicity of the latter contribution, it can be expressed as:

$$s_P[n] = s_P[n - mN_{SS}] \qquad m \in \mathbb{Z} \tag{6}$$

being $N_{SS} = 4T_s f_s$. The effective solution for pilots equalization proposed by our research group consists in subtracting, from the original signal, its own replica, delayed by an integer multiple of $4T_s$ and scaled by $(1 - 1/E_P) = 7/16$:

$$s_{Seq}[n] = s[n] - \frac{7}{16}s[n - MN_{SS}] \tag{7}$$

thus obtaining

$$s_{Seq}[n] = s_D[n] - \tfrac{7}{16}s_D[n - MN_{SS}] + \tfrac{3}{4}s_P[n]. \tag{8}$$

In this way the amplitude of the pilots contribution in (8) is equal to $3/4$. This allow the pilots component to be effectively normalized in the surveillance signal after cross-correlation, as desired for a pilot equalization stage. The additional data component – specifically the second term in the right side of (8) – may be responsible for additional undesired peaks in the AF. Thus a proper move would be to choose M in a way that those components would fall outside of the area of interest. Considering the size of the area of interest for maritime purposes, $M = 2$ represents a reasonable choice to avoid such additional peaks in the RDM.

As can be seen from Figure 12(a), for delays shorter than T_s – that are long enough to perform maritime surveillance – residual undesired peaks only appear at zero Doppler. Those may be removed applying the RPR filter.

For the purpose, the zero-Doppler cut of the AF is extracted from the mismatched auto-correlation function (ACF) between the original reference signal and the one at the output of the AF filter:

$$R_{PE}[l] = \chi_{PE}[l, 0] = \sum_{n=0}^{N-1} s[n]\, s_{PE}^{*}[n-l] \tag{9}$$

The output will be the central row of the AF represented in Figure 12(a). RPR filter weights are obtained by solving a system of linear equations that forces the mismatched ACF to be equal to zero at every point except the one corresponding to the main peak. To reduce its complexity, the zero-constraint is imposed only at the expected peaks position of the ACF. For the purpose, the ACF is oversampled using an oversampling factor equal to 3. As can be seen from Figure 12(b), the joint exploitation of PE and RPR filters allow the correct removal of all the peaks appearing at a normalized delay smaller than or equal to $3T_s$ and at absolute normalized Doppler frequencies smaller than $1/T_S$.

3.3.1 SELECTIVE UTILIZATION OF THE TECHNIQUE

The presented technique was developed by our research group and no changes have been made to it as its effectiveness even in maritime applications has been extensively proved. However, the requirement for a quasi-real-time operation of the PBR system has prompted a study on the actual need of applying both the filters when performing maritime surveillance.

Depending on the required coverage, a computational load saving could be achieved avoiding to apply filters when they are not needed. From theory, the first undesired peak in the zero-Doppler cut lies at a normalized delay equal to $T_u/3$: therefore its position is only a function of the transmission mode (2k – 8k) and it does not depend on the guard interval.

In the frequency domain, the first peak occurs at $(1/4T_s)$, then its position varies with the transmission mode and the guard interval size. Table 5 shows the position in the bistatic range and bistatic velocity coordinates of the nearest undesired peaks as a function of the transmission mode and guard interval dimension. As the bistatic velocity is related to the Doppler frequency via the wavelength λ, the smaller λ the closer are the undesired peaks. Values reported in the table refer to the worst case in terms of size of the wavelength, in fact the higher DVB-T channel ($f_c = 866$ MHz, $\lambda = 0{,}35\ m$) has been considered.

Table 5 Bistatic range and bistatic velocity positions of the nearest undesired peaks.

		Guard interval				
		1/4	1/8	1/16	1/32	
Bistatic range	[km]	22.4				2k Mode
Bistatic velocity	[km/h]	±556.75	±618.60	±654.99	±674.84	
Bistatic range	[km]	89.6				8k Mode
Bistatic velocity	[km/h]	±139.18	±154.65	±163.74	±168.71	

Given an acquired signal, characterized by some wavelength λ, it is possible to estimate its transmission mode and guard interval size through the '*DVBT mode understanding*' block. From them, the position of the first peaks can be obtained. Comparing those values with the desired coverage of the RDM, it is possible to state the actual need of performing both or just one of the filters. In particular, if one is interested in performing surveillance with a range coverage smaller that the first peak in the range dimension, there is no need for the RPR filter. While PE filter is not required whenever the desired velocity extent to be covered is smaller than half the values reported in the table.

The signal at the output of the RPR filter represents the input for the calculus of the Range-Doppler map that is discussed below.

3.4 DISTURBANCE CANCELLATION

3.4.1 INTRODUCTION

Disturbance cancellation represents a key stage within a conventional PCL processing scheme despite the kind of waveform is used and/or the application it is intended for. Such issue has been addressed with other members of our research group each one working on a different topic. The following explanation is derived from our journal publication and keeps the same structure of the latter to facilitate the understanding of both the issue and the proposed solution. However, with respect to the journal paper, much more results will be provided for the maritime application.

As anticipated in the introduction of this thesis, PCL systems can be regarded as "invisible" systems catching extremely weak signals (target echoes) that are usually "invisible" to the ordinary users of the employed transmitter. This is made possible by the use of receivers with wide dynamic range and by the application of appropriate signal processing techniques to tackle the invisibility of such weak target echoes against typical undesired signal contributions, above all the direct signal breakthrough and multipath.

When the PCL is equipped with a single or few receiving channels, disturbance cancellation is usually accomplished in the time domain. To this purpose, the signal collected at the reference channel is typically exploited to remove undesired contributions, received together with the moving target echo, on the surveillance channel. Different approaches have been proposed to cope with this problem yielding solutions with different complexity and effectiveness ([29]-[41]).

Among these approaches, a widely used cancellation technique is the Extensive Cancellation Algorithm (ECA) and its Batches version (ECA-B) ([36]), whose working principle and performance are shown in the next paragraphs. These techniques have been largely employed by our as well as by other research groups and became a key-step within the signal processing chain of many different PCL prototypes. A number of contributions appeared in the open literature where the effectiveness of these cancellation approaches has been clearly demonstrated with reference to quite different PCL applications exploiting various waveforms of opportunity, e.g. ([41]-[55]). Nevertheless, ECA and ECA-B present some limitations when employed against highly time-varying disturbance scenarios.

The advantages yielded by the proposed cancellation approach are verified in this paper with reference to three live data sets accounting for very different PCL applications. Specifically, a WiFi-based PCL is considered for target detection at short range aiming at local area surveillance. A DVBT-based PCL is exploited for medium range maritime surveillance. Finally, an FM-based PCL is employed for typical air traffic control (ATC) applications.

The paper is organized as follows. The ECA and the ECA-B approaches are briefly recalled in 3.4.2 and some real-life examples are shown to demonstrate the benefits of a batches operation in different surveillance applications. The limitations of the ECA-B are investigated in 3.4.3 by means of theoretical derivations and experimental results. Then the ECA-S approach is presented in 3.4.4 and its effectiveness is demonstrated in 3.4.5 against experimental data sets compared to previous ECA versions. 3.4.6 reports some considerations on the computational load aiming at the practical implementation of the proposed approach. Finally, conclusions are drawn in 3.4.7.

3.4.2 ECA AND ECA-B APPROACHES

As well known the ECA operates by subtracting from the surveillance signal $s_s(t)$ properly scaled and delayed replicas of the reference signal $s_r(t)$ [36]. Specifically, by sampling the received signals at f_s and assuming that the multipath echoes are backscattered from the first *K* range bins, the output of the ECA is evaluated as:

$$s_{ECA}[n] = s_s[n] - \sum_{k=0}^{K-1} \alpha_k s_r[n-k] \quad n = 0, \dots, N-1 \tag{10}$$

being *N* the number of samples within the CPI T_{int}. The filter coefficients $\boldsymbol{\alpha} = [\alpha_0 \ \alpha_1 \ \cdots \ \alpha_{K-1}]^{\boldsymbol{T}}$ are evaluated by resorting to a Least Square (LS) approach that minimizes the power of the signal at the output of the filter:

$$\boldsymbol{\alpha} = (\mathbf{S}_r^{\mathrm{H}} \mathbf{S}_r)^{-1} \mathbf{S}_r^{\mathrm{H}} \mathbf{s}_s \tag{11}$$

where $\mathbf{s}_s$ is a $N \times 1$ vector containing *N* samples of the surveillance signal and $\mathbf{S}_r$ is a $N \times K$ matrix whose columns are the delayed versions of the reference signal. As is apparent, in its original version, the ECA requires the filter weights to be estimated over the whole CPI.

In contrast, the ECA-B output at the *l*-th batch is written as

$$\begin{gathered} s_{ECA-B}[n] = s_s[n] - \sum_{\mathrm{k}=0}^{\mathrm{K}-1} \alpha_k^{(l)} s_r[n-k] \\ n = lN_B, \dots, (l+1)N_B - 1; \ l = 0, \dots, B-1 \end{gathered} \tag{12}$$

where N_B is the dimension of each batch, $B = \left\lfloor \frac{N}{N_B} \right\rfloor$ is the number of batches, and $\boldsymbol{\alpha}^{(l)} = \left[\alpha_0^{(l)} \ \alpha_1^{(l)} \ \cdots \ \alpha_{K-1}^{(l)}\right]^T$ is the filter coefficients estimate obtained at the *l*-th batch, namely by exploiting the *l*-th signal fragment of duration $T_B = N_B / f_s$. Basically we have

$$\boldsymbol{\alpha}^{(l)} = \left[\mathbf{S}_r^{(l)^H} \mathbf{S}_r^{(l)}\right]^{-1} \mathbf{S}_r^{(l)^H} \mathbf{s}_s^{(l)} \tag{13}$$

where $\mathbf{s}_s^{(l)} = \left[s_s[lN_B], \ s_s[lN_B + 1], \cdots, s_s[(l+1)N_B - 1]\right]^T$ is a $(N_B \times 1)$ vector and $\mathbf{S}_r^{(l)}$ is a $N_B \times K$ matrix collecting the delayed copies of the corresponding reference signal fragment.

The ECA-B has been demonstrated to yield effective disturbance cancellation and target detection in a number of applications ([17],[28],[36],[52]-[55]). Usually the batch duration T_B has to be carefully selected as it affects the capability of the system to adapt to the time-varying characteristics of the environment. However, to avoid undesired effects, the need for a rapid update of filter coefficients has to be traded with the accuracy of the adaptive estimation and with the necessity of preserving the target echo.

These points are investigated here with reference to quite different PCL applications by exploiting real data sets collected in various conditions. Specifically, three PCL experimental prototypes have been used that exploit different waveforms of opportunity and are intended for various surveillance applications.

A. FM-BASED PCL FOR ATC APPLICATIONS

First of all, we consider a long range surveillance application using the FM radio signal as waveform of opportunity. Specifically, we exploit the data set collected on June 7th 2012, in a site near the Fiumicino Airport of Rome. Receiver architecture and acquisition geometry are described in detail in [17]. Enough to know that two antennas were used: one antenna was employed to collect the reference signal and was steered toward the transmitter located on Monte Cavo, about 35 km South-East of the receiver site; the other antenna was pointed toward the opposite direction to gather the surveillance signal. Several sequential data acquisitions were performed for different FM radio channels; each data file is about 1.1 sec of duration, with a temporal spacing of about 2.3 sec between two consecutive acquisitions. All the available data files have been first processed according to different ECA versions with K=140 taps (i.e. 210 km @ f_s=200 kHz).

The disturbance cancellation capability is studied in Figure 13 along 200 consecutive data files for different choices of the batch duration employed by the ECA-B. The reported clutter attenuation (CA) is defined as the ratio between the

power levels measured, over the considered FM radio channel bandwidth, at the input and at the output of the cancellation filter. As is apparent, operating with a conventional ECA (i.e. $T_B = 1$ s in this application where $T_{int} = 1$ s is adopted) yields a significant cancellation loss with respect to the theoretical cancellation (about 52 dB); this can be attributed to a number of factors there including Tx/Rx non-idealities as well as the presence of interference. Nevertheless, disturbance removal via ECA-B provides remarkably better results making the system robust to slowly varying conditions of the observed scenario. Specifically reducing the batch duration down to $T_B = 25$ ms allows a significant improvement in term of CA with respect to the conventional ECA. In fact, the average CA increases by 6 dB and the performance is much more stable along the acquisition time. Further reducing the batch duration might yield some degradation in most of the considered data files due to the progressively larger adaptivity loss. Therefore T_B values around 25 ms will be considered in the following to guarantee effective cancellation against this specific scenario.

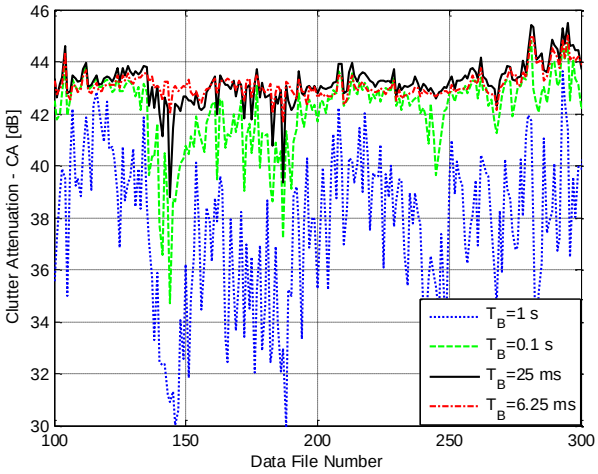

Figure 13 Clutter attenuation (CA) along the acquisition for the ECA-B operating with different batch durations.

B. DVB-T-BASED PCL FOR MARITIME SURVEILLANCE

Due to their fine range resolution and the high effective radiated power (ERP) associated with their illuminators, Digital Video Broadcasting-Terrestrial (DVB-T) transmissions represent one of the most attractive choices to be used for naval target localization and tracking. The potentialities of DVB-T based PCL have been preliminary demonstrated both for short/medium [15] and for long range maritime surveillance [16].

Here we report the results obtained against the DVB-T based PCL data collected during the acquisition campaigns held by Selex-ES at various sites along the Italian coastline. In Figure 14 we focus on four different data sets; for each of them 30 consecutive data files of duration 1 s have been considered and ECA-B with different values of batch duration, T_B, has been applied to the received signals. Since a CPI of 1 s is adopted in the following, setting $T_B = 1$ s corresponds to the application of ECA. In particular, the CA as a function of T_B is reported in Figure 14, averaged over the considered 30 data files for each considered Data Set.

As is apparent, Data Sets 1 and 2 account for quite stationary scenarios. In this case an almost flat trend of CA is observed for high enough values of the batch duration (i.e. $T_B > 0.1$ s); further decreasing the batch duration leads to an increase of the adaptivity loss thus yielding slightly worse disturbance cancellation.

In contrast, when the system operates against highly non-stationary scenarios, progressive decrease of T_B allows to better adapt to the varying characteristics of the disturbance (see Data Sets 3 and 4). However it is worth noticing that uncontrolled decrease of the batch duration may lead to detrimental detection losses for slowly moving targets that fall in the cancellation filter. For this reason, it is convenient to identify a useful set of T_B values that: (i) give rise to

small CA losses when working in stationary scenarios and (ii) yield a good trade-off between measured CA and slowly moving targets detection when dealing with non-stationary scenarios. Based on the analysis reported in Figure 14, a reasonable choice could be $T_B \in [0.05\ \text{s}, 0.2\ \text{s}]$.

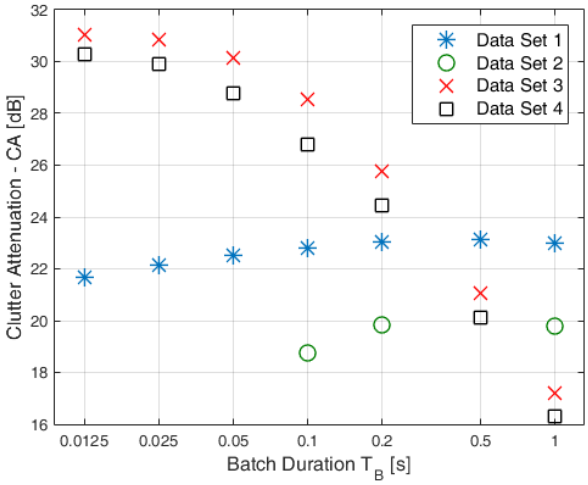

Figure 14. Clutter attenuation (CA) as a function of the batch duration for the ECA-B. Comparison between data sets acquired in different scenarios.

C. WIFI-BASED PCL FOR LOCAL AREA MONITORING

WiFi transmissions might be successfully exploited in local area monitoring applications aiming at the detection of designated vehicles or human beings within public/private buildings and surrounding areas [54]-[55]. As an example of this application, we show the results obtained using the experimental equipment described in [55]. In particular, a wireless access point (AP) was employed, set up to emit the beacon signal at 3 ms, and a quasi-monostatic configuration was adopted for the surveillance and the transmitting antennas. Tests have been performed in a parking area using vehicles as cooperative targets.

In addition, in this specific application we were allowed to perform some target-free tests in order to evaluate the disturbance cancellation capability in controlled situations avoiding the target effects. To this purpose, an acquisition of 20 s is considered in the following that includes just disturbance contributions (direct signal and echoes from the stationary scene).

Figure 15 reports the cancellation performance along the acquisition time for the ECA-B operating over a range extension of 500 m with different durations of the batch. In this application, the measured CA is close to the maximum theoretical expected value (29.4 dB) even operating with long batches (i.e. using a conventional ECA). In fact in this case, the system operates in a scenario that mostly includes man-made objects. Therefore the non-stationary behavior of the received signals is mostly due to the instabilities of both the transmitter and the receiver. Nevertheless the decrease of the batch duration allows a slight improvement in term of average CA: about 0.4 dB gain is obtained moving from $T_B = 0.5$ s to $T_B = 15$ ms (Figure 15(a) and Figure 15(d), respectively). Moreover we observe that a much more stable CA is achieved along the acquisition time which clearly demonstrates the increased capability to adapt to the time-varying characteristics of the collected signals.

This analysis allows us to select a batch duration between 50 ms and 15 ms. Notice that, in this case it is not recommended to further decrease T_B since we recall that WiFi transmissions are of a pulsed type and, due to the exploited Carrier Sense Multiple Access (CSMA) approach, the transmission may be inhibited for a long time thus yielding a high temporal separation among consecutive pulses. Therefore operating with very small batches there

might be a high variability in the number of pulses included in each batch and, in extreme cases, this might yield empty batches.

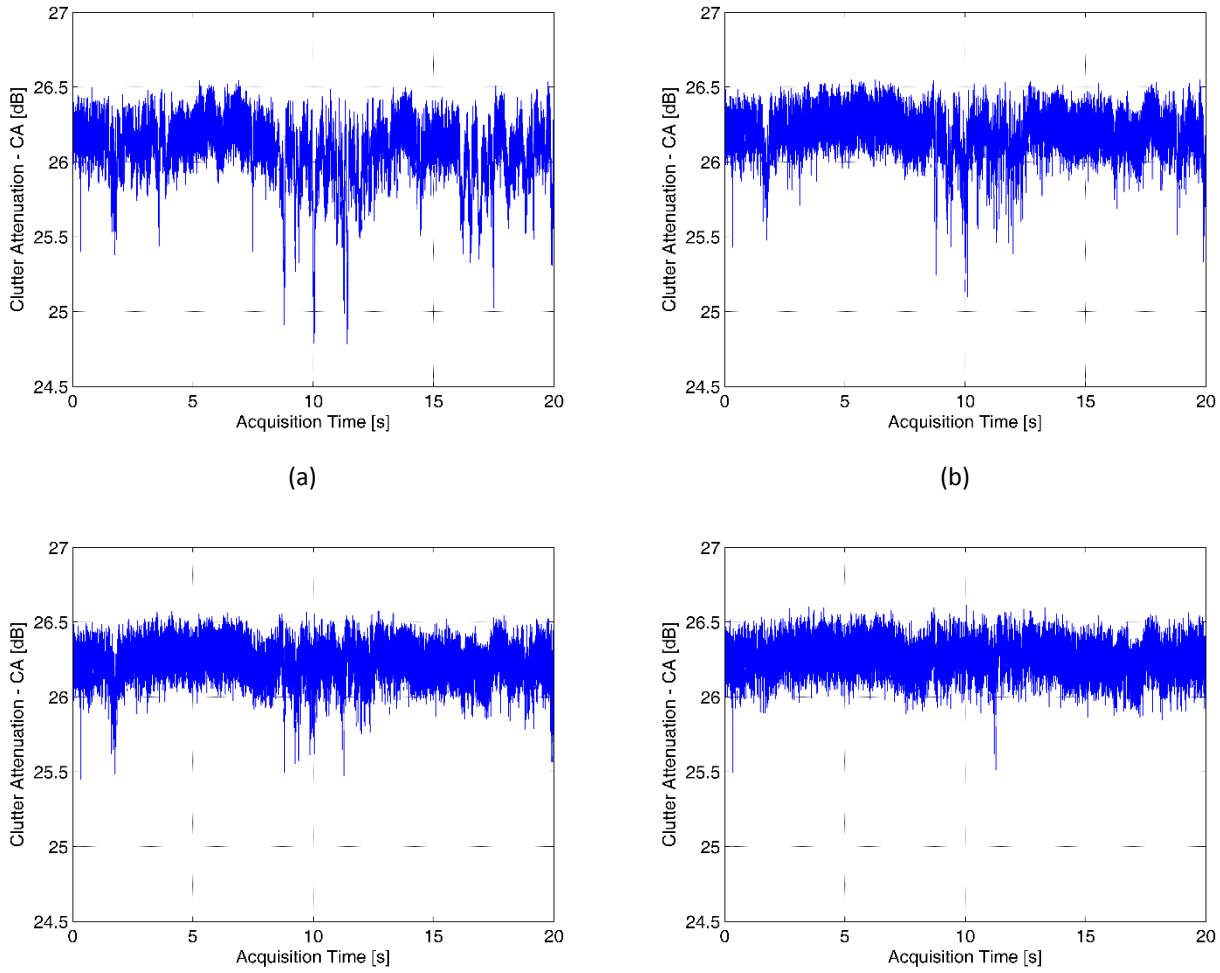

Figure 15 Clutter attenuation (CA) along the acquisition time for the ECA-B operating with different batch durations. (a) $\mathbf{T_B = 0.5}$ s; (b) $\mathbf{T_B = 0.1}$ s; (c) $\mathbf{T_B = 50}$ ms; (d) $\mathbf{T_B = 15}$ ms.

3.4.3 LIMITATIONS OF THE ECA-B

The benefits of the ECA-B approach have been shown in the previous section in term of disturbance cancellation capability. Specifically, it has been verified that, widening the cancellation notch by reducing the batch duration up to a certain limit allows a better removal of the disturbance contributions.

Obviously, this has a non-negligible impact on the target echoes, especially those observed at low Doppler frequencies. However, we show that this impact is not limited only to the typical SNR loss due to the partial cancellation of slowly moving target echoes.

To this purpose we consider the two-dimensional (Range-Doppler) cross-correlation between the reference signal and the surveillance signal after the disturbance cancellation stage. The resulting map is a representation of the Range-Doppler distribution of the signal energy at the output of the cancellation filter. Therefore, its analysis gives a further insight into the performance of the considered cancellation algorithm.

For example, let us consider the short range application employing a WiFi-based PCL, in which it is quite typical to deal with targets observed at low Doppler frequency, namely slowly-moving targets or targets moving mainly along the cross-range direction. Therefore, it is of interest to study the effect of the ECA-B on the detection of such targets. To this purpose we show the results obtained with the experimental set-up described in 3.4.2.C, for a test performed against a vehicular target moving in the cross-range direction with approximate speed 4.5 m/s and distance of minimum approach R_0 = 20 m. In such geometry, the target describes a parabolic trajectory on the bistatic Range-Doppler plane and, for a long time, it will be observed at Doppler frequencies within or close to the cancellation filter notch. As an example, Figure 16 and Figure 17 show the range-Doppler maps obtained after disturbance cancellation with a CPI $T_{int} = 0.2$ s for two different positions of the target along its trajectory. Proper techniques have been applied to control the sidelobes level of the signal ambiguity function [54]. All the reported maps have been normalized to thermal noise power level so that the value at each map location represents the estimated signal to noise ratio (SNR). Notice that the dynamic range has been lower limited to better highlight the main structures arising in the map. The adopted cancellation filters operate over a range extension of 500 m with different values of the batch duration T_B.

Specifically, Figure 16 accounts for a favorable situation since the target Doppler frequency is reasonably high so that it is not affected by the cancellation stage. In fact, in this case, the ECA-B operates with $T_B = 50$ ms that yields a notch Doppler extension equal to approximately $1/T_B$ which is significantly smaller than the target Doppler value. As a consequence, after the cancellation stage, the target appears as a strong peak at 53 m and -41 Hz. In addition, a further peak is also visible at 161 m and -33 Hz caused by the double-bounce reflection of the target echo over the metallic fence delimiting the parking area.

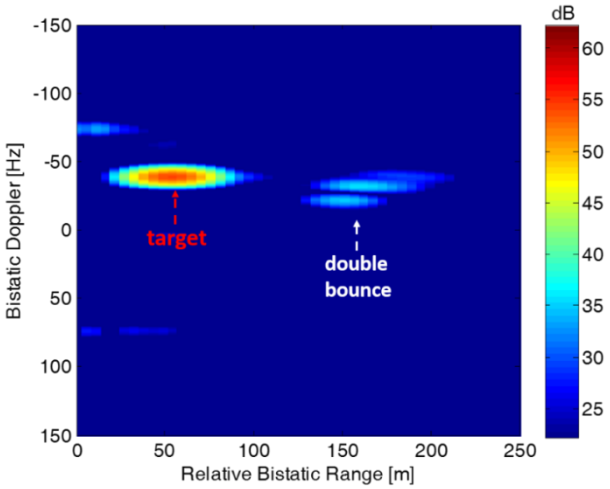

Figure 16 Range-Doppler map after ECA-B with $\mathbf{T_B = 50}$ ms in the case of a high Doppler target.

In contrast, Figure 17 shows the case of a target echo included in the filter notch so that it is expected to be strongly affected by the cancellation stage. In particular, Figure 17(a-c) have been obtained by using batch durations equal to $T_B = 50$ ms, $T_B = 30$ ms, and $T_B = 15$ ms, respectively.

As is apparent, in all cases, the target peak is surrounded by undesired structures in the Doppler dimension that might be responsible of useful dynamic range reduction or masking effects over weak targets, thus limiting the detection capability. These Doppler ambiguities are mainly due to the ECA-B approach that exploits consecutive batches of the received signals where the filter coefficients are separately estimated and applied. In fact this yields discontinuities in the target echo at the output of this stage appearing at regular intervals of T_B thus setting the Doppler spacing between unwanted peaks ($1/T_B$).

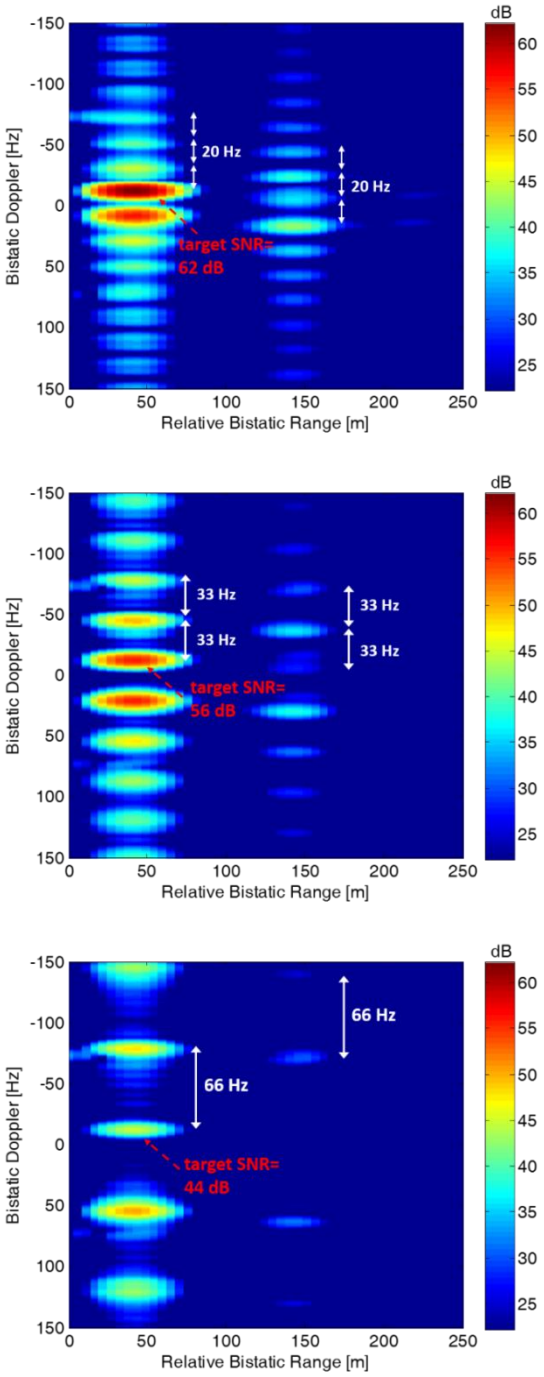

Figure 17 Range-Doppler maps after ECA-B for three different batch durations in the case of a low Doppler target: (a) $\boldsymbol{T_B = 50}$ ms; (b) $\boldsymbol{T_B = 30}$ ms; (c) $\boldsymbol{T_B = 15}$ ms.

This is demonstrated here with reference to the following simplifying hypotheses:

(i) the surveillance signal includes a single moving target echo observed with amplitude A_t at Doppler f_d with delay $\tau = n_\tau / f_s$, a single zero-Doppler replica of the transmitted signal received from the same target range cell (i.e. delay τ) with amplitude A_c, and thermal noise w_s:

$$s_s[n] = A_t d[n-n_\tau] e^{j2\pi f_d n/f_s} + A_c d[n-n_\tau] + w_s[n] \tag{14}$$

where $d[n]$ is the signal emitted by the illuminator of opportunity with unitary average power. Notice that the zero-Doppler term in (14) might represent either the direct signal from the transmitter or a stationary multipath contribution.

(ii) the reference signal is an ideal noise-free copy of the transmitted signal: $s_r[n] = A_r d[n], n = 0, \dots, N-1$.

(iii) the ECA filter operates with a single tap, i.e. $K = 1$, against the sole range cell at delay τ that includes both the target and the multipath echoes. Without loss of generality we further assume that $\tau = n_\tau/f_s = 0$.

With the positions above, the filter in (11) and (13) reduces to a single complex coefficient. In particular, at the *l*-th batch ($l = 0, \dots, \left\lfloor \frac{N}{N_B} \right\rfloor - 1$), it can be written as:

$$\alpha_0^{(l)} = \frac{1}{\left\|\mathbf{s}_r^{(l)}\right\|^2} \mathbf{s}_r^{(l)H} \mathbf{s}_s^{(l)} = \frac{1}{|A_r|^2 \|\mathbf{d}^{(l)}\|^2} \left[A_r^* A_t \mathbf{d}^{(l)H} \mathbf{d}_{f_d}^{(l)} + A_r^* A_c \left\|\mathbf{d}^{(l)}\right\|^2 + A_r^* \mathbf{d}^{(l)H} \mathbf{w}_s{}^{(l)} \right] \tag{15}$$

where $\mathbf{d}^{(l)}$ is the $N_B \times 1$ vector containing the *l*-th batch of the direct signal and $\mathbf{d}_{f_d}^{(l)}$ is its Doppler shifted version.

Consequently, the output of the ECA-B at the *l*-th batch is:

$$\begin{aligned} \mathbf{s}_{ECA-B}^{(l)} &= \mathbf{s}_s^{(l)} - \alpha_0^{(l)} \mathbf{s}_r^{(l)} = \\ &= A_t \mathbf{d}_{f_d}^{(l)} - \frac{A_t}{\|\boldsymbol{d}^{(l)}\|^2} \mathbf{d}^{(l)H} \mathbf{d}_{f_d}^{(l)} \mathbf{d}^{(l)} + \mathbf{w}_s{}^{(l)} - \frac{1}{\|\mathbf{d}^{(l)}\|^2} \mathbf{d}^{(l)H} \mathbf{w}_s{}^{(l)} \mathbf{d}^{(l)} \end{aligned} \tag{16}$$

where the original stationary disturbance contribution in the surveillance signal has been perfectly removed thanks to the simplifying hypotheses above. As is apparent the ECA-B output includes the ideal target contribution, $A_t \mathbf{d}_{f_d}^{(l)}$, along with an additional zero-Doppler contribution whose amplitude depends both on the target amplitude A_t and on the target Doppler frequency via the scalar product $\mathbf{d}^{(l)H} \mathbf{d}_{f_d}^{(l)}$. Therefore, this term cannot be neglected for slowly moving target echoes, i.e. targets observed at low Doppler frequencies, and it encodes the partial removal of the target echo due to the application of the cancellation filter. Similarly, the original thermal noise contribution, $\boldsymbol{w}_s{}^{(l)}$, is present together with a noise-dependent term which yields the theoretical upper bound to the achievable cancellation of zero-Doppler contributions.

Then we can evaluate the output of the range-Doppler map for the range bin of the target at the generic Doppler frequency f_0:

$$\chi[f_0] = \mathbf{d}_{f_0}^H \mathbf{s}_{ECA-B} = \mathbf{d}_{f_0}^H \begin{bmatrix} \mathbf{s}_{ECA-B}^0 \\ \vdots \\ \mathbf{s}_{ECA-B}^{B-1} \end{bmatrix} = \sum_{l=0}^{B-1} \mathbf{d}_{f_0}^{(l)H} \mathbf{s}_{ECA-B}^{(l)} \tag{17}$$

Substituting (16) into (17) we obtain:

$$\begin{aligned} \chi[f_0] = &\sum_{l=0}^{B-1} A_t \mathbf{d}_{f_0}^{(l)H} \mathbf{d}_{f_d}^{(l)} - \sum_{l=0}^{B-1} \frac{A_t}{\|\mathbf{d}^{(l)}\|^2} \mathbf{d}^{(l)H} \mathbf{d}_{f_d}^{(l)} \mathbf{d}_{f_0}^{(l)H} \mathbf{d}^{(l)} + \\ &+ \sum_{l=0}^{B-1} \left[\mathbf{d}_{f_0}^{(l)H} - \frac{1}{\|\mathbf{d}^{(l)}\|^2} \mathbf{d}_{f_0}^{(l)H} \mathbf{d}^{(l)} \mathbf{d}^{(l)H} \right] \mathbf{w}_s{}^{(l)} \end{aligned} \tag{18}$$

Aiming at understanding the impact of the ECA-B on the target echo, we focus our attention on the first two terms in eq. (18). Specifically, for the first term we might write:

$$\chi_I[f_0] = \sum_{l=0}^{B-1} A_t \mathbf{d}_{f_0}^{(l)^H} \mathbf{d}_{f_d}^{(l)} = A_t \mathbf{d}_{f_0}^H \mathbf{d}_{f_d} = A_t \sum_{n=0}^{N-1} |d[n]|^2 \, e^{-j2\pi(f_0 - f_d)n/f_s} \tag{19}$$

This term represents the ideal target contribution at the output of the 2D-CCF and its shape in the Doppler dimension strongly depends on the signal ambiguity function. As expected, for a constant modulus signal, eq. (19) yields the typical $\sin(Nx)/\sin(x)$ shape centered in $f_0 = f_d$ with peak amplitude $A_t N$, main lobe width $f_s/N = 1/T_{int}$, and period f_s:

$$\chi_I[f_0] = A_t \frac{sin[\pi(f_d - f_0)\, N/f_s]}{sin[\pi(f_d - f_0)/f_s]} e^{j\pi(f_d - f_0)(N-1)/f_s} \tag{20}$$

The second term in eq. (18) can be written as:

$$\chi_{II}[f_0] = A_t N_B^2 \sum_{l=0}^{B-1} \frac{1}{\|\boldsymbol{d}^{(l)}\|^2} g^{(l)}(f_d) \left[g^{(l)}(f_0)\right]^* \tag{21}$$

where $g^{(l)}(f) = \mathbf{d}^{(l)^H} \mathbf{d}_f^{(l)}/N_B$ is the output of the zero-Doppler filter for a unitary input signal with Doppler shift f. Notice that, for a constant amplitude signal, it results

$$g^{(l)}(f) = \frac{1}{N_B} \sum_{n=lN_B}^{(l+1)N_B - 1} |d[n]|^2 \, e^{j2\pi f n/f_s} = g^{(0)}(f) e^{j2\pi f l N_B/f_s} \tag{22}$$

being

$$g^{(0)}(f) = \frac{1}{N_B} \sum_{n=0}^{N_B - 1} e^{j2\pi f n/f_s} = \frac{1}{N_B} \frac{sin[\pi f N_B/f_s]}{sin[\pi f/f_s]} e^{j\pi f(N_B - 1)/f_s} \tag{23}$$

and eq. (21) becomes:

$$\begin{aligned} \chi_{II}[f_0] &= A_t N_B g^{(0)}(f_d)\left[g^{(0)}(f_0)\right]^* \sum_{l=0}^{B-1} e^{j2\pi(f_d - f_0) l N_B/f_s} = \\ &= A_t N_B g^{(0)}(f_d)\left[g^{(0)}(f_0)\right]^* \frac{sin[\pi(f_d - f_0)\, B N_B/f_s]}{sin[\pi(f_d - f_0) N_B/f_s]} e^{j\pi(f_d - f_0)(B-1)N_B/f_s} \end{aligned} \tag{24}$$

As is apparent $\chi_{II}[f_0]$ includes a $\sin(Bx)/\sin(x)$ shaped factor centered in $f_0 = f_d$ with period $f_s/N_B = 1/T_{\mathrm{B}}$. Notice that its main lobe width coincides with that in eq. (20) whereas its peak amplitude is modulated by the product $G(f_d, f_0) = g^{(0)}(f_d)\left[g^{(0)}(f_0)\right]^*$ which separately depends on the target Doppler frequency f_d and the Doppler of interest f_0 and we have $|G(f_d, f_0)| \leq 1$.

Let us consider the global output at specific Doppler values.

Setting $f_0 = f_d$ we infer that the target peak value is subject to a loss due to the cancellation stage. In fact in this case we obtain:

$$\chi[f_d] = \chi_I[f_d] - \chi_{II}[f_d] = A_t N \left\{1 - \left|\frac{1}{N_B} \frac{sin[\pi f_d N_B/f_s]}{sin[\pi f_d/f_s]}\right|^2\right\} \tag{25}$$

As expected, for a given batch duration, the loss depends on the target Doppler frequency and cannot be neglected as far as $|f_d| < 1/T_{\mathrm{B}}$.

It is interesting to evaluate the output at the ambiguous peaks of the $\sin(Bx)/\sin(x)$ term in (24), i.e. for $|f_0 - f_d| = \frac{p}{T_B}(p \in \mathbb{Z}, p \neq 0)$. First of all we observe that this condition does not guarantee that both f_0 and f_d are multiples of $\frac{1}{T_B}$, so that in the general case $G(f_d, f_0) \neq 0$ and the Doppler ambiguities clearly appear in the final map:

$$\left|\chi\left[f_d + \frac{p}{T_B}\right]\right| = \left|A_t \frac{N}{N_B^2} \frac{sin[\pi f_d N_B/f_s]}{sin[\pi f_d/f_s]} \frac{sin\left[\pi(f_d + \frac{p}{T_B})N_B/f_s\right]}{sin\left[\pi(f_d + \frac{p}{T_B})/f_s\right]}\right| \tag{26}$$

For a slowly moving target included in the cancellation notch, i.e. $|f_d| < 1/T_B$, the first $sin[N_B x]/sin[x]$ factor has non negligible values while the amplitude of the second factor decreases as $|p|$ increases. Therefore, in such conditions the target response at the output of the 2D-CCF map shows Doppler ambiguities separated by $1/T_B$ with amplitudes decaying at high Doppler frequencies.

This is clearly the case observed in Figure 17. Notice that as the batch duration decreases, the Doppler ambiguities spread accordingly. In addition, the cancellation notch is widened and the target SNR is progressively reduced. Further decreasing T_B would allow the undesired structures to be moved out of the Doppler range of interest. However this would also yield a more severe slowly-moving target removal and additional adaptivity loss since the disturbance characteristics would be estimated on few signal samples.

The above limitation of the ECA-B is apparent in PCL local area applications where it is quite typical to deal with slowly moving targets. However, similar effects can be observed also in longer range applications, especially when exploiting signals of opportunity in the VHF or UHF band since there is a reasonable probability to observe a target at low Doppler frequency. This certainly applies to the maritime surveillance application where small boats or docked vessels might show very limited velocities. However, even in ATC applications, targets could be present moving mainly along the cross-range direction.

These considerations exacerbate in severe scenarios (i.e. those characterized by rapidly varying disturbance characteristics, possibly induced by co- and inter-channel interference, severe multipath, transmitter dependent effects, etc.) where it may be necessary to frequently update the filter coefficients to effectively remove the disturbance. In fact, operating with the ECA-B this is tantamount to the request for batches of extremely small dimension. Unluckily, this results in a considerable widening of the cancellation filter notch thus including even fast moving targets.

3.4.4 ECA-SLIDING TECHNIQUE

Based on the previous analysis, when the ECA-B approach is applied, special attention should be devoted to the selection of the batch duration as it affects both the capability to effectively remove the disturbance contributions possibly showing a non-stationary behavior and the possibility to nicely preserve the target echo.

Specifically the two requirements above might set opposite constraints on the selection of T_B. Long T_B should be selected to reduce the minimum detectable velocity and to limit the adaptivity loss. In contrast, short T_B should be preferred to be effective against disturbance with rapidly varying characteristics and to move the target Doppler ambiguities out of the observed Doppler extent.

To overcome this limitation, we propose a sliding version of the ECA (ECA-S) which operates over partially overlapped signal fragments (see Figure 18). This allows to decouple the selection of the batch duration exploited for the filter estimation and the update rate of the filter coefficients so that the requirements above could be more flexibly traded for.

Basically a new parameter is introduced, T_S, that represents the signal fragment processed using a given filter estimate; apparently, T_S also coincides with the temporal separation between consecutive updates of the filter coefficients. Thus ECA-S output at the *l*-th fragment is written as

$$s_{ECA-S}[n] = s_s[n] - \sum_{k=0}^{K-1} \alpha_k^{(l,T_A)} s_r[n-k]$$
$$n = lN_S, \dots, (l+1)N_S - 1;\ l = 0, \dots, B_S - 1 \tag{27}$$

where N_S is the dimension of each fragment (i.e. $N_S = T_S f_s$), $B_S = \left\lfloor \frac{N}{N_S} \right\rfloor$ is the number of consecutive fragments in the CPI, and $\boldsymbol{\alpha}^{(l,T_A)} = \left[\alpha_0^{(l,T_A)}\ \alpha_1^{(l,T_A)}\ \cdots\ \alpha_{K-1}^{(l,T_A)}\right]^T$ are the current filter coefficients. The latter are adaptively estimated on a longer signal fragment of duration $T_A = N_A/f_s$, symmetrically taken around the current signal fragment to be processed (see Figure 18). Basically $\boldsymbol{\alpha}^{(l,T_A)}$ are evaluated as

$$\boldsymbol{\alpha}^{(l,T_A)} = \left[\mathbf{S}_r^{(l,T_A)H} \mathbf{S}_r^{(l,T_A)}\right]^{-1} \mathbf{S}_r^{(l,T_A)H} \mathbf{s}_s^{(l,T_A)} \tag{28}$$

where the surveillance vector is given by

$$\mathbf{s}_s^{(l,T_A)} = \left[s_s\left[lN_S + \frac{N_S - N_A}{2}\right], s_s\left[lN_S + \frac{N_S - N_A}{2} + 1\right], \cdots, s_s\left[lN_S + \frac{N_S + N_A}{2} - 1\right]\right]^T \quad (N_A \times 1) \tag{29}$$

and $\mathbf{S}_r^{(l,T_A)}$ is a $N_A \times K$ matrix collecting the delayed copies of the corresponding reference signal fragment of duration T_A. Obviously, with the ECA-B approach we have $T_B = T_S = T_A$.

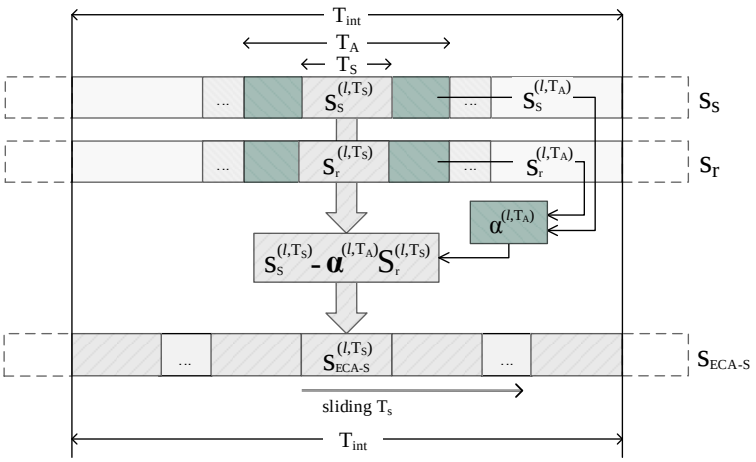

Figure 18 Block diagram of ECA-S.

Based on the ECA-S cancellation algorithm, the theoretical derivation in 3.4.3 can be repeated under the same simplifying hypotheses. To this purpose, let us collect in vectors $\mathbf{s}_s^{(l,Ts)}$ and $\mathbf{s}_r^{(l,Ts)}$ the N_S samples of the *l*-th fragment of the surveillance and the reference signals, respectively:

$$\mathbf{s}_{s/r}^{(l,Ts)} = \left[s_{s/r}[lN_S],\ s_{s/r}[lN_S + 1], \cdots, s_{s/r}[(l+1)N_S - 1]\right]^T \quad (N_S \times 1) \tag{30}$$

These vectors include the N_S samples that are processed using the same filter weights according to (27). Therefore, eq. (27) can be written in matrix notation as:

$$\mathbf{s}_{ECA-S}^{(l,Ts)} = \mathbf{s}_s^{(l,Ts)} - \alpha_0^{(l,T_A)}\mathbf{s}_r^{(l,Ts)} \tag{31}$$

where

$$\alpha_0^{(l,T_A)} = \frac{1}{\left\|\mathbf{s}_r^{(l,T_A)}\right\|^2}\mathbf{s}_r^{(l,T_A)^H}\mathbf{s}_s^{(l,T_A)} = \frac{1}{|A_r|^2\|\mathbf{d}^{(l,T_A)}\|^2}\left[A_r^*A_t\mathbf{d}^{(l,T_A)^H}\mathbf{d}_{f_d}^{(l,T_A)} + A_r^*A_c\left\|\mathbf{d}^{(l,T_A)}\right\|^2 + A_r^*\mathbf{d}^{(l,T_A)^H}\mathbf{w}_s{}^{(l,T_A)}\right] \tag{32}$$

being $\mathbf{d}^{(l,T_A)}$ and $\mathbf{d}_{f_d}^{(l,T_A)}$ the $N_A \times 1$ vectors containing the *l*-th overlapped batch of duration T_A of the direct signal and its Doppler shifted version.

Therefore, proceeding as in (17)-(18), we evaluate the output of the range-Doppler map for the range bin of the target at the generic Doppler frequency f_0:

$$\chi[f_0] = \sum_{l=0}^{B_S-1} A_t\mathbf{d}_{f_0}^{(l,T_S)^H}\mathbf{d}_{f_d}^{(l,T_S)} - \sum_{l=0}^{B_S-1}\frac{A_t}{\|\mathbf{d}^{(l,T_A)}\|^2}\mathbf{d}^{(l,T_A)^H}\mathbf{d}_{f_d}^{(l,T_A)}\mathbf{d}_{f_0}^{(l,T_S)^H}\mathbf{d}^{(l,T_S)} + \\ + \sum_{l=0}^{B_S-1}\left[\mathbf{d}_{f_0}^{(l,T_S)^H}\mathbf{w}_s{}^{(l,T_S)} - \frac{1}{\|\mathbf{d}^{(l,T_A)}\|^2}\mathbf{d}_{f_0}^{(l,T_S)^H}\mathbf{d}^{(l,T_S)}\mathbf{d}^{(l,T_A)^H}\mathbf{w}_s{}^{(l,T_A)}\right] \tag{33}$$

Again, the first target contribution in (33) results:

$$\chi_I[f_0] = A_t\frac{sin[\pi(f_d - f_0)\,N/f_s]}{sin[\pi(f_d - f_0)/f_s]}e^{j\pi(f_d-f_0)(N-1)/f_s} \tag{34}$$

This coincides with eq. (20) since this term represents the ideal target contribution at the output of the 2D-CCF and it is not affected by the cancellation stage.

The second term in eq. (33) can be written as:

$$\chi_{II}[f_0] = A_tN_AN_S\sum_{l=0}^{B_S-1}\frac{1}{\|\boldsymbol{d}^{(l,T_A)}\|^2}g^{(l,T_A)}(f_d)\left[g^{(l,T_S)}(f_0)\right]^* \tag{35}$$

where

$$g^{(l,T_A)}(f) = \mathbf{d}^{(l,T_A)^H}\mathbf{d}_f^{(l,T_A)}/N_A = \frac{1}{N_A}\sum_{n=lN_S+\frac{N_S-N_A}{2}}^{lN_S+\frac{N_S+N_A}{2}-1}|d[n]|^2\,e^{j2\pi fn/f_s} = g^{(0,T_A)}(f)e^{j2\pi flN_S/f_s} \tag{36}$$

and

$$g^{(l,T_S)}(f) = \mathbf{d}^{(l,T_S)^H}\mathbf{d}_f^{(l,T_S)}/N_S = \frac{1}{N_S}\sum_{n=lN_S}^{(l+1)N_S-1}|d[n]|^2\,e^{j2\pi fn/f_s} = g^{(0,T_S)}(f)e^{j2\pi flN_S/f_s} \tag{37}$$

being

$$g^{(0,T_A)}(f) = \frac{1}{N_A}\frac{sin[\pi fN_A/f_s]}{sin[\pi f/f_s]}e^{j\pi f(N_S-1)/f_s} \tag{38}$$

and

$$g^{(0,T_S)}(f) = \frac{1}{N_S}\frac{sin[\pi f N_S/f_s]}{sin[\pi f/f_s]} e^{j\pi f(N_S-1)/f_s} \tag{39}$$

Therefore eq. (35) becomes:

$$\chi_{II}[f_0] = A_t N_S g^{(0,T_A)}(f_d)\left[g^{(0,T_S)}(f_0)\right]^* \frac{sin[\pi(f_d - f_0)\, B_S N_S/f_s]}{sin[\pi(f_d - f_0)\, N_S/f_s]} e^{j\pi(f_d - f_0)\, N_S(B_S-1)/f_s} \tag{40}$$

As is apparent, this term still include a $\sin(B_S x)/\sin(x)$ factor; however in this case the period is set by the filter update rate. In other words, operating with the ECA-S approach, the Doppler ambiguities associated to low Doppler targets are expected to appear with Doppler separation equal to $\frac{f_s}{N_S} = \frac{1}{T_S}$. Therefore, a reasonable strategy to design this parameter is to select T_S so that to move out of the Doppler range of interest $[-f_{Dmax}, f_{Dmax}]$ the undesired structures arising from the batch processing of the received signals. By imposing this condition for all the targets belonging to the cancellation notch area, we obtain $T_S < \left(f_{Dmax} + \frac{1}{2T_A}\right)^{-1}$. A good cancellation capability can be still guaranteed by acting on the other independent parameter T_A. Specifically this can be selected according to the analysis reported in 3.4.2, in order to allow remarkable cancellation performance against the time-varying characteristics of the disturbance for the specific operative scenario; obviously, this should be partly traded with the minimum detectable velocity to be guaranteed.

In fact the target peak amplitude (i.e. for $f_0 = f_d$) at the output of the 2D-CCF can be evaluated in this case as:

$$\chi[f_d] = \chi_I[f_d] - \chi_{II}[f_d] = A_t N\left\{1 - \frac{1}{N_S N_A}\frac{sin[\pi f_d N_S/f_s]}{sin[\pi f_d/f_s]}\frac{sin[\pi f_d N_A/f_s]}{sin[\pi f_d/f_s]}\right\} \tag{41}$$

As is apparent, the target SNR loss, and in turn, the cancellation notch width, depends on both T_A and T_S.

Notice that if the ECA-B operates with $T_B = T_S$ aiming at excluding the ambiguities from the observed Doppler region, a wide cancellation notch could be achieved; in contrast the ECA-S yields the possibility to significantly narrow the cancellation notch by properly selecting $T_A > T_S$.

However, when the batch duration of the ECA-B is selected as $T_B = T_A$ to maximize the cancellation capability, the ECA-S typically yields a wider Doppler extent of the cancellation area with respect to the ECA-B since the T_S value required to remove Doppler ambiguities is much smaller than T_A (see eqs. (41) and (25)). In other words, operating with the ECA-S allows to trade the ambiguities removal with a limited SNR loss. In turn, the latter can be traded with a small cancellation loss if T_A is slighly increased with respect to the initial choice $T_A = T_B$.

Based on the considerations above, we here address the design of the ECA-S parameters with reference to the different case studies considered in this paper (see 3.4.2.A, B and C).

When the FM-based PCL is employed for ATC applications, the batch duration exploited to estimate the filter coefficients can be selected as $T_A = 25$ ms which was experimentally verified to yield remarkable and quite stable cancellation performance in the considered scenario (see Figure 13). In contrast, assuming a maximum velocity $v_{max} = 400$ m/s ($f_{Dmax} = 126$ Hz with the exploited FM radio channel at 94.5 MHz), we might set $T_S < 6.8$ ms.

In the case of a DVB-T based PCL for maritime surveillance, again the batch duration T_A can be independently set to maximize the cancellation performance: for example $T_A = 0.1$ s is a reasonable choice according to the analysis in 3.4.2.B. Furthermore, the maximum observed velocity can be limited to $v_{max} = 20$ m/s so that $T_S < 17.4$ ms allows to set the first Doppler ambiguity out of the observed area in our case studies ($f_{Dmax} < 52.4$ Hz with the DVB-T channels exploited in the considered data sets).

Finally, in the WiFi-based PCL case, a batch duration $T_A = 50$ ms has been shown to be a good compromise for effective disturbance removal and reasonable target echo preservation. Moreover, as the maximum Doppler frequency observed is $f_{Dmax} = 70$ Hz, we might set $T_S < 12.5$ ms.

3.4.5 PERFORMANCE ANALYSIS AGAINST REAL DATA

In this section, the improvement achieved by the proposed ECA-S approach is investigated in term of detection performance of the PCL system. This analysis allows us to gain a further insight into the operation of both the ECA-B and the ECA-S and to clearly demonstrate how the proposed modification recovers for the limitations identified in 3.4.3. We refer to the same case studies considered in 3.4.2.

A. EXPERIMENTAL RESULTS FOR THE FM-BASED PCL IN ATC APPLICATIONS

Based on our experimental results ([17],[52]), in this application quite long batch durations can be used normally for adaptive filter evaluation; this yields narrow cancellation notches compared to the typical high Doppler values of the aerial targets even operating with an ECA-B approach. As a consequence the adverse effects investigated in 3.4.3 occur with low probability, and, when this is the case, they appear for a very limited time thus not compromising the overall results if effective post-processing stages are implemented.

Nevertheless, we have shown that in specific condition, i.e. when operating against severe scenarios (namely those characterized by rapidly varying disturbance characteristics, possibly induced by co- and inter-channel interference, severe multipath, transmitter dependent effects, etc.) it may be necessary to operate the ECA-B with batches of extremely small dimension to effectively remove the disturbance. As a result, the undesired effects shown in the previous sections might arise limiting the surveillance capability of the PCL system.

The above considerations are experimentally verified with reference to the data set described in 3.4.2.A. All the available data files have been processed according to a basic PCL processing scheme that includes: (i) disturbance (direct signal and multipath) cancellation using different ECA versions with K=140 taps; (ii) evaluation of the 2D-CCF between the surveillance and the reference signal over a CPI of 1 s; (iii) target detection via a cell-average constant false alarm rate (CA-CFAR) threshold with a nominal probability of false alarm $P_{fa}=10^{-4}$; (iv) track initiation using a conventional nearest neighbor association scheme with a '2 out of 2' strategy. Figure 19 reports the results obtained for 100 consecutive data files.

In particular, using the conventional ECA for the disturbance removal, the results are those reported as red dots in Figure 19(a), where black dots represent the available air-truth. Due to the high non-stationarity of the environment, resorting to the ECA-B approach allows a better cancellation capability (see 3.4.2.A) that turns out to guarantee a better continuity in target detection. As an example, the results obtained with $\mathrm{T_B} = 25$ ms are reported in Figure 19(b). As is apparent complete plot sequences are detected and additional target tracks are correctly identified. However, it is worth noticing that operating with $\mathrm{T_B} = 25$ ms yields a number of false tracks due to Doppler ambiguities at $1/\mathrm{T_B}$ Hz distance from the corresponding true target track.

Figure 19(c) reports the results obtained after the disturbance removal with the ECA-S operating with $T_S = 6.25$ ms, to remove Doppler ambiguities appearing in the area of interest, and $T_A = 25$ ms, to guarantee an effective disturbance cancellation in the observed non-stationary environment. Again, a tremendous improvement is observed with respect to the conventional ECA whereas comparable detection performance is obtained with respect to the application of the ECA-B approach operating with $T_B = 25$ ms. However, the possibility to separately set the filter updating rate allows to avoid the many false tracks appearing in Figure 19(b).

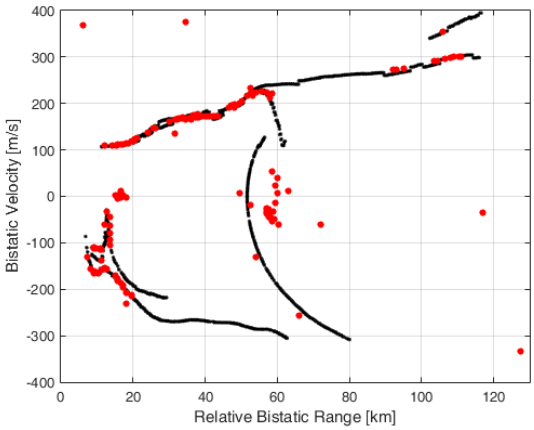

(a)

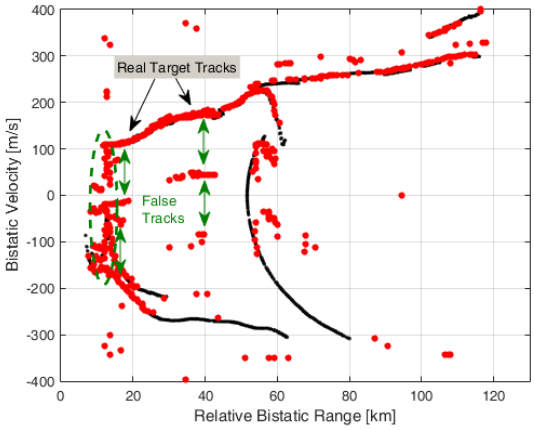

(b)

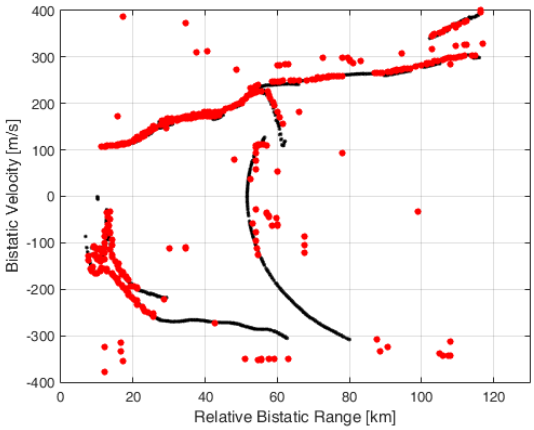

(c)

Figure 19 Detection results over the bistatic range-velocity plane for 100 consecutive scans when disturbance removal is performed via: (a) the conventional ECA; (b) the ECA-B with $T_B = 25$ ms; (c) the ECA-S with $T_{\mathrm{A}} = 25$ ms and $T_{\mathrm{S}} = 6.25$ ms.

B. EXPERIMENTAL RESULTS FOR THE DVB-T-BASED PCL

As seen in Figure 14, some maritime operative scenarios may be highly time varying thus requiring the cancellation filter coefficients to be estimated over a much smaller duration than the CPI in order to adequately lower the

disturbance power in the surveillance signal. Therefore, due to the low speed of many naval targets, operating with an ECA-B approach might yield the limitations discussed in 3.4.3.

This is shown in Figure 20 with reference to the data sets mentioned in 3.4.2.B. All the available data files have been fed into a signal processing chain composed by: (i) prefiltering of the reference signal for ambiguity function control [28]; (ii) disturbance cancellation using different ECA versions with $K = 1000$ taps; (iii) evaluation of the 2D-CCF between the surveillance and the reference signal over a CPI of 1 s; (iv) target detection via a CA-CFAR threshold with a nominal probability of false alarm P_{fa}=10^{-4}; (v) '2 out of 2' criterion to integrate the detection obtained at the 2 available surveillance channels; (vi) track initiation stage using a conventional nearest neighbor association scheme with a '2 out of 2' strategy.

Figure 20 reports the comparison of the results obtained over 90 consecutive data files of Data Set 1 after cancellation with ECA-B and ECA-S. Red dots represent PCL detections while blue tracks represent the ground truth provided by AIS. As is apparent, ECA-B operating with $T_B = 0.1$ s (see Figure 20(a)) gives rise to several false tracks that may prevent a proper awareness of the number of vessels in the surveilled zone. They are spaced in the bistatic Doppler dimension at $1/T_B$ Hz that results in 6.22 m/s spacing in the bistatic velocity domain (at the considered carrier frequency). Figure 20(b) shows the results for disturbance removal with ECA-S operating with $T_A = 0.1$ s and $T_S = 15$ ms. As is apparent the proposed approach allows the complete removal of the false tracks appearing between 24 and 30 km; detections wrapped in the dotted ellipse have been attributed to an interfering transmitter and have been verified to be revealed also after cancellation via conventional ECA. Plot sequences at 7-15 km and at 16-20 km are likely to be traffic of opportunity not equipped with AIS.

Based on other similar analyses, we might conclude that the ECA-S yields similar cancellation performance with respect to the previous batch version of the ECA, and this results in a comparable capability of detecting real target tracks. Furthermore, the ECA-S allows to recover for the limitations of the ECA-B arising when operating against slowly moving targets so that it can be regarded as a better solution for disturbance removal also in this application.

Therefore, in the following we focus on the comparison of ECA-S with the conventional ECA aiming at understanding the benefits deriving from a batch approach in different maritime scenarios.

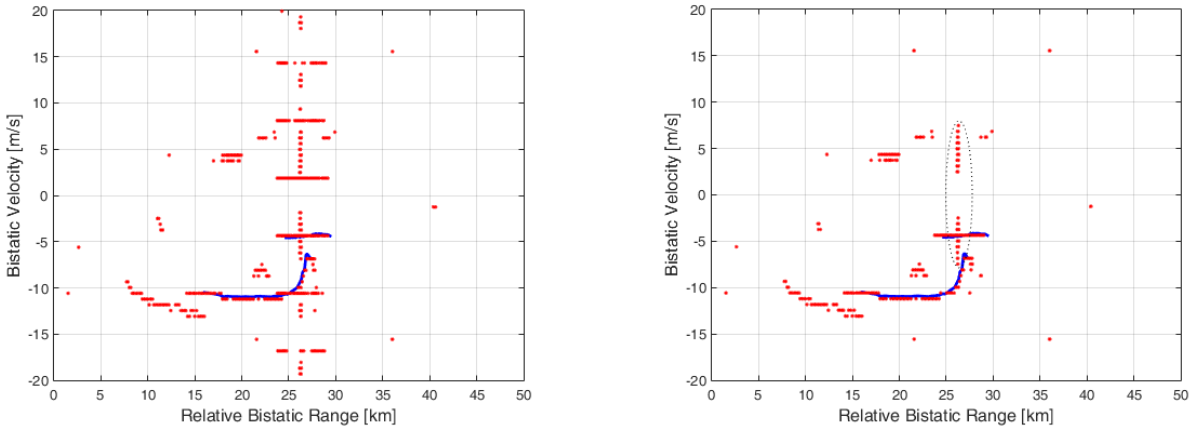

(a) (b)

Figure 20 Detection results over the bistatic range-velocity plan for 90 consecutive data files of Data Set 1 with disturbance removal performed via: (a) ECA-B with $T_B = 0.1$ s; (b) ECA-S with $T_A = 0.1$ s and $T_S = 15$ ms.

To this purpose Figure 21 reports some examples of detection results obtained at different acquisitions; specifically, in each figure, an enlarged view is shown around specific targets of opportunity. Figure 21(a-b) reports the detections over 90 data files for a cargo ship observed in Data Set 1 at very long bistatic range (>200 km); Figure 21(a) is obtained

after the application of ECA while Figure 21(b) reports the results of ECA-S. We recall that Data Set 1 was collected in a quite stationary scenario so that the performance yield by the two approaches are very similar, even though a slight better continuity is obtained when operating with ECA-S.

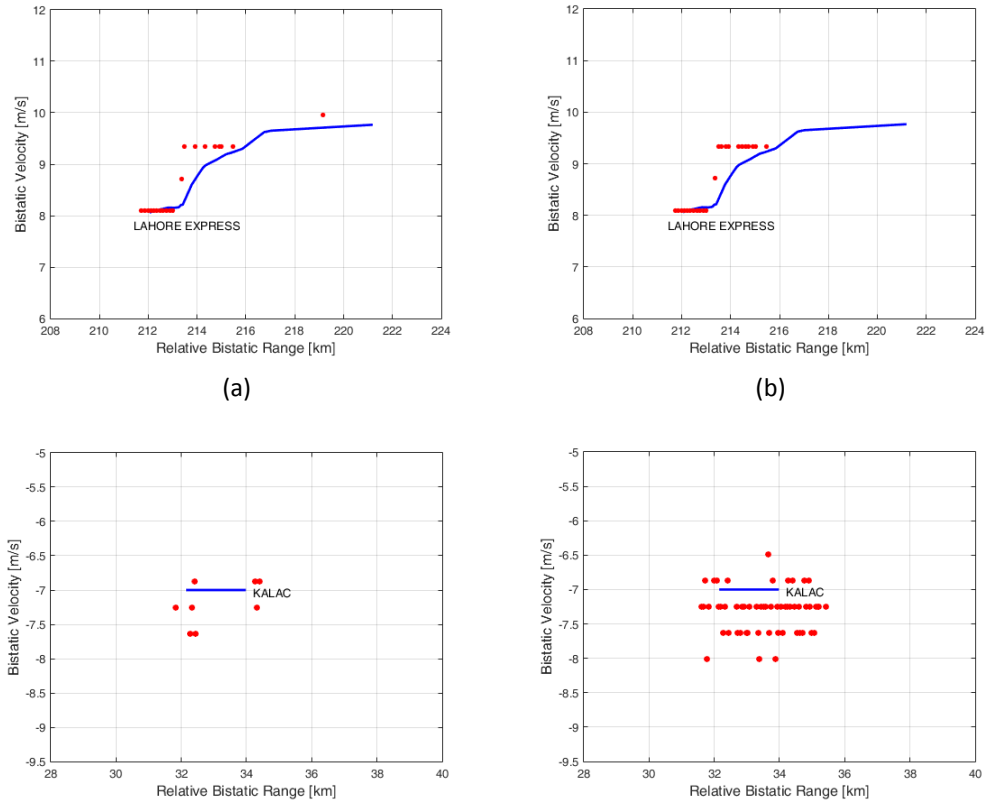

Figure 21 Comparison of detection results with ECA and ECA-S for specific targets of opportunity: (a-b) Cargo ship detected in Data Set 1 operating with ECA and ECA-S, (c-d) Sailing vessel detected in Data Set 6 operating with ECA and ECA-S.

Figure 21(c-d) report the results over 66 data files of Data Set 6 which accounts for a highly varying disturbance scenario. In this case tremendous advantage offered by ECA-S is quite apparent since it allows to significantly improve the detection rate for the considered 22 m sailing vessel at medium ranges.

The number of correct detections obtained with the ECA and the ECA-S in the above examples has been reported in Table 6 (first and last line) along with other examples from the available data sets. In each case we indicate the considered Data Set and provide details about the target of opportunity (name, type, size, bistatic range-velocity coordinates). The number of correct detections obtained after ECA and ECA-S are compared to the total number of available data files. Cancellation via ECA provides very similar detection performance with respect to ECA-S when the system operates in a quasi-stationary scenario (see results obtained for Data Set 1). Remarkable detection rates could be obtained after the ECA even in non-stationary scenarios (i.e. Data Sets 3-6); however, in this case, the size of the target and its distance from the receiver play an important role to ensure the same performance. In fact, a comparable detection continuity is observed for big-sized targets at short/medium ranges. In contrast, ECA-S dramatically increase the number of correct detections against small targets such as fishing or sailing vessels (see for example targets Nuovo Ciclone and Kalac).

Table 6. Detection results comparison against various targets of opportunity in different acquisitions.

							Associated Detections	
Data set	Target	Type	Size [m]	Bistatic range [km]	Bistatic velocity [m/s]	Available scans	ECA	ECA-S
1	Lahore Express	Cargo	259x32	213	9	90	25	27
1	Besiktas GH	Tanker	123x19	140	-12,5	90	77	79
3	Vastaso	Tanker	176x31	17	1	42	42	42
3	Camilla	Container	184x25	16	-4	42	15	19
3	SS Trinità	Fishing	26x6	12,5	-1,5	42	8	12
4	Alida S	Cargo	116x16	37	7,5	43	2	41
5	Alida S	Cargo	116x16	29	6	45	32	43
5	Nuovo Ciclone	Fishing	22x6	34	-3	45	0	16
6	Kalac	Sailing	14x5	33	-7	66	11	61

B.1. ADDITIONAL RESULTS FOR THE DVB-T BASED PCL

In this paragraph some other results will be shown and additional considerations will be provided for the considered application. Figure 22-Figure 24 show the PBR detections, in red, and the ground truth track (blue) of three opportunity targets after disturbance cancellation via ECA or ECA-S. Shown detections are those at the output of a '2-out-of-2' track initiation scheme; beside each red dot a number indicating the scan identifier is plotted.

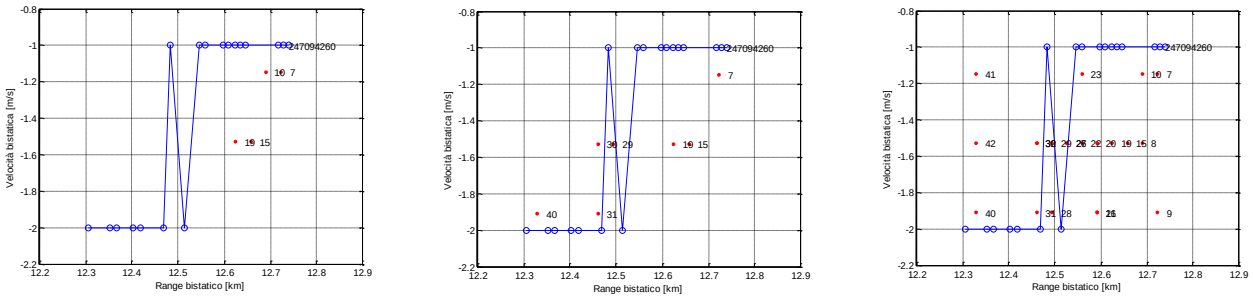

(a) (b) (c)

Figure 22 Detections relative to the opportunity target 'SS Trinità'. Disturbance cancellation via (a) ECA, (b) ECA-S with $T_A = 0.1$ s and $T_S = 15$ ms, (c) ECA-S with $T_A = 0.2$ s and $T_S = 15$ ms.

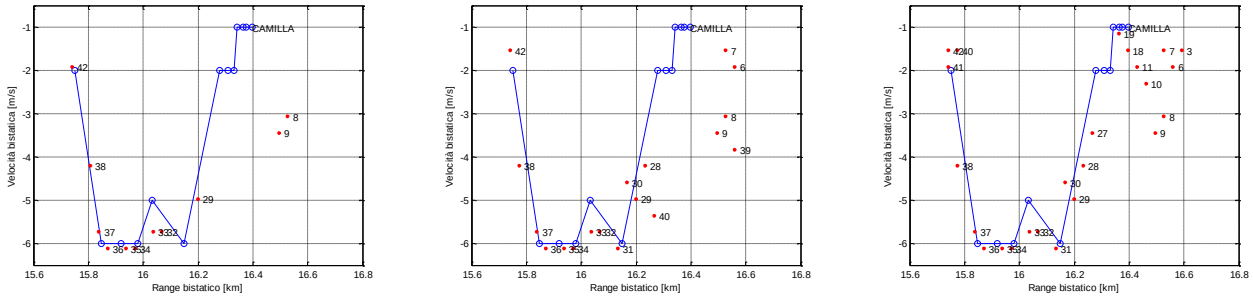

(a) (b) (c)

Figure 23 Detections relative to the opportunity target 'Camilla'. Disturbance cancellation via (a) ECA, (b) ECA-S with $T_A = 0.1$ s and $T_S = 15$ ms, (c) ECA-S with $T_A = 0.2$ s and $T_S = 15$ ms.

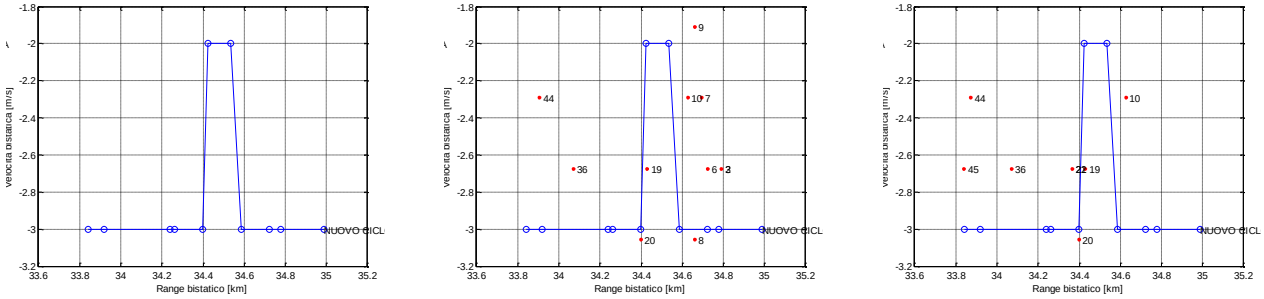

(a) (b) (c)

Figure 24 Detections relative to the opportunity target 'Camilla'. Disturbance cancellation via (a) ECA, (b) ECA-S with $T_A = 0.1$ s and $T_S = 15$ ms, (c) ECA-S with $T_A = 0.2$ s and $T_S = 15$ ms.

In Figure 25, some interesting results are reported regarding an opportunity target not equipped with AIS. It has been visually identified as a motorboat maneuvering at few kilometers from the harbor. It can be seen in the bistatic plane the parabolic-like trajectory of the target. As this target as well as the others in the scene were buried in a highly non-stationary scenario, it has been necessary to recur to disturbance cancellation via ECA-S to enhance the overall performance of the system. However, it implied the application of a wider filter notch with respect to cancellation via ECA, resulting in a lack of detections when using ECA-S.

This situation represents a drawback of the proposed technique when dealing with targets moving at very low bistatic velocities. Nevertheless the detection capability of the system is not compromised for such target and is much increased for faster targets. It is worth noting that Figure 25 refers to Data set 4 in which there is a target that had much benefit for ECA-S (as observable in Table 6).

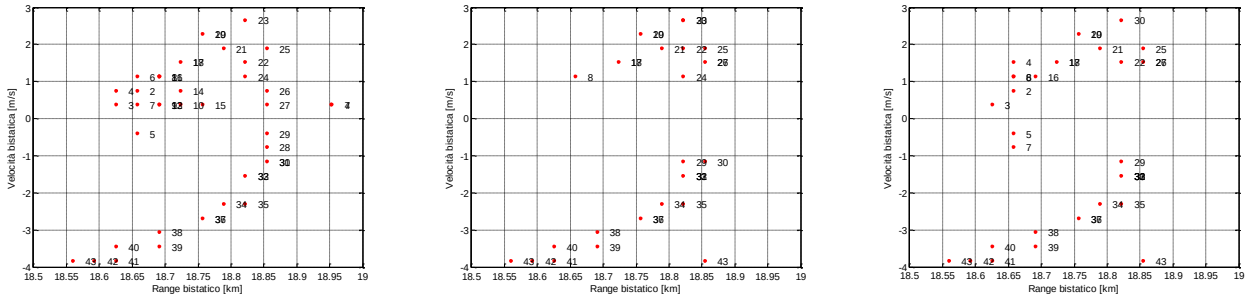

(a) (b) (c)

Figure 25 Detections relative to an opportunity target not equipped with AIS. Disturbance cancellation via (a) ECA, (b) ECA-S with $T_A = 0.1$ s and $T_S = 15$ ms, (c) ECA-S with $T_A = 0.2$ s and $T_S = 15$ ms.

C. EXPERIMENTAL RESULTS FOR THE WIFI-BASED PCL

The effectiveness of the sliding version of the ECA is further demonstrated in this sub-section for WiFi-based PCL. Specifically Figure 26 shows the detection results obtained with ECA and ECA-S for the same data set considered in 3.4.3 (test against a vehicular target moving in the cross-range direction).

The data collected has been processed according to the WiFi-based passive radar processing scheme presented in [54]. In particular, the cancellation stage is performed by adopting the ECA-B or the ECA-S over a range of 500 m. A CPI of 0.2 s is then used to evaluate the bistatic range-velocity map over consecutive portions of the acquired signals

(frames) with a fixed displacement of 0.1 s (10 frames per second are thus obtained); finally, target detection is performed by resorting to a standard cell-average CFAR threshold with a probability of false alarm equal to 10^{-5}.

In Figure 26 we report the raw detections over the bistatic range/velocity plane collected along the whole acquisition (20 seconds). Specifically Figure 26(a) has been obtained after cancellation via ECA-B operating with $T_B = 50$ ms while Figure 26(b) is the result of the application of the ECA-S. Notice that for ECA-S, the adopted parameters are $T_A = 50$ ms and $T_S = 3$ ms; in fact, for a practical application, we set the filter update rate to be equal to the beacon emission rate of the exploited access point, i.e. the filter coefficients are updated beacon by beacon.

As is apparent, in both figures, in addition to the target returns (the cross-range movement of the target results in a parabolic sequence of detections over the range/velocity plane with vertex in (40;0)), there are also the double bounce returns caused by the reflection of the target echo over the metallic fence delimiting the parking area (parabolic sequence with vertex in (140;0)) and false alarms.

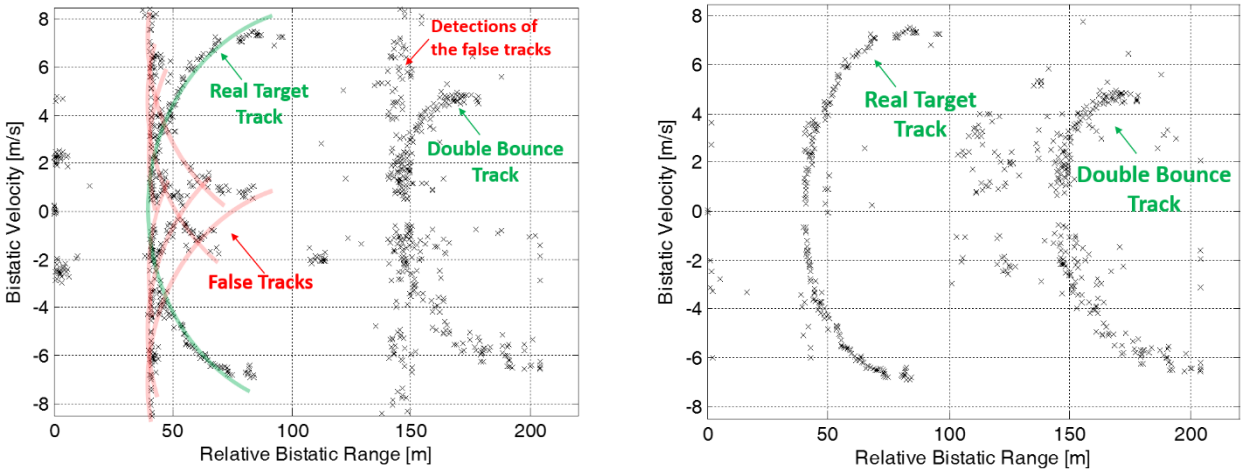

(a) (b)

Figure 26 Detection results over the bistatic range-velocity plane when disturbance removal is performed via: (a) the ECA-B with $T_B = 50$ ms; (b) the ECA-S with $T_A = 50$ ms and $T_S = 3$ ms.

In addition, operating with the ECA-B yields a number of false plots due to Doppler ambiguities with 2.3 m/s spacing (corresponding to $1/T_B$ = 20 Hz). These ambiguities arise both from the main target echo and from its double-bounce return; however they are more evident in the first case due to the higher SNR of the originating echo. False tracks are usually discontinuous thanks to the masking effect of the real target echo at the detection stage. Nevertheless, they are quite apparent and might significantly limit the capability to identify and effectively track the true targets.

In contrast, we observe that the ECA-S allows to move the Doppler ambiguities out of the Doppler extent of interest while guaranteeing largely comparable detection capability against the true target echoes.

3.4.6 CONSIDERATIONS ON THE COMPUTATIONAL COST

The advantages yield by the ECA-S are paid in terms of computational load since the filter weights computation is repeated a greater number of times within the CPI with respect to both the ECA and the ECA-B. However, we show that the required computations can be limited if proper expedients are adopted.

Based on eqs. (10)-(11), (12)-(13), and (27)-(28), the computational load of any version of the ECA can be decomposed in two main contributions:

1) the cost $C_1(K, N_x)$ required for the adaptive evaluation of the filter coefficients; this depends on the number of taps and on the length of the signal fragment used for adaptive weights estimation (namely, $N_x = N$ for ECA, $N_x = N_B$ for ECA-B, and $N_x = N_A$ for ECA-S).

2) the cost $C_2(K, N_y)$ required for the application of the filter to the surveillance signal; this again depends on *K* and on the length of the signal fragment processed with a given filter estimate (namely, $N_y = N_x$ for ECA and ECA-B, whereas $N_y = N_S$ for ECA-S).

Therefore the computational load for ECA is simply

$$C_{ECA}(K, N) = C_1(K, N) + C_2(K, N) \tag{42}$$

In contrast, when operating with the ECA-B and ECA-S approaches, the two tasks above are performed against smaller signal fragments but they are repeated at each considered, possibly overlapped, batch, i.e.

$$C_{ECA-B}(K, N_B) = B\,[C_1(K, N_B) + C_2(K, N_B)] \tag{43}$$

$$C_{ECA-S}(K, N_A, N_S) = B_S\,[C_1(K, N_A) + C_2(K, N_S)] \tag{44}$$

Notice that the direct implementation of eqs. (11), (13), and (28), requires $C_1(K, N_x) = O[4N_xK^2 + 4K^3]$ FLOPs (FLoating-point Operations; here we assume that a complex add involves 2 FLOPs and a complex multiplication involves 6 FLOPs). The filter application is much less computationally expensive since it requires $C_2(K, N_y) = 8\mathrm{N_y K}$ FLOPs with $N_y \leq N_x$. Therefore $C_1(K, N_x)$ drives the final cost of the cancellation stage and, depending on the values of the relevant parameters, the number of required FLOPs could rapidly increase so that this stage might become the bottleneck for a real-time operation. This especially applies to the ECA-S approach where the filter computation is repeated many times along the CPI (we recall that in all the considered applications $B_S > B$ and $N_A \geq N_B$).

As is apparent, appropriate expedients should be devised to limit the computational load of the adaptive filter evaluation with respect to the direct implementation of eqs. (11), (13), and (28).

To this purpose, let us rewrite eq. (11) as

$$\boldsymbol{\alpha} = \mathbf{M}^{-1}\mathbf{c} \tag{45}$$

where $\mathbf{M} = \mathbf{S}_r^{\mathrm{H}}\mathbf{S}_r$ and $\mathbf{c} = \mathbf{S}_r^{\mathrm{H}}\mathbf{s}_s$. The following considerations identically apply to other ECA approaches with an obvious change of notation. Based on the definition of matrix $\mathbf{S}_r$, the *k*-th element of vector $\mathbf{c}$ can be evaluated as:

$$c[k] = \sum_{n=0}^{N-1} s_r^H[n-k]s_s[n] \quad k = 0,..,K-1 \tag{46}$$

Notice that it coincides with the *k*-th sample of the cross-correlation between the reference and the surveillance signals. Therefore the whole vector $\mathbf{c}$ can be computed at FFT speed by performing the FFT of $\boldsymbol{s}_s$ and $\boldsymbol{s}_r$, evaluating the IFFT of their conjugate product, and then selecting the useful samples.

Similarly, the [*k,l*]-th element of matrix $\mathbf{M}$ can be rewritten as:

$$M[k,l] = \sum_{n=0}^{N-1} s_r^H[n-k]s_r[n-l] \cong m[k-l] \qquad k,l = 0,..,K-1 \tag{47}$$

where, for the last equality, we neglect the border effect or, equivalently, we assume that the reference signal is locally stationary so that its autocorrelation depends only on the time-distance between delayed replicas. Apparently this approximation is largely acceptable when $K \ll N$, as for typical applications. In addition we observe that $m[k] = m^*[-k]$. Therefore we conclude that $\mathbf{M}$ is an Hermitian positive definite Toeplitz matrix so that it is completely defined by its first row (or column). Consequently, matrix $\mathbf{M}$ can be computed using the same approach

adopted for vector **c**, by exploiting the FFT of $\boldsymbol{s}_r$ available from the previous step. Overall, the computation of **M** and **c** requires $17.5N\log_2(N) + 8.5N$.

Once the required matrices have been computed, the direct implementation of (45) would require the inversion of a $K \times K$ matrix. To limit the corresponding computational load, we might observe that vector $\boldsymbol{\alpha}$ is the solution of an Hermitian positive definite Toeplitz system $\mathbf{M}\boldsymbol{\alpha} = \mathbf{c}$. This can be efficiently solved by resorting to the Levinson algorithm which requires approximately $16K^2$ FLOPs [56]. Therefore, for a typical number *K* of taps, a significant computational load can be saved with respect to the $O(4K^3)$ complexity of conventional matrix inversion.

Therefore, generalizing the result to different versions of the ECA, the number of FLOPs required for the adaptive filter evaluation has been reduced down to $C_1(K, N_x) = 17.5N_x\log_2(N_x) + 8.5N_x + 16K^2$.

Similar expedients can be adopted to further limit the computational load required for filter application. To this purpose eq. (10) is rewritten as $s_{ECA}[n] = s_s[n] - y[n]$ where

$$y[n] = \sum_{k=0}^{K-1} \alpha_k s_r[n-k] \quad n = 0, \dots, N-1 \tag{48}$$

is the output of the convolution between the reference signal and the filter. Again, this can be evaluated in the frequency domain by performing the FFT of $\boldsymbol{s}_r$ and the zero-padded version of $\boldsymbol{\alpha}$, and then evaluating the IFFT of their product. Therefore, for the generic ECA version, the computation of the output with given filter coefficients requires $C_2(K, N_y) = 15N_y\log_2(N_y) + 8N_y$. Notice that if $N_y = N_x$ (as for ECA and ECA-B), the FFT of the reference signal fragment to be processed is available from the previous step so that $C_2(K, N_y)$ can be further reduced down to $C_2(K, N_y) = 10N_y\log_2(N_y) + 8N_y$.

The overall complexity of the different ECA versions is reported in Table 7. As is apparent, for typical values of the relevant parameters, the ECA-S is still the most demanding approach in term of computational load. However, its complexity has been significantly reduced with respect to the direct implementation of eqs. (27)-(28). In many cases, such reduction might enable a real-time operation or, at least, remove the cancellation stage from the role of bottleneck of the PCL processing chain.

This is shown in Figure 27 where the complexity of the different ECA versions is compared to the number of FLOPs required for the evaluation of a Range-Doppler map according to an efficient optimum algorithm. Specifically we refer to the case of DVB-T based PCL for maritime surveillance application as it represents the most demanding application in tem of computational burden. Specifically, we consider the Correlation-FFT algorithm for the 2D-CCF evaluation since it represents the most efficient solution when DVB-T transmissions are exploited [27]. The corresponding computational load is reported in [27] and is essentially determined by the number of integrated samples *N* and the number N_f of Doppler bins included in the range-Doppler map.

The results in Figure 27 are shown as a function of the CPI. As expected, the number of FLOPs required for ECA-S is higher than for ECA and ECA-B; this is indeed the price to be paid to obtain the observed performance improvement (see 3.4.5.B for this specific application). However, we observe that the increase in complexity is asymptotically constant and smaller than an order of magnitude.

Nevertheless, it is to be noted that the computational load required by ECA-S is much lower than that required for 2D-CCF evaluation for typical values of the CPI (i.e. CPI>1 s for this application) and the gap widens as the CPI increases. The Range-Doppler map computation is indeed a key step of the PCL signal processing. Therefore, the analysis above clearly shows that, despite the increased complexity with respect to previous ECA versions, the proposed ECA-S approach does not represent the bottleneck in the PCL signal processing chain.

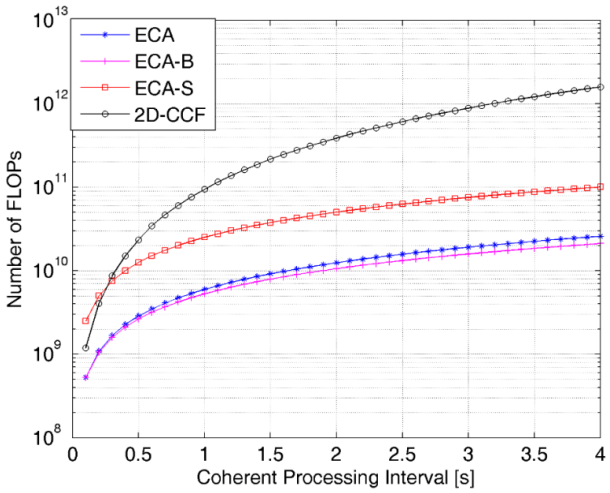

Figure 27 Number of FLOPs as a function of the CPI for the different ECA versions in comparison with the 2D-CCF evaluation in the case of DVB-T application.

As a last remark, from both Table 7 and Figure 27, we observe that the ECA and the ECA-B approaches largely benefit from the proposed efficient implementation. In this regard, the discussion reported in this section gains a more general value as the expedients introduced above can be fruitfully adopted to limit also the computational burden of the previous ECA versions. This makes these previous versions more appealing, at least for those applications that do not imply the limitations discussed in this paper.

Table 7 Number of FLOPs required for the efficient implementation of different ECA versions.

ECA Version	**Number of FLOPs**
ECA	$C_{ECA}(K,N) = 27.5N\log_2(N) + 16.5N + 16K^2$
ECA-B	$C_{ECA-B}(K,N_B) = B\,[27.5N_B\log_2(N_B) + 16.5N_B + 16K^2]$
ECA-S	$C_{ECA-S}(K,N_A,N_S) = B_S\,[17.5N_A\log_2(N_A) + 15N_S\log_2(N_S) + 16K^2 + 8.5N_A + 8N_S]$

3.4.7 CONCLUSIONS

In this section, a modified version of the ECA-Batches has been presented to cope with some limitations observed when dealing with highly varying disturbance characteristics in the presence slowly-moving targets or targets moving mainly along the cross-range direction. This ECA-Sliding approach operates on partially overlapped portions of the received signals so that it takes advantage of a smooth estimate of the filter coefficients.

The effectiveness of the proposed approach has been verified with reference to several live data sets accounting for very different PCL applications. The experimental results show that the ECA-S approach allows a better trade-off between disturbance cancellation and the capability to preserve low Doppler target echoes thus improving the detection performance of the resulting PCL system. Following the discussion on its efficient implementation, the proposed ECA-S can be regarded as an effective solution for practical PCL applications.

3.5 RANGE-DOPPLER MAP EVALUATION

3.5.1 PROBLEM STATEMENT

The evaluation of the (Range-Doppler Map) RDM represents one of the costliest operation of the passive radar processing chain in terms of computational burden. It consists in the calculus of the cross-correlation between the surveillance and the reference signals. The high cost required is due to the need of using long coherent processing intervals (CPIs) in order to obtain an acceptable SNR. In addition, large two dimensional maps might be required depending on the ratio between the surveillance region extent and the pixel spacing in both range and Doppler dimensions. Such aspect is even more emphasized with the increasing demand for an improved reliability of the PBR systems. This is achieved integrating the results processed by multiple receiving channels. In particular, signals collected at different frequencies, different polarizations or properly displaced antenna elements are processed at each coherent processing interval. The same task was performed on our passive system; indeed, up to three surveillance antennas were used. In addition, an experimental analysis on the performance of the system with multi-frequency integration was done. This means that the already onerous calculus of the RDM became the main bottle neck of the entire processing chain.

Many algorithms have been developed for the efficient evaluation of the theoretical RDM map. As it will be seen, existing optimum algorithms can be considered as loss-less approaches; however, time needed for RDM evaluation are prohibitively expensive for a real time application. This is especially true when wideband signals, such as DVB-T transmissions, are exploited. On the other hand, existing sub-optimum algorithms offer much lower computational load at the expense of SNR degradation; depending on the scenario, such losses may be so high as to compromise targets detection. For this reason it has been developed a sub-optimum algorithm able to overcome such limitations.

This section is organized as follows. In 3.5.2 and 3.5.3, existing optimum and sub-optimum algorithms will be presented and compared in terms of performance and computational load for a typical maritime scenario. The parameters characterizing the considered algorithms are accurately selected according to proper optimization criteria. The comparative analysis allows to identify the best suited sub-optimum technique for the considered application and, at the same time, to understand its main limitations. In section 0, the novel sub-optimum approach is presented; finally, the conclusions are drawn in 3.5.5.

3.5.2 STATE OF THE ART

The objective of the evaluation of the RDM is to look for potential targets that, due to the acquisition geometry, are characterized by some bistatic range and bistatic Doppler. For the purpose the reference signal is delayed and Doppler shifted in order to cover all the possible bistatic distances and velocities of the targets. Indeed, the evaluation of the RDM corresponds to the implementation of a bank of matched filters, each one tuned to a specific target bistatic velocity. Typically, those filters are chosen in order to cover all the possible target velocities. The filter where the target is detected provides an estimate of the bistatic Doppler shift; while the estimate of the bistatic range is given by the sample along range where it is detected.

The RDM is obtained by cross-correlating the surveillance signal with Doppler shifted replicas of the reference signal:

$$\chi[l,m] = \sum_{n=0}^{N-1} s_{surv}[n] \cdot s_{ref}^{*}[n-l] \cdot e^{-j2\pi\frac{mn}{N}} \tag{49}$$

where $N = \lfloor T_{int} f_s \rfloor$ is the number of samples in the CPI T_{int}, l $(l = 0, \dots, N_\tau - 1)$ represents the time bin corresponding to time delay $\tau = l/f_s$ and m $(m = -N_f/2, \dots, N_f/2 - 1)$ indicates the Doppler bin corresponding to Doppler shift $f_D = mf_s/N$, being f_s the sampling frequency.

As anticipated in the introduction of this section, evaluation of (49) represents one of the heaviest operation in the whole signal processing chain. In fact, the exploited waveform of opportunity is typically characterized by very low power level for radar purposes, so a very long integration time is needed to obtain an acceptable SNR. In addition large two dimensional maps may be required depending on the desired surveillance region extent in bot range $(0, R_{B\max})$ and Doppler dimensions $(\pm v_{B\max})$, where $R_{B\max}$ and $v_{B\max}$ are the maximum relative bistatic range and the maximum bistatic velocity of interest, respectively. The number of range and Doppler bins is given by:

$$N_\tau = \left\lceil \frac{R_{B\max}}{c} f_s \right\rceil \quad \text{and} \quad N_f = \left\lceil \frac{2|v_{B\max}|}{\lambda} \frac{N}{f_s} \right\rceil \tag{50}$$

thus direct evaluation of (49) over N_τ range bins and N_f Doppler bins would require $N(N_\tau + 1)N_f$ complex multiplications and $(N-1)N_\tau N_f$ complex additions.

In order to reduce the number of required operations, two alternative efficient implementations can be obtained by rearranging the factors in (49) according to different criteria and exploiting the well-known fast Fourier transform (FFT) algorithm to evaluate the discrete Fourier transform (DFT). For further details see [27].

Correlation-FFT

This implementation is based on the observation that, for a fixed Doppler bin m, the samples along of the RDM correspond to the samples of the cross-correlation between the reference signal and a Doppler shifted version of the surveillance signal $s_m[n] = s_{surv}[n] \cdot e^{-j2\pi mn/N}$:

$$\chi[l, m] = \sum_{n=0}^{N-1} s_m[n] \cdot s_{ref}^*[n-l] = C_m[l] \tag{51}$$

A computational load saving is obtained by evaluating the cross-correlation in the frequency domain as:

$$C_m[l] = \mathrm{IDFT}\{\ \ \mathrm{DFT}\{s_m[n]\}\,\mathrm{conj}\big(\mathrm{DFT}\{s_{ref}[n]\}\big)\ \ \} = \mathrm{IDFT}\{S_m[k]S_{ref}^*[k]\} \tag{52}$$

For each of the N_f Doppler filters, an IDFT is computed and $N - N_\tau$ samples are discarded. For a given Doppler filter, the DFT $S_m[k]$ of the sequence $s_m[n]$ can be obtained as a circular shift of the samples of $S_{surv}[k] = \mathrm{DFT}\{s_{surv}[n]\}$; in this way the DFT of the reference and surveillance signals can be evaluated just once and, for each Doppler bin, only N complex multiplications and a single IFFT must be performed. It is worth noticing that this algorithm can be parallelized over the Doppler dimension; its computational load is reported in Table 8.

Direct-FFT

This algorithm can be thought as the dual of the Correlation-FFT; it is based on the observation that, for each time bin l, the samples along Doppler frequency of the RDM correspond to the DFT of the sequence $x_l[n] = s_{surv}[n]s_{ref}^*[n-l]$ obtained as the product of the surveillance signal and the delayed conjugated reference:

$$\chi[l, m] = X_l[m] = \mathrm{DFT}\{x_l[n]\} \tag{53}$$

Similar to the previous algorithm, for each of the N_τ range bins, a DFT is evaluated and $N - N_\tau$ output samples are discarded; to reduce the required execution time a parallelization over the range dimension could be performed. The resulting computational load is reported in Table 8 for comparison. The sketches of both the algorithms is reported in Figure 28.

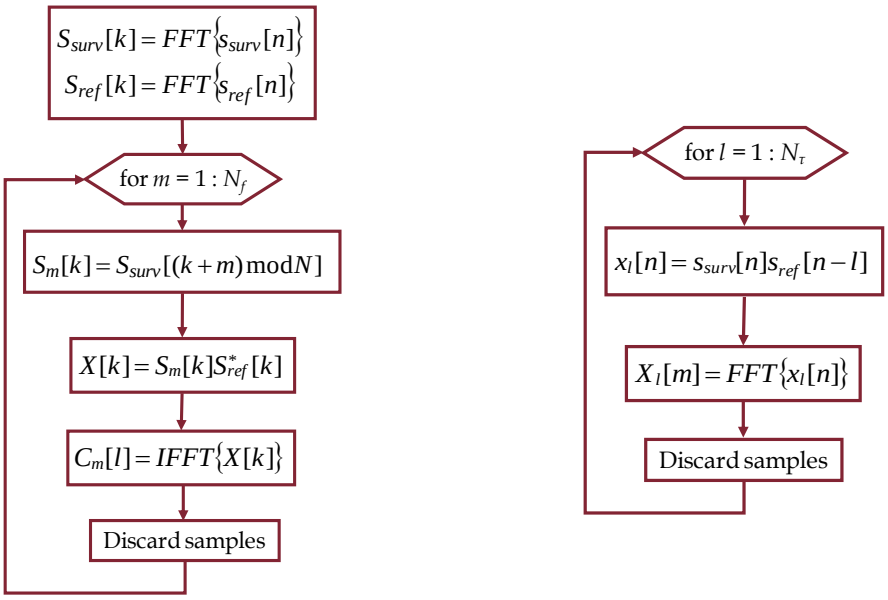

(a) (b)

Figure 28 Optimum efficient algorithms for RDM evaluation: (a) Correlation-FFT, (b) Direct-FFT.

Two existing sub-optimum algorithms will be now briefly described; they provide a remarkable computational load saving at the exchange of small SNR losses. Their sketches are reported in Figure 29, while the computational load is reported in Table 8.

Batches Algorithm

This sub-optimum algorithm is obtained by subdividing the CPI into n_B batches (sub-CPIs) of N_B samples each. The cross-correlation between the surveillance and reference signals is computed on a batch basis; the Doppler dimension is then synthesized by performing the FFT of the cross-correlation values taken at a given time delay. Specifically (49) is rewritten as:

$$\chi[l,m] = \sum_{r=0}^{n_B-1} e^{-j2\pi\frac{mr}{n_B}} \sum_{p=0}^{N_B-1} s_{surv}[rN_B+p]s^*_{ref}[rN_B+p-l]e^{-j2\pi\frac{mp}{N}} \tag{54}$$

and neglecting the complex exponential term within the inner summation we obtain

$$\chi[l,m] \cong \sum_{r=0}^{n_B-1} e^{-j2\pi\frac{mr}{n_B}} \sum_{p=0}^{N_B-1} s_{surv}[rN_B+p]s^*_{ref}[rN_B+p-l] = \sum_{r=0}^{n_B-1} e^{-j2\pi\frac{mr}{n_B}}\, y_l[r] \tag{55}$$

that represents the DFT of the decimated sequence $y_l[r]\ \ (r = 0, \dots, n_B - 1)$.

The number of batches n_B should be selected such that $n_B \geq N_f$. Within this limit, a smaller n_B provides a lower computational load but also yields a higher integration loss for fast-moving targets whose Doppler shift is not properly compensated. In fact, for a constant modulus signal the SNR loss for a target at range bin l and Doppler bin m can be written as:

$$L[l,m] = -20\log_{10}\left\{\frac{n_B}{N}\frac{\sin(\pi m/N_B)}{\sin(\pi m/N)}\right\} \tag{56}$$

that obviously depends just on the Doppler bin m. It reaches the maximum value at the highest Doppler of the RDM; in contrast, no loss is experienced at zero Doppler.

Channelization Technique

This algorithm operates by splitting the signals in the frequency domain into n_C sets of N_c samples, which are separately processed. This is achieved by calculating the FFT on $n_C = N/N_C$ samples and arranging them in n_C separate channels. Those are used to evaluate n_C Doppler profiles; delay dimension is then synthesized via IFFT of the values taken at a given Doppler bin. This algorithm represents a further approximation of the Batches Algorithm where the signals at each batch are cyclically extended before cross-correlation. In particular, we have:

$$\chi[l,m] \cong \sum_{r=0}^{N_c-1} e^{-j2\pi\frac{mr}{N_c}} \sum_{p=0}^{n_c-1} s_{surv}[rn_c+p]s_{ref}^{*}[rn_c+p-l] \cong$$
$$\cong \sum_{r=0}^{N_c-1} e^{-j2\pi\frac{mr}{N_c}} \left(\frac{1}{n_c} \sum_{k=0}^{n_c-1} S_{surv}^{(r)}[k] S_{ref}^{(r)*}[k] e^{+j2\pi\frac{kl}{n_c}} \right) = \frac{1}{n_c} \sum_{k=0}^{n_c-1} e^{+j2\pi\frac{kl}{n_c}} \sum_{r=0}^{N_c-1} Y[k,r] e^{-j2\pi\frac{mr}{N_c}} \quad (57)$$

As a result, additional SNR loss is experienced in the delay dimension. To limit such loss within the observed map, the reference signal fed in input to the algorithm is properly delayed so that the SNR loss is minimum at the central bin of the map (reference point) and symmetrically increases on both sides. With this expedient the algorithm parameters should be selected so that $N_\tau \leq n_C \leq N/N_f$. Reducing n_C within these limits allows a corresponding reduction in the computational load. In contrast, since the approximations used for this algorithm both affect the Doppler and the delay dimensions, the maximum SNR loss in the final map might not show a monotonic behavior with n_C.

Assuming a constant modulus signal, the SNR loss for a target located at delay bin l and Doppler bin m is given by:

$$L[l,m] = -20\log_{10}\left\{ \frac{1}{n_c} \frac{\sin(\pi m(n_c - (l - N_\tau/2))/N)}{\sin(\pi m/N)} \right\} \quad (58)$$

that reaches its maximum at the edges of the RDM.

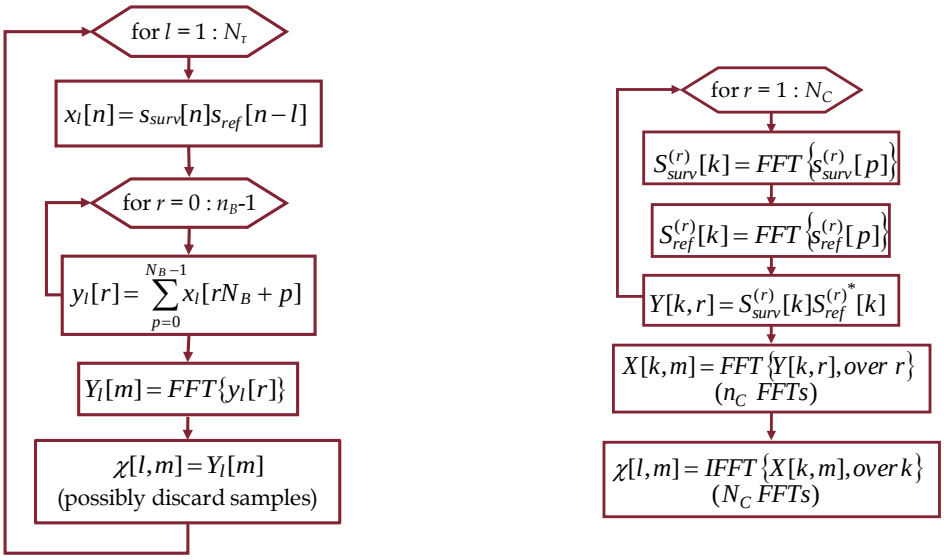

(a) (b)

Figure 29 Sub-optimum algorithms for RDM evaluation: (a) Batches algorithm, (b) Channelization technique.

In Figure 30 are reported typical courses of the SNR loss and computational load curves for the sub-optimum algorithms as a function of the characterizing parameters. Based on these example plots, the best parameter value is selecting according to the following criteria. For the Batches Algorithm, the parameter value is chosen within the region of n_B values where both the computational load and the SNR loss have a quite flat trend (i.e. they almost reached their minimum). Differently, for the Channelization Technique, one might observe that the SNR loss curve shows a minimum, while the computational load has a limited excursion within the edge of admitted values for n_C. Therefore, for this technique, the best parameter values appear to be the one that yields the lowest SNR loss.

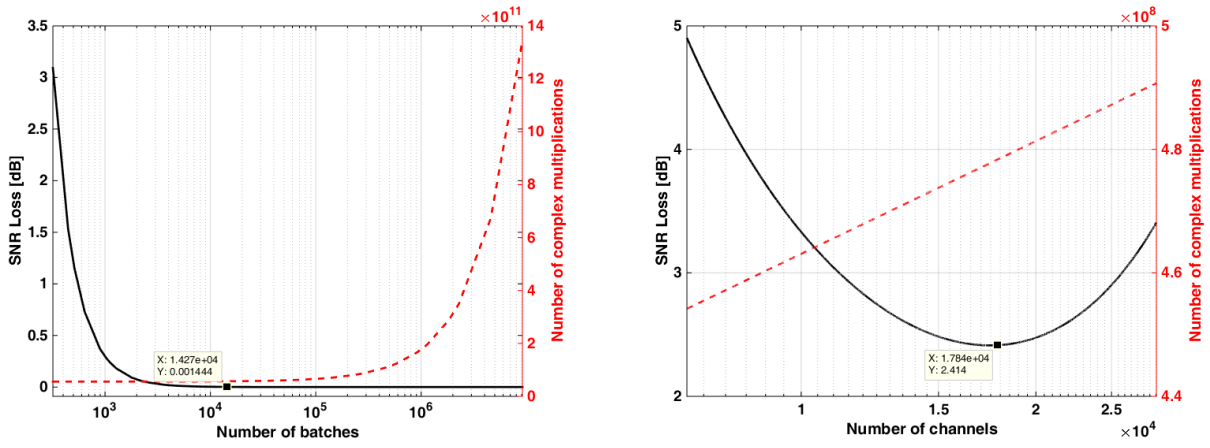

(a) (b)

Figure 30 SNR loss (solid black) and Computational load (dashed red) as a function of: (a) $\mathbf{n_B}$ for the Batches Algorithm, (b) $\mathbf{n_C}$ for the Channelization Technique.

In the next paragraph the conducted analysis will be presented; its objective was to identify the best suited algorithm for RDM evaluation.

3.5.3 COMPARATIVE STUDY OF EXISTING ALGORITHMS

A comparison among those algorithms in quite different practical scenarios for passive radar has been conducted. The analysis allowed to state the potentialities of the sub-optimum algorithms in reducing the computational load for the evaluation of the RDM; however, the quasi real-time operation could not be enabled as we could have two possibilities: (i) low SNR loss but still high computational load or (ii) remarkable computational load saving but high SNR loss. A much detailed analysis has been conducted for the maritime application and it will be reported in the following.

The computational load for the presented algorithm is reported in Table 8. The optimum algorithms obviously yield identical results and their computational load increase as $N \log_2 N$, however the final cost of the Correlation FFT is essentially determined by the number N_f of Doppler bins included in the map, while the cost of the Direct FFT is determined by the number N_τ of delay bins. As a consequence, when signals of opportunity with remarkable bandwidth are employed for long range surveillance applications, the Correlation FFT algorithm has to be preferred.

The operative scenarios in which the algorithms have been compared are now presented. In a maritime surveillance application, the low speed of the targets allows to use integration times of the order of up to 4 seconds without experiencing migration of the target return over contiguous cells of the map. For the computational load analysis, integration times equal to 1 and 4 seconds have been considered.

Table 8 Computational load for several RDM evaluation algorithms.

Algorithm	Complex multiplications	Complex additions
Correlation-FFT	$2N\log_2(N)+ N_f\,[N+N\log_2(N)]$	$2N\log_2(N)+N_f\,[N\log_2(N)]$
Direct-FFT	$N_\tau[N+N\log_2(N)]$	$N_\tau\,[N\log_2(N)]$
Batches Algorithm	$N_\tau\,[N+n_B\log_2(n_B)]$	$N_\tau\,[N+n_B\log_2(n_B)]$
Channelization Technique	$2N\log_2(n_C)+N+N\log_2(N)$	$2N\log_2(n_C)+N\log_2(N)$

The number of range bin N_τ is a function of the radar coverage; we considered medium (89 km) and long (200 km) range coverages. It is worth noticing that the former value has been chosen as it avoid the need of the RPR filter (described in 3.3).

The number N_f of Doppler bins is a function of the integration time T_{int} and of the wavelength of the emitted signal. For this reason, two DVB-T carrier frequencies, placed at the edge of the UHF band, have been considered: 474 and 858 MHz. In each scenario a maximum bistatic velocity equal to $\pm 40\ \mathrm{m/s}$ as been set.

Table 9 Considered operative scenarios for comparison of existing RDM evaluation algorithms.

Scenario		A	B	C	D	E	F	G	H
$\mathbf{T_{int}}$	[s]	1	1	1	1	4	4	4	4
$\mathbf{f_c}$	[MHz]	474	474	858	858	474	474	858	858
$\mathbf{R_{Bmax}}$	[km]	89	200	89	200	89	200	89	200
$\mathbf{N_\tau}$		2714	6097	2714	6097	2714	6097	2714	6097
$\mathbf{N_f}$		258	258	462	462	1014	1014	1834	1834

The computational load for each of the presented algorithm will be shown in the following. In addition, for the sub-optimum algorithms, the values of SNR loss will be provided.

In Table 10 and Table 11 the number of complex multiplications for the evaluation of the RDM is reported for the optimum algorithms as a function of the scenario and of the kind of DVB-T signal. Those reported in red represent the more demanding scenarios for the examined technique.

Table 10 Number of complex multiplications for the RDM evaluation via Correlation-FFT.

Correlation FFT	**A**	**B**	**C**	**D**	**E**	**F**	**G**	**H**
Mode 2k, Guard 1/4	$2{,}88\cdot10^{10}$	$2{,}88\cdot10^{10}$	$5{,}13\cdot10^{10}$	$5{,}13\cdot10^{10}$	$4{,}86\cdot10^{11}$	$4{,}86\cdot10^{11}$	$8{,}77\cdot10^{11}$	$8{,}77\cdot10^{11}$
Mode 2k, Guard 1/8	$2{,}88\cdot10^{10}$	$2{,}88\cdot10^{10}$	$5{,}13\cdot10^{10}$	$5{,}13\cdot10^{10}$	$4{,}86\cdot10^{11}$	$4{,}86\cdot10^{11}$	$8{,}77\cdot10^{11}$	$8{,}77\cdot10^{11}$
Mode 2k, Guard 1/16	$2{,}88\cdot10^{10}$	$2{,}88\cdot10^{10}$	$5{,}13\cdot10^{10}$	$5{,}13\cdot10^{10}$	$4{,}86\cdot10^{11}$	$4{,}86\cdot10^{11}$	$8{,}77\cdot10^{11}$	$8{,}77\cdot10^{11}$
Mode 2k, Guard 1/32	$2{,}88\cdot10^{10}$	$2{,}88\cdot10^{10}$	$5{,}13\cdot10^{10}$	$5{,}13\cdot10^{10}$	$4{,}86\cdot10^{11}$	$4{,}86\cdot10^{11}$	$8{,}77\cdot10^{11}$	$8{,}77\cdot10^{11}$
Mode 8k, Guard 1/4	$2{,}88\cdot10^{10}$	$2{,}88\cdot10^{10}$	$5{,}13\cdot10^{10}$	$5{,}13\cdot10^{10}$	$4{,}85\cdot10^{11}$	$4{,}85\cdot10^{11}$	$8{,}77\cdot10^{11}$	$8{,}77\cdot10^{11}$
Mode 8k, Guard 1/8	$2{,}88\cdot10^{10}$	$2{,}88\cdot10^{10}$	$5{,}13\cdot10^{10}$	$5{,}13\cdot10^{10}$	$4{,}86\cdot10^{11}$	$4{,}86\cdot10^{11}$	$8{,}77\cdot10^{11}$	$8{,}77\cdot10^{11}$
Mode 8k, Guard 1/16	$2{,}88\cdot10^{10}$	$2{,}88\cdot10^{10}$	$5{,}12\cdot10^{10}$	$5{,}12\cdot10^{10}$	$4{,}86\cdot10^{11}$	$4{,}86\cdot10^{11}$	$8{,}77\cdot10^{11}$	$8{,}77\cdot10^{11}$
Mode 8k, Guard 1/32	$2{,}88\cdot10^{10}$	$2{,}88\cdot10^{10}$	$5{,}12\cdot10^{10}$	$5{,}12\cdot10^{10}$	$4{,}86\cdot10^{11}$	$4{,}86\cdot10^{11}$	$8{,}77\cdot10^{11}$	$8{,}77\cdot10^{11}$

Table 11 Number of complex multiplications for the RDM evaluation via Direct-FFT.

Direct FFT	A	B	C	D	E	F	G	H
Mode 2k, Guard 1/4	$5{,}97 \cdot 10^{11}$	$1{,}34 \cdot 10^{12}$	$5{,}97 \cdot 10^{11}$	$1{,}34 \cdot 10^{12}$	$2{,}59 \cdot 10^{12}$	$5{,}82 \cdot 10^{12}$	$2{,}59 \cdot 10^{12}$	$5{,}82 \cdot 10^{12}$
Mode 2k, Guard 1/8	$5{,}98 \cdot 10^{11}$	$1{,}34 \cdot 10^{12}$	$5{,}98 \cdot 10^{11}$	$1{,}34 \cdot 10^{12}$	$2{,}59 \cdot 10^{12}$	$5{,}82 \cdot 10^{12}$	$2{,}59 \cdot 10^{12}$	$5{,}82 \cdot 10^{12}$
Mode 2k, Guard 1/16	$5{,}98 \cdot 10^{11}$	$1{,}34 \cdot 10^{12}$	$5{,}98 \cdot 10^{11}$	$1{,}34 \cdot 10^{12}$	$2{,}59 \cdot 10^{12}$	$5{,}82 \cdot 10^{12}$	$2{,}59 \cdot 10^{12}$	$5{,}82 \cdot 10^{12}$
Mode 2k, Guard 1/32	$5{,}98 \cdot 10^{11}$	$1{,}34 \cdot 10^{12}$	$5{,}98 \cdot 10^{11}$	$1{,}34 \cdot 10^{12}$	$2{,}59 \cdot 10^{12}$	$5{,}82 \cdot 10^{12}$	$2{,}59 \cdot 10^{12}$	$5{,}82 \cdot 10^{12}$
Mode 8k, Guard 1/4	$5{,}97 \cdot 10^{11}$	$1{,}34 \cdot 10^{12}$	$5{,}97 \cdot 10^{11}$	$1{,}34 \cdot 10^{12}$	$2{,}59 \cdot 10^{12}$	$5{,}82 \cdot 10^{12}$	$2{,}59 \cdot 10^{12}$	$5{,}82 \cdot 10^{12}$
Mode 8k, Guard 1/8	$5{,}98 \cdot 10^{11}$	$1{,}34 \cdot 10^{12}$	$5{,}98 \cdot 10^{11}$	$1{,}34 \cdot 10^{12}$	$2{,}59 \cdot 10^{12}$	$5{,}82 \cdot 10^{12}$	$2{,}59 \cdot 10^{12}$	$5{,}82 \cdot 10^{12}$
Mode 8k, Guard 1/16	$5{,}97 \cdot 10^{11}$	$1{,}34 \cdot 10^{12}$	$5{,}97 \cdot 10^{11}$	$1{,}34 \cdot 10^{12}$	$2{,}59 \cdot 10^{12}$	$5{,}82 \cdot 10^{12}$	$2{,}59 \cdot 10^{12}$	$5{,}82 \cdot 10^{12}$
Mode 8k, Guard 1/32	$5{,}97 \cdot 10^{11}$	$1{,}34 \cdot 10^{12}$	$5{,}97 \cdot 10^{11}$	$1{,}34 \cdot 10^{12}$	$2{,}59 \cdot 10^{12}$	$5{,}82 \cdot 10^{12}$	$2{,}59 \cdot 10^{12}$	$5{,}82 \cdot 10^{12}$

As the number of range bins is much greater than the number of Doppler bins in each scenario, Direct-FFT is always characterized by a higher computational load. As can be seen from the related table, a greater number of operations is required when, for a fixed integration time, a higher coverage is sought.

Regarding the Correlation-FFT, the worst cases are those characterized by a higher number of Doppler bins. This result can be expected as the algorithm scans all the Doppler bins and evaluates, in the frequency domain, the cross-correlation between the reference signal and the Doppler shifted version of the surveillance signal.

The transmission mode and the size of the guard interval have a low impact on the computational load; small differences are due to small adjustments made on the number of integrated samples. For this reason, in the following the analysis on the computational load will be performed for one of the mostly used DVB-T signal format which is the 8k with guard interval equal to 1/4.

The computational load of sub-optimum algorithms, as well as the loss introduced by them, is a function of their characterizing parameters n_B and n_C. In Table 12 and Table 13 is reported the computational load together with the maximum SNR loss within the RDM and the selected parameter value for the two sub-optimum algorithms. Those reported in the tables refer to the choices of the parameters that minimize the SNR loss in each scenario.

Table 12 Computational load, SNR loss and parameter selection for the Batches algorithm.

Batches Algorithm	A	B	C	D	E	F	G	H
Computational load	$2{,}62 \cdot 10^{10}$	$5{,}89 \cdot 10^{10}$	$2{,}62 \cdot 10^{10}$	$5{,}72 \cdot 10^{10}$	$1{,}04 \cdot 10^{11}$	$2{,}30 \cdot 10^{11}$	$1{,}04 \cdot 10^{11}$	$2{,}30 \cdot 10^{11}$
SNR Loss[dB]	$4{,}50 \cdot 10^{-5}$	$4{,}67 \cdot 10^{-5}$	$1{,}49 \cdot 10^{-4}$	$5{,}98 \cdot 10^{-4}$	$7{,}04 \cdot 10^{-5}$	$1{,}36 \cdot 10^{-4}$	$2{,}30 \cdot 10^{-4}$	$4{,}45 \cdot 10^{-4}$
Parameter selection n_B	35680	35680	35680	17840	114176	81920	114176	81920

Table 13 Computational load, SNR loss and parameter selection for the Channelization technique.

Channelization Technique	A	B	C	D	E	F	G	H
Computational load	$4{,}82 \cdot 10^{8}$	$4{,}90 \cdot 10^{8}$	$4{,}72 \cdot 10^{8}$	$4{,}82 \cdot 10^{8}$	$2{,}00 \cdot 10^{9}$	$2{,}03 \cdot 10^{9}$	$1{,}96 \cdot 10^{9}$	$2{,}00 \cdot 10^{9}$
SNR Loss[dB]	0,85	1,45	1,25	2,1	0,84	1,43	1,24	2,09
Parameter selection n_C	20480	28544	14272	20480	20480	28544	14272	20480
Correlation-FFT (N'<N)	$2{,}34 \cdot 10^{10}$	$2{,}02 \cdot 10^{10}$	$3{,}78 \cdot 10^{10}$	$3{,}06 \cdot 10^{10}$	$3{,}95 \cdot 10^{11}$	$3{,}42 \cdot 10^{11}$	$6{,}47 \cdot 10^{11}$	$5{,}27 \cdot 10^{11}$

As can be seen the Batches Algorithm provides only a limited computational load reduction at the expenses of very small SNR losses (fractions of dB). A remarkable saving can be obtained recurring to Channelization Technique; however, the SNR losses are much higher with respect to the Batches Algorithm and increase with the dimension of the map. Obviously, SNR losses introduced by Channelization Technique may be detrimental in practical situations; nevertheless, to show the high potentialities in computational load saving, we also reported the computational load of the most efficient optimum algorithm (Correlation-FFT) using $N' < N$ integrated samples, where N' has been chosen so that the integration gain is reduced of a factor equal to SNR loss introduced by the sub-optimum algorithm.

In this regard it is worth noticing that the SNR losses reported in Table 13 are the maximum loss experienced in the map: the loss for a target lying in a generic point of the map may be much smaller (punctual SNR loss of the sub-optimum algorithm is reported in Figure 31).

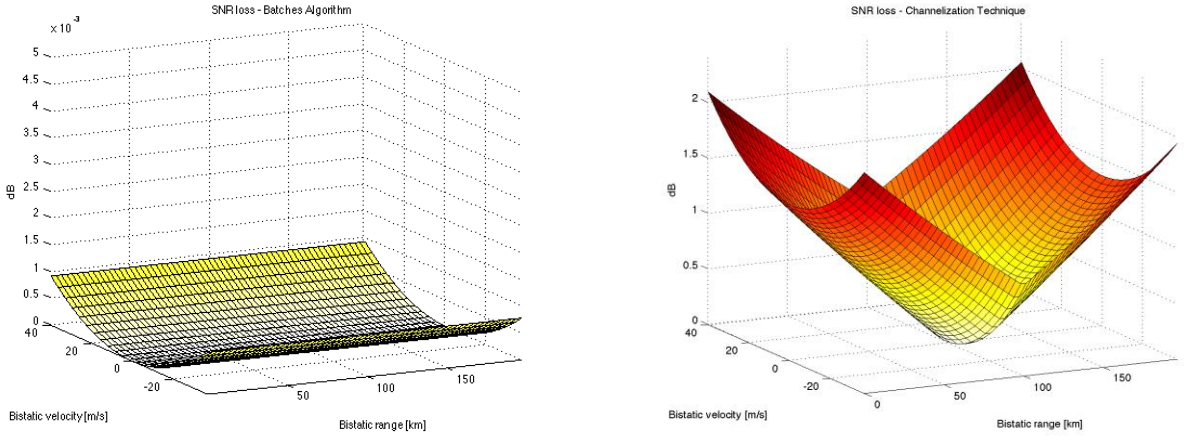

(a) (b)

Figure 31 SNR loss over the RDM map in scenario 'H' for: (a) Batches Algorithm (b) Channelization Technique.

Moreover, the computational load of the optimum algorithm with reduced integration gain (all over the map) is still higher that the computational load of the channelization technique and this clearly proves the efficiency of the algorithm. However, the main limitation of this approach is represented by the impossibility to further reduce the expected loss by acting on the characterizing parameter. Therefore, in the next paragraph a novel sub-optimum approach is presented, able to overcome this limitation.

3.5.4 BLOCK BASED CHANNELIZATION TECHNIQUE

As can be noted in Figure 31(b), the maximum SNR loss provided by Channelization Technique occurs at the edge of the map and is a function of the map delay and Doppler extents. Therefore, an effective way to reduce such loss is to partition the desired map into adjacent sub-maps (blocks) of reduced dimensions and to apply the Channelization Technique to each block. The sub-maps are then recombined to obtain the final map (see Figure 32(a)). This technique has been named Block based Channelization Technique (BBCT).

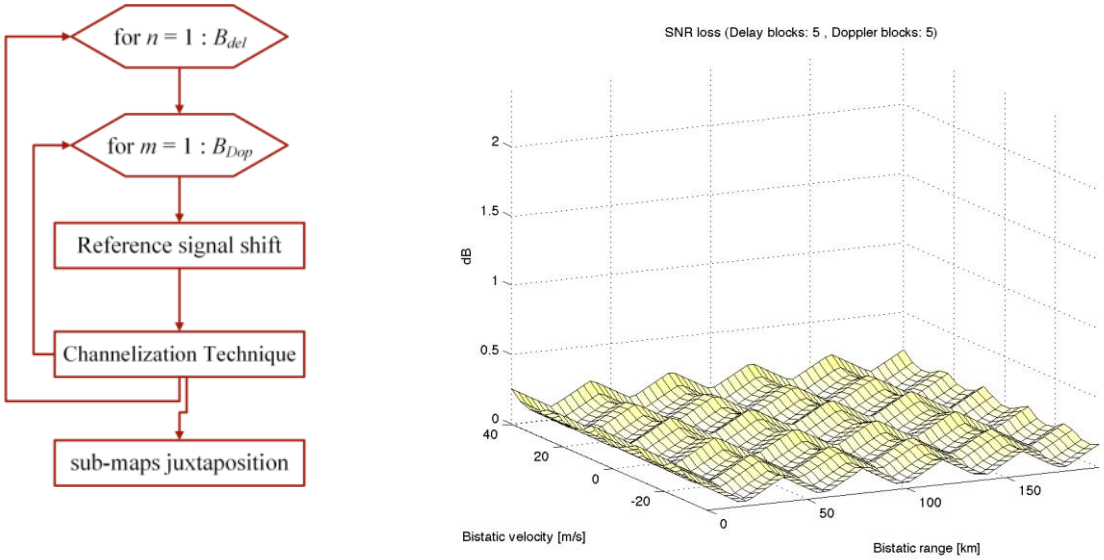

(a) (b)

Figure 32 (a) Block diagram of the Block based Channelization Technique, (b) Scenario 'H' - Punctual SNR loss using two blocks in the range dimension.

The computational load of this technique is almost directly proportional to the number of blocks used. As an example in Table 14, it is reported the number of complex products and the SNR loss for the 'H'-Scenario using several blocks in the range and Doppler dimension. The actual loss over the RDM when using 5 blocks in both delay and Doppler is depicted in Figure 32(b); the maximum loss is still experienced at the edges of each block, however it can be noted its lower value with respect to the RDM obtained with the conventional Channelization Technique in Figure 31(b).

Table 14 SNR loss and, in brackets, computational load applying BBCT for RDM evaluation in Scenario 'H'.

		Delay blocks				
		1	2	3	4	5
Doppler blocks	1	2,09 (2,00 · 10^9)	1,35 (3,93 · 10^9)	1,04 (5,89 · 10^9)	0,87 (7,71 · 10^9)	0,11 (9,64 · 10^9)
	2	1,35 (4,07 · 10^9)	0,87 (8,00 · 10^9)	0,66 (1,20 · 10^{10})	0,54 (1,59 · 10^{10})	0,47 (1,99 · 10^{10})
	3	1,04 (6,22 · 10^9)	0,66 (1,23 · 10^{10})	0,51 (1,83 · 10^{10})	0,43 (2,40 · 10^{10})	0,36 (3,00 · 10^{10})
	4	0,88 (8,30 · 10^9)	0,55 (1,65 · 10^{10})	0,42 (2,46 · 10^{10})	0,34 (3,26 · 10^{10})	0,30 (4,07 · 10^{10})
	5	0,74 (1,05 · 10^{10})	0,47 (2,07 · 10^{10})	0,36 (3,09 · 10^{10})	0,30 (4,10 · 10^{10})	0,26 (5,13 · 10^{10})

Recurring to 5 delay and Doppler blocks the SNR loss provided by the algorithm is largely more acceptable with respect to the one provided by Channelization Technique and computational load reduction is still important compared to other algorithms, as can be seen in Table 15.

Table 15 Computational load comparison.

Algorithm	**Complex products**
BBCT ($B_{del} = 5, B_{dop} = 5$)	$5{,}13 \cdot 10^{10}$
Batches Algorithm	$2{,}30 \cdot 10^{11}$
Correlation FFT ($N' < N$)	$8{,}23 \cdot 10^{11}$

3.5.4.1 ADDITIONAL CONSIDERATIONS ON THE CHOICE OF THE BBCT PARAMETER

In the following some additional considerations on the choice of the parameter n_C are provided. They apply for both the conventional Channelization Technique and the Block based Channelization Technique. It has been found that whether the value of n_C leading to the minimum SNR loss is equal to the number N_s of samples contained in an OFDM symbol, an undesired peak appears in the RDM. This will be shown against simulated data.

Simulated signals are generated as follows. First of all, the reference signal is generated and its first sample coincides with the beginning of the first OFDM symbol. In order to emulate a target, the reference signal is properly delayed and Doppler shifted thus obtaining the surveillance signal. Simulated target is assumed to be at zero range and zero Doppler; this means that also the beginning of the surveillance signal is aligned with the beginning of the OFDM symbol.

Two different signals have been simulated: an 8k mode with 1/4 guard interval and an 8k mode with 1/8 guard interval. Figure 33(a)-(d) show the RDM for those signals both not applying (figures (a) and (c)) and applying ((b) and (d)) the SLL technique for sidelobe control. In all the cases the RDM have been evaluated by means of the Channelization technique with $n_C = N_s$. As is apparent, a strong peak appears in all the maps at a delay corresponding to the guard interval $\left(\frac{1}{G+1}T_s\right)$, where G represents the proportional factor between the useful and the guard part of the OFDM symbol.

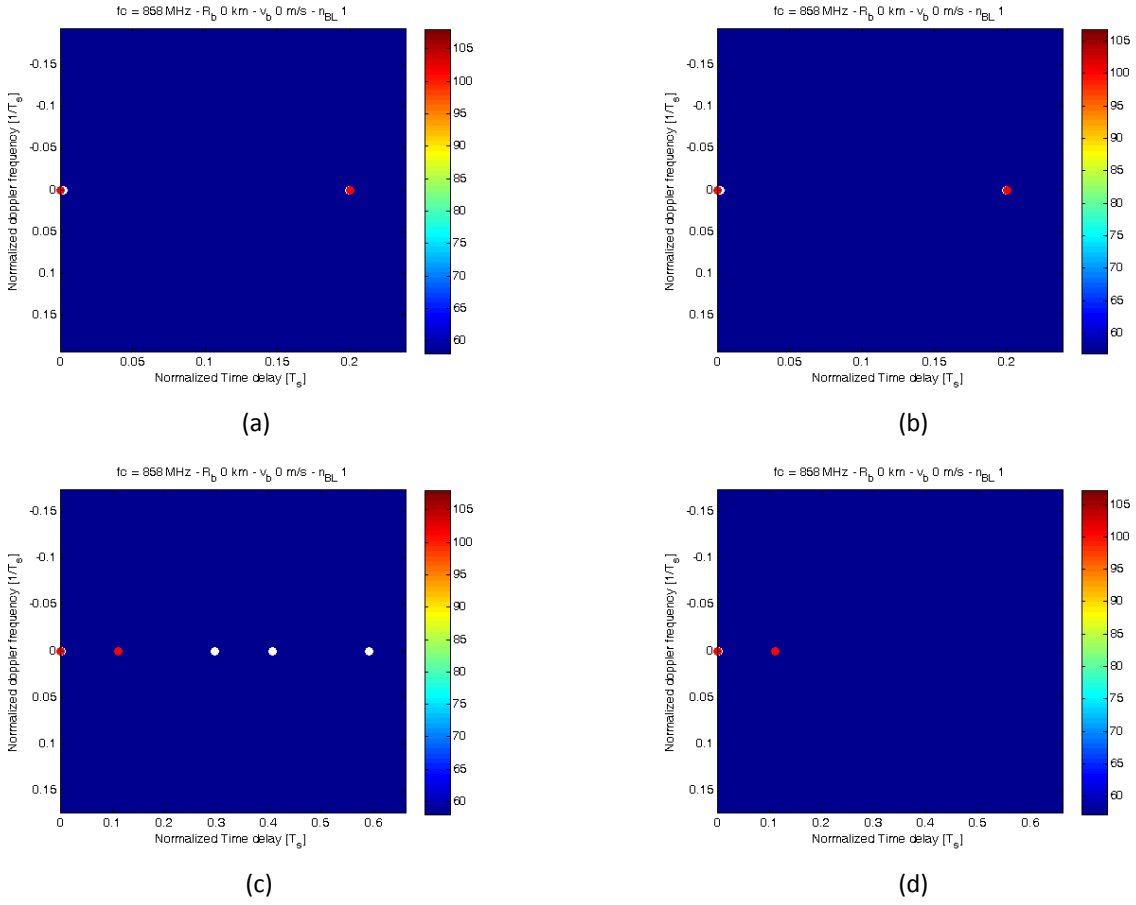

Figure 33 RDM ($\boldsymbol{n_c = N_s}$) obtained not applying and applying SLL technique for simulated DVB-T signals: (a) 8k 1/4 - without SLL, (b) 8k 1/4 - with SLL, (c) 8k 1/8 - without SLL, (d) 8k 1/4 - with SLL.

The phenomenon is due to the perfect correlation of the guard interval samples of the reference signal with those of the surveillance one; this is depicted in Figure 34. Such perfect correlation produces an undesired peak at a level from the peak equal to $\mathrm{dB}(N_g/N_s)$, where N_g is the number of samples in the guard interval.

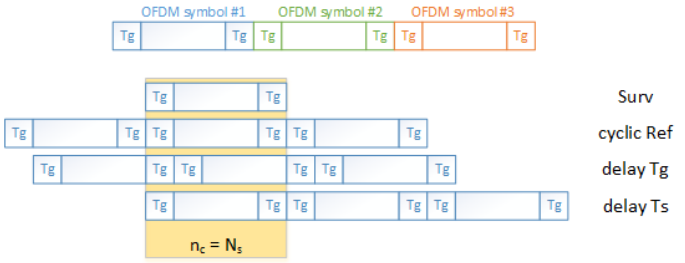

Figure 34 Example of cyclic correlation for $\boldsymbol{n_c = N_s}$.

Evaluating the RDM using $n_C = 2 \cdot N_s$ the correlation happens with the periodicity depicted in Figure 35 and provides two undesired peaks at $T_s \pm T_g$. RDM for a 2k mode and 1/4 guard interval is represented in Figure 36.

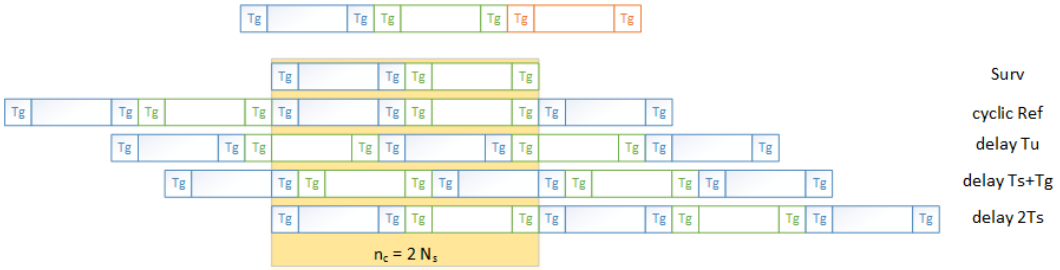

Figure 35 Example of cyclic correlation for $\boldsymbol{n_c = 2 \cdot N_s}$.

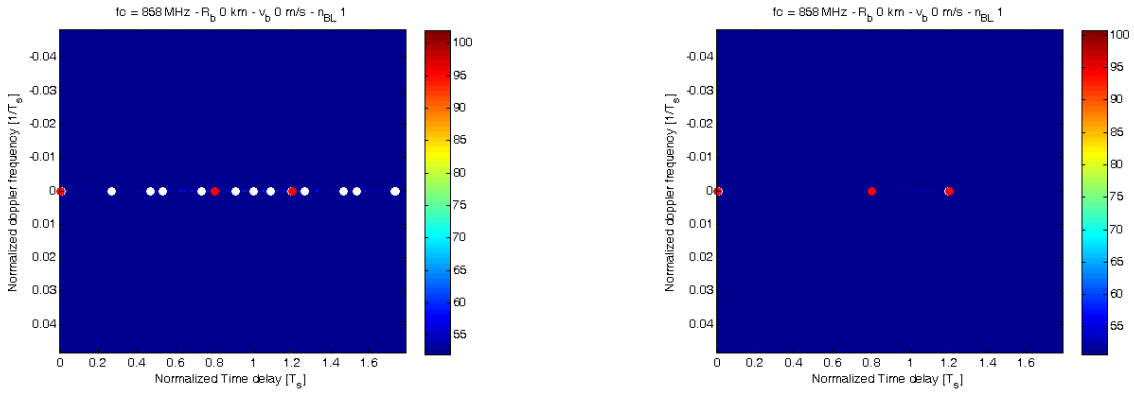

(a) (b)

Figure 36 RDM ($\boldsymbol{n_c = 2 \cdot N_s}$) obtained not applying and applying SLL technique for a 2k mode simulated DVB-T signal with guard interval equal to 1/4.

In Table 16 an analysis on the Peak to Sidelobe Level Ratio (PSLR) is reported for several DVB-T signals. As can be seen there is a very good agreement between the expected and the actual PSLR.

Table 16 Actual PSLR for several guard interval sizes.

DVB-T signal type	Map Extension R_{Bmax} , v_{Bmax}	Main Peak [dB]	Expected PSLR [dB]	Actual PSLR [dB]
8k 1/4 - $n_c = N_s$	70 km , 60 m/s	108.06	13.98	13.97
8k 1/8 - $n_c = N_s$	70 km , 60 m/s	108.05	19.09	19.12
8k 1/16 - $n_c = N_s$	70 km , 60 m/s	108.05	24.61	24.57
8k 1/32 - $n_c = N_s$	70 km , 60 m/s	108.06	30.37	30.41

It is worth noticing that the level of the undesired peak shown in the table is the worst case ever possible; in fact a perfect synchronism has been assumed between (i) the surveillance and the reference signal, and (ii) the beginning of the OFDM symbol and the beginning of the channels in which the signals are split for RDM evaluation. Generally the PSLR will be lower due to the likely lack of synchronism between signals that involves a smaller number of perfectly correlating guard samples. For example, delaying the reference signal in order to experience the minimum SNR loss provided by the Channelization Technique at the center of the RDM, one obtains PSLR = 23.37 dB for the 8k 1/4 DVB-T signal (instead of 13.97 dB) as reported in Figure 37(a). A graphical explanation of the result is shown in Figure 37(b).

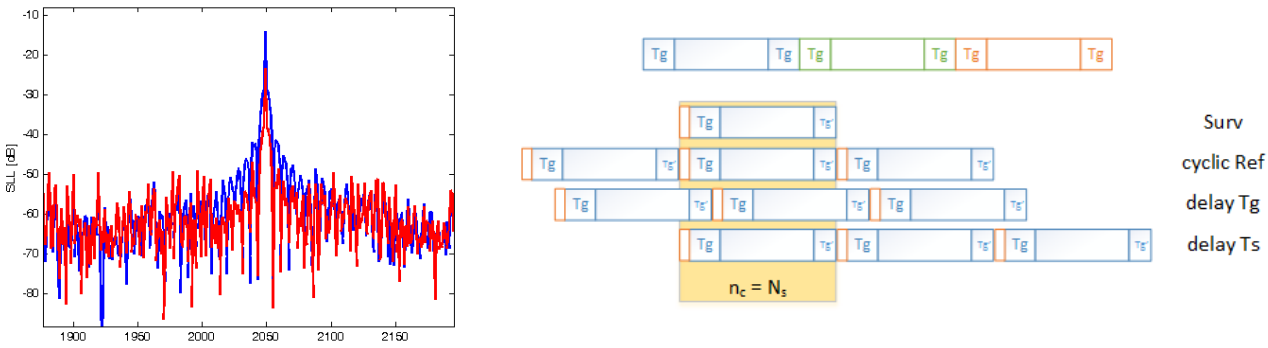

(a) (b)

Figure 37 (a) PSLR for two different synchronisms of the signals. (b) Example of cyclic correlation for $\boldsymbol{n_c = N_s}$ in case of non-perfect synchronism between portions of reference and surveillance signals and the beginning of OFDM symbols.

To avoid the appearance of such peak inside the RDM, a proper constraint for the choice of the parameter n_C has been set. In particular, it is chosen in order to have the undesired peak at a bistatic range greater than the maximum observable one. The relationship to be fulfilled is

$$(n_s - 1) \cdot T_s + T_g > \frac{\Delta R_{Bmax}}{c} \tag{59}$$

where n_s represents the number of OFDM symbols contained in n_C. It follows that:

$$n_s > \left(\frac{\Delta R_{Bmax}}{cT_u} G - 1\right) \cdot \frac{1}{G+1} + 1 \tag{60}$$

Thus the minimum value of n_C is the one that satisfies $n_{Cmin} > n_s \cdot N_s$ where, we recall, N_s is the number of samples contained in an OFDM symbol.

In the following an analysis over two different scenarios is conducted, with the objective of comparing the optimum choice of n_C (thus the one carrying the lowest SNR loss) with the lower bound provided by the constraint in the equation above.

Considered scenarios are:

- Scenario 1: $R_{Bmax} = 80\ km$, $v_{Bmax} = \pm 60\ m/s$
- Scenario 2: $R_{Bmax} = 220\ km$, $v_{Bmax} = \pm 60\ m/s$

Table 17 and Table 18 report, for each guard interval size, the number N_S of samples contained in each OFDM symbol. The second and third rows contain the values n_{c1} that provide the lowest L_1 SNR loss in the RDM. The value n_{c1} has to be compared with the one ($n_{c_{min}}$) that satisfies the constraint for the absence of the undesired peak. Whether the constraint is not fulfilled a new parameter, n_{c2}, that both meets the constraint and minimizes the loss is chosen. Provided loss is indicated with L_2. Cases requiring a novel optimization are highlighted in red.

Table 17 DVB-T signal (8k mode) - Scenario 1.

Guard Interval	**1/4**	**1/8**	**1/16**	**1/32**
N_s	10240	9216	8704	8448
n_{c1} (min loss)	10240	11280	10624	11264
L_1 [dB]	1.52	1.51	1.51	1.52
$n_{c_{min}}$	>10632	>10632	>10632	>10632
n_{c2}	13568		11288	
L_2 [dB]	1.61		1.51	

Table 18 DVB-T signal (8k mode) - Scenario 2.

Guard Interval	**1/4**	**1/8**	**1/16**	**1/32**
N_s	10240	9216	8704	8448
n_{c1} (min loss)	16384	15360	15936	16448
L_1 [dB]	2.71	2.70	2.70	2.72
$n_{c_{min}}$	>14292	>14292	>14292	>14292

Regarding the case of 1/4 guard interval in Table 17, the SNR loss to be accepted using the parameter n_{c2} is slightly higher ($+0{,}09$ dB) of the one yielded by n_{c1} however it has the nice advantage of not being affected by the undesired peak due to the perfect correlation of the guard samples. RDMs obtained applying the Channelization Technique with $n_c = n_{c2}$ are reported in Figure 38; the comparison with those of Figure 33 allow to state the effectiveness of the applied constraint.

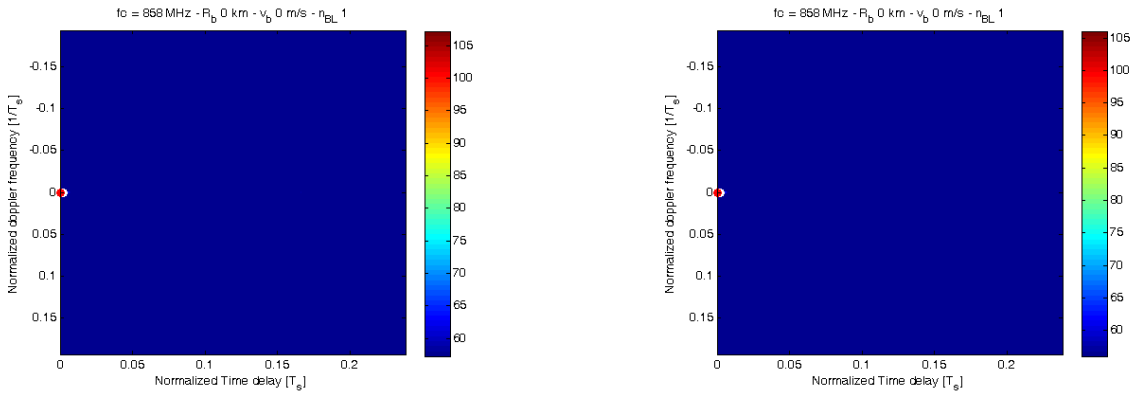

(a) (b)

Figure 38 RDM ($\boldsymbol{n_c = 13568}$) obtained not applying and applying SLL technique for simulated DVB-T signals: (a) 8k 1/4 - without SLL, (b) 8k 1/4 - with SLL

Similar analysis has been conducted for the 2k mode DVB-T signal; the results are summarized in Table 19 and Table 20 for the two considered scenarios. The constraint on n_c is always satisfied so no re-optimization is required.

Table 19 DVB-T signal (2k mode) - Scenario 1.

Guard Interval	**1/4**	**1/8**	**1/16**	**1/32**
N_s	2560	2304	2176	2112
n_{c1} (min loss)	10240	11304	8704	11264
L_1 [dB]	1.52	1.52	1.60	1.52
$n_{c_{min}}$	>4488	>4488	>4488	>4488

Table 20 DVB-T signal (2k mode) - Scenario 2.

Guard Interval	**1/4**	**1/8**	**1/16**	**1/32**
N_s	2560	2304	2176	2112
n_{c1} (min loss)	16384	15072	15952	16448
L_1 [dB]	2.72	2.71	2.70	2.72
$n_{c_{min}}$	>8148	>8148	>8148	>8148

For both the transmission modes, the RDM evaluation via Channelization Technique always yields a maximum SNR loss greater than 2 dB in the second scenario. To reduce such loss, the Block based Channelization Technique could be exploited. With the objective of lowering the loss below 2 dB, the required number of blocks for each transmission mode and guard interval size is reported in Table 21-Table 22. As can be seen two blocks are sufficient to achieve the objective.

Table 21 DVB-T signal (8k mode) - Scenario 2.

Guard Interval	**1/4**	**1/8**	**1/16**	**1/32**
N_{blocks}	2	2	2	2
n_{c1} (min loss)	13568	12032	11288	12336
L_1 [dB]	1.79	1.74	1.75	1.75
$n_{c_{min}}$	>9717	>9717	>9717	>9717

Table 22 DVB-T signal (2k mode) - Scenario 2.

Guard Interval	**1/4**	**1/8**	**1/16**	**1/32**
N_{blocks}	2	2	2	2
n_{c1} (min loss)	13568	11304	8704	12336
L_1 [dB]	1.79	1.75	1.93	1.75
$n_{c_{min}}$	>3573	>3573	>3573	>3573

3.5.5 CONCLUSIONS

In this section we introduced a low-cost sub-optimum algorithm for the evaluation of the 2D- CCF exploited by passive radar. The proposed approach operates by applying an efficient sub-optimum technique on adjacent blocks of the original Delay-Doppler map. A comparison with existing optimum and alternative sub-optimum algorithms has been performed against typical scenarios. The proposed technique is proven to offer a better control of the SNR loss to be accepted that can be more flexibly traded with the computational load. Even in the demanding case of an aerial surveillance application based on DVB-T transmissions, a few blocks are required in both delay and Doppler dimensions to limit the expected loss well below 1 dB while retaining a significant computational load saving with respect to alternative approaches. Notice that the residual loss can be partly recovered by the increased update rate allowed by the reduced computational burden. In this regard, it is also important to notice that the proposed Block based Channelization technique is intrinsically well suited for a parallel computing or it allow to apply the Channelization Technique even when the Delay-Doppler extension would not allow it.

3.6 TARGET DOA ESTIMATION

3.6.1 INTRODUCTION

As the DVB-T based PBR exploits up to three surveillance antennas dislocated along the horizontal dimension, target direction of arrival (DoA) could be provided for localization in the Cartesian plane. Typically, an array designed for DoA estimation is dimensioned so as to offer an unambiguous angular sector comparable with the antenna beamwidth since it is assumed that targets outside of it are not detected. However, it may not be true for every application such as simultaneous short and long range coastal surveillance where close targets are detected even through the sidelobes of the receiving antennas.

The request for a wide unambiguous angular sector would require an array of reduced size, however this would result in a poor estimation accuracy, accentuated by the use of low frequencies [58]. To improve the accuracy, it would be necessary to increase the size of the array which, in turn, introduces ambiguities problems that are extensively discussed in the literature. In our case, ambiguity problems are emphasized by the reduced number of receiving elements that, to keep costs of the system down, is generally a prerogative of PBR systems.

Several approaches of target estimation are described in literature, among them the ML estimator is one of the most known. However, such estimator is only asymptotically efficient, i.e. it reaches the Cramer-Rao bound at high SNR, while it is affected by a threshold effect when SNR is low. This may by a strong limitation as passive radars typically work with low levels of SNR; thus it would be useful to introduce bounds that are able to consider (i) the obtainable accuracy given the array geometry and (ii) the possible presence of ambiguities.

Our goal is to find an approach able to relax the trade-off on the distance between the elements. On the basis of our study the best positioning for the elements of the array is found and this will constitute an input for the design of the receiving antenna. In fact the acquisition will be performed with the array as it has been dimensioned.

This section is structured as follows. In 3.6.2, we describe the data model and the relative ML estimator is derived. As it will be seen, performance of an ML estimator highly depends on the position of the elements of the receiving array thus a proper positioning should be performed. The analytic functional, described in [59], able to predict performance of the ML estimator at low SNR is briefly presented in 3.6.3 and the design strategy based on it is described right after. An efficient estimation technique that, unlike ML estimator, does not require any process for maximum research while providing similar performance is presented in 3.6.4 and its performance is compared to the one of the ML estimator even in the case of an unbalanced array in 3.6.6. Finally results from the acquisition campaigns are shown in 3.6.7 prior to derive conclusions in 3.6.8.

3.6.2 DATA MODEL AND ML ESTIMATOR

Assuming that all the array elements are characterized by the same disturbance level and that the target echo is received with the same amplitude, received signal over a K element array can be modelled as:

$$\boldsymbol{x} = A\boldsymbol{s}(u_0) + \boldsymbol{n} \tag{61}$$

where A is the target complex amplitude, $\boldsymbol{n}$ is the noise vector of dimension $K\text{x}1$ which is approximated as a K-dimensional Gaussian random variable with zero mean and covariance matrix given by $\sigma^2\boldsymbol{I}_K$; finally $s(u_0)$ is the $K\text{x}1$ steering vector that models the array response for a waveform imping the array from a direction u_0 with respect to the boresight. For a linear array of K receiving elements placed at position d_k $(k = 0, \dots, K-1)$, the steering vector takes the form:

$$\boldsymbol{s}(u_0) = \left[\exp\left(-j\frac{2\pi}{\lambda}d_0u_0\right) \quad \exp\left(-j\frac{2\pi}{\lambda}d_1u_0\right) \quad \dots \quad \exp\left(-j\frac{2\pi}{\lambda}d_{K-1}u_0\right)\right] \tag{62}$$

where λ is the wavelength of the acquired signal. The function:

$$B(u) = \frac{1}{K}|\mathbf{s}^{\mathrm{H}}(u)\mathbf{s}(\mathrm{u}_0)|^2 \tag{63}$$

is known as beam pattern function and determines the magnitude of the received power at every angle. Such function is maximum when $u = u_0$; as u changes the element signals will no longer combine in phase, causing the beam patter to decrease. It represents an intrinsic property of the array and characterizes its performance.

In order to estimate target DoA from the observed data $\boldsymbol{x}$, a Maximum Likelihood DOA estimator is derived. It provides the estimate $\hat{u}_0$ that maximizes the likelihood function of the observed data $\boldsymbol{x}$. Such estimator is widely used as it is easy to derive and it reaches the Cramér Rao Lower Bound (CRLB) when it deals with high SNR.

The probability density function of the received signal $\boldsymbol{x}$ can be written as:

$$p_{\mathbf{x}}(\mathbf{x}\,|u_0, A) = p_{\mathbf{x}}(\mathbf{x}\,|u_0, A) = (\pi\sigma^2)^{-K} exp\left\{\sigma^{-2}\big(\mathbf{x} - A\mathbf{s}(u_0)\big)^H\big(\mathbf{x} - A\mathbf{s}(u_0)\big)\right\}. \tag{64}$$

The ML estimate $\hat{u}_0$ is obtained by maximizing the probability density function above with respect to the unknown signal amplitude A and DoA u_0. After some math, one obtains:

$$V(u) = \frac{1}{K}|\mathbf{s}^{\mathrm{H}}(u)\mathbf{x}|^2 \tag{65}$$

and the ML estimate is:

$$\hat{u}_{ML} \qquad s.t. \qquad V(\hat{u}_{ML}) = \max\big(V(u)\big) \tag{66}$$

When dealing with just two receiving elements, it is easy to verify that the maximum value of (66) may be found in closed form recurring to the interferometric approach; it measures the phase difference of arrival $\Delta\phi$ between the two antennas at distance d to calculate the DoA θ_0 of the target echo, by inverting the following relationship:

$$\Delta\phi = \frac{2\pi d}{\lambda}\sin\theta_0 = \frac{2\pi d}{\lambda}u_0. \tag{67}$$

The greater the distance between the elements, the more accurate is the estimate. However, since the phase difference is measured modulo 2π, the receiving array may not be able to uniquely associate a phase shift to a single direction of arrival. The unambiguous angular sector guaranteed by two elements placed at a distance d and receiving a signal with wavelength λ is:

$$\left[-\frac{\lambda}{2d}; +\frac{\lambda}{2d}\right]. \tag{68}$$

This means that the array provides unambiguous estimates within the angular sector $\pm 90°$ only in the case of half-wavelength spacing ($d \leq \lambda/2$). Considering the two DVB-T frequencies at the edges of the UHF Band (474 and 794 MHz) one should place the elements at a distance equal to $0{,}31$ m and $0{,}19$ m respectively to ensure $\pm 90°$ coverage. This could be a strong constraint due to the physical dimension of the elements and, if this is even possible, it could still be a limiting factor in terms of maximum achievable estimation accuracy.

The constraint to be fulfilled to not have grating lobes in the sector of interest is

$$d < \frac{\lambda}{1 + |u_M|} \tag{69}$$

where $|u_M| = |\sin\theta_M|$ is the maximum DoA that is wanted to be unambiguously estimated.

Monte Carlo simulation (10^6 trials) have been performed to state the performance of the ML estimator for an array of $K = 2$ elements spaced $d = 0.45\,\lambda$ from each other. A Swerling 0 target placed at $60°$ has been simulated. Simulation results are compared with CRLB and are shown in Figure 39. As is apparent there is a good agreement at high SNR but not at low one. As the SNR decreases, the estimator exhibits a threshold phenomenon and the mean square estimation error (MSE) increases rapidly above the CRLB. This is due to sidelobes in the array beampattern causing a false estimate of the target DoA.

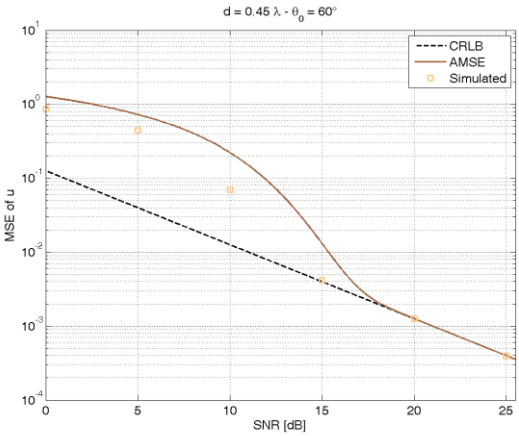

Figure 39 CRLB, AMSE and Monte Carlo simulation versus SNR for $\boldsymbol{u_0 = \sin(60°)}$ and $\boldsymbol{d = 0,45\,\lambda}$.

Observing the results in Figure 39, it is clear that despite having met the constraint (69), one gets large estimation error at SNR values that are operative for a passive radar system. As already introduced, such effect is known as threshold effect and can be considered as a characteristic of the ML estimator for each given array. The main goal is to predict the threshold effect and to identify system configurations that allow to operate in the region of convergence (ML attains CRLB) for nearly all the SNR values of interest. We will investigate strategies that will provide an increase in performance and, at the same time, a relaxation on the constraint on d.

3.6.3 STRATEGY FOR ARRAY SIZING

In the literature many bounds able to predict the threshold effect – shown in Figure 39 – have been presented. In this study it will be used the one in [59], hereafter called AMSE, since it has been proved to be applicable to non-uniform arrays. Unlike the CRLB, which essentially depends on the shape of the mainlobe and only considers small deviations around the true DoA, AMSE takes into account the non-zero probability that sidelobes in the angular sector of interest may be higher than the mainlobe when the received data are corrupted by noise. Errors due to sidelobes are estimated considering their position, their amplitude and the probability of falling into one of them. Resuming the nomenclature of [59], those errors are referred to as outliers. The higher the noise power, the greater the probability of outliers P_o.

As can be seen from Figure 39, AMSE describes better than CRLB the performance of the ML estimator. In this special case of a 2 receiving elements array, AMSE may not track with good accuracy the actual performance of the ML estimator. However, as it will be seen later, it provides a much more realistic estimate of the performance when we consider array with $K = 3$ elements. AMSE can then be used in place of time-consuming computer simulations to foresee performance for any given array configuration thus enabling the research for the 'best array configuration'.

Such research will be conducted as follows. For each configuration it will be evaluated SNR_* as the value for which the probability of false alarm is lower than a fixed threshold $\overline{P_o}$. Among all the considered configurations, only the ones characterized by SNR_* lower than $\mathrm{SNR}_{\mathrm{low}}$ are considered valid. $\mathrm{SNR}_{\mathrm{low}}$ should be set equal to values guaranteeing

acceptable target probability of detection. Once a subset of configurations is individuated, the one ensuring the lowest MSE is chosen. This can be summarized in a constraint and an optimization problem:

$$\begin{cases} \mathrm{SNR}_* < \mathrm{SNR}_{\mathrm{low}} \\ \min\limits_{\boldsymbol{\xi}} (\mathrm{MSE}|_{\mathrm{SNR}_{\mathrm{low}}}) \end{cases} \tag{70}$$

where $\boldsymbol{\xi}$ is a vector containing the relevant parameters for the system design, i.e. inter-element distance and signal wavelength.

As an example, trends of P_o as a function of SNR is shown in Figure 40(a) for three different choices of $\boldsymbol{\xi}$. We now set two thresholds on the maximum desired probability of outlier $\overline{P_o}$ (10^{-3} and 10^{-4}, respectively) and we denote with circles and squares, for each configuration, the values of SNR_* providing a probability of outlier lower than $\overline{P_o}$. $\mathrm{SNR}_{\mathrm{low}}$ is chosen equal to 13 dB. Using the first threshold, two out of three configurations are valid, while only one configuration meets the constraint for $\overline{P_o} = 10^{-4}$. MSE is shown in Figure 40(b); for $\overline{P_o} = 10^{-4}$, the only usable system design is $\mathrm{Conf}\ 1$. If one wants to ensure a probability of outlier lower than 10^{-3}, the configuration that provides the best performance at $\mathrm{SNR}_{\mathrm{low}}$ is $\mathrm{Conf}\ 2$.

It is worth noting that a system dimensioned only through the CRLB would result in the choice of $\mathrm{Conf}\ 3$ as it provides the best performance (lowest MSE) at $\mathrm{SNR}_{\mathrm{low}}$, see Figure 40(b). Actually the sidelobe level in the beambattern of such configuration has a catastrophic effect on the DoA estimation for all the targets detected with a SNR lower than 18 dB.

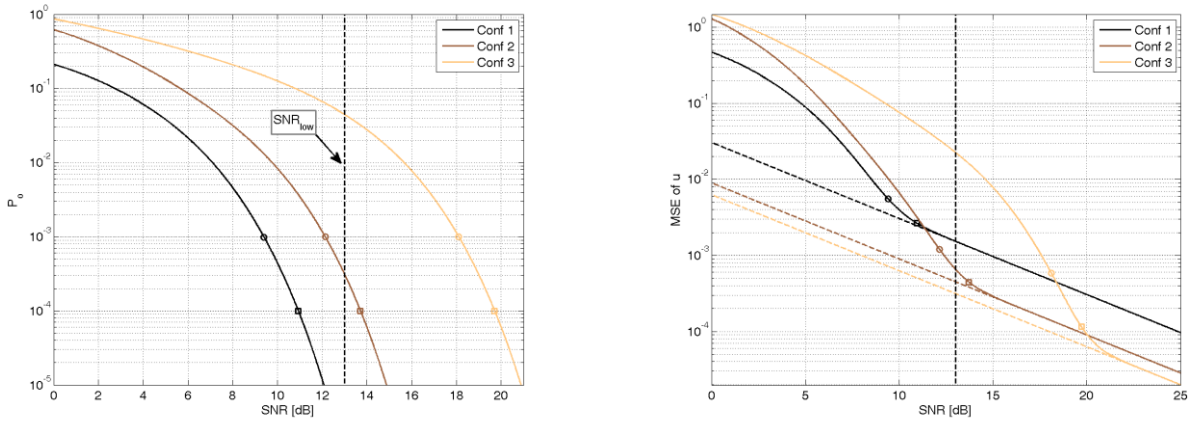

(a) (b)

Figure 40 (a) Probability of outlier as a function of SNR. Markers identify the values of SNR_* for two different threshold of P_o: (circles) 10^{-3}, (squares) 10^{-4}; (b) MSE of u for the configurations. Dashed lines represent CRLB; circles and squares identify values of SNR_* for the two thresholds.

For a given array configuration, the shape of its beampattern essentially depends on the inter-element distance and on the wavelength of the exploited signal; thus one has potentially two degrees of freedom to find the best configuration. Actually, when operating with signals of opportunity one cannot control the choice of the frequencies to be exploited. At most is possible to choose a subset of frequencies from those available in the site of the acquisition, so the only degree of freedom to lower the MSE lies in the positioning of the elements.

Hereafter we denote by d_{0n} the distance of the n-element from the reference element 0. Therefore d_{0N} represents the total size of the N-elements array and is called baseline. As previously seen, when using only two antennas we need to place them at a distance shorter than half the wavelength to not have grating lobes. However there is still the problem of sidelobes to deal with, as can be seen in the top and center plot of Figure 41(a) where the x-axis has been

extended to better understand the problematic. Resorting to a larger number of evenly spaced antennas with inter element spacing $d_n = d < \lambda/2$, one gets – with respect to the 2 elements beampattern – a slight gain in accuracy while maintaining low the level of sidelobes (bottom of Figure 41(a)). A further improvement may be obtained by exploiting baseline diversity. This is shown at the bottom of Figure 41(b) where an even narrower mainlobe has been obtained placing the elements at distances greater than or equal to half the wavelength.

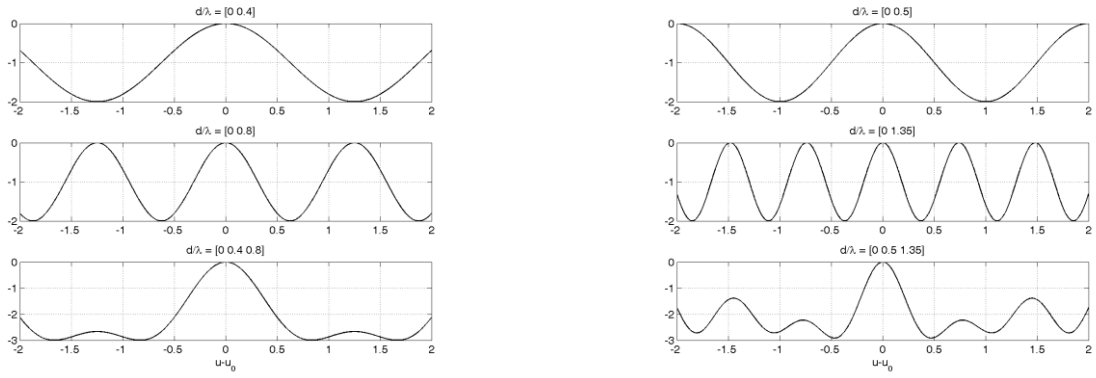

(a) (b)

Figure 41 (Top and Center) of (a) and (b): ML functions for $K = 2$. Elements distance, normalized to λ, from the reference point are reported above each plot. (Bottom) Resulting ML functions for $K = 3$.

The research of the best array configuration will be conducted varying the position of the antennas for a 3 elements array. In particular, we vary the size of the baseline d_{02} and the position of the central element d_{01} between the reference element and half the baseline: symmetric performance are obtained on the second half of the interval. Maximum probability of outlier is set equal to $\overline{P_o} = 10^{-3}$ at a maximum $\mathrm{SNR_{low}} = 13$ dB. Results are shown in Figure 42 for one the highest DVB-T frequency channel (786 MHz); that is because small wavelengths represent a pejorative case for the beampattern shape.

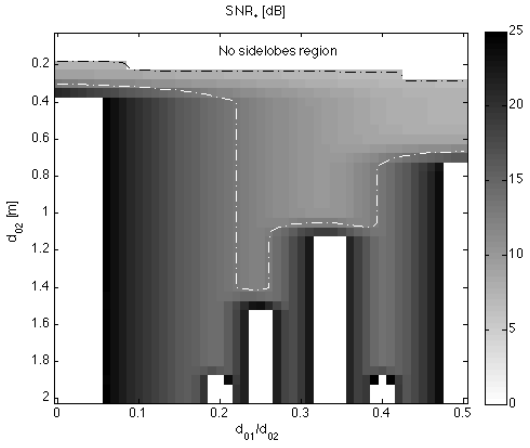

Figure 42 SNR_* for a multi-baseline approach ($K = 3, N = 1$) for $\lambda = 0{,}38\ m$. Array configurations inside the white dashed line are characterized by an SNR_* ($\overline{P_o} = 10^{-3}$) equal to or below the SNR threshold at 13 dB.

The upper white region of the figure represents the set of configurations that, due to the inter-element spacing lower than half-wavelength, do not show sidelobes in the whole angular sector of interest. Therefore, an estimate through one of such configurations would only be affected by small errors in the mainlobe region. White regions in the bottom refer to system configurations characterized by a SNR_* that exceeds the precision of the computer. The remaining part of the figure illustrates the values of SNR_* for all the tested configurations. The region enclosed in the dashed

lines identifies configurations meeting the constraint of equation (70), i.e. $\mathrm{SNR}_* < \mathrm{SNR}_{\mathrm{low}}$. Focusing the interest on valid configurations, MSE at low ($\mathrm{SNR} = \mathrm{SNR}_* = 13$ dB) and high SNR ($\mathrm{SNR} = 20$ dB) has been calculated and plotted in Figure 43.

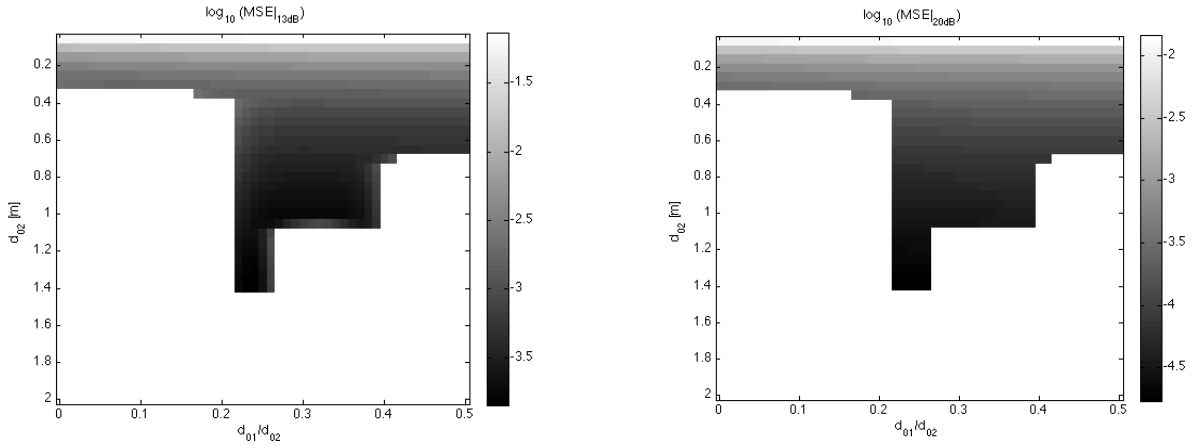

(a) (b)

Figure 43 MSE for a $K = 3$ elements array ($f_c = 786$ MHz) for SNR equal to 13 and 20 dB. Valid configurations are those providing a maximum probability of outlier $\bar{P}_o = 10^{-3}$ at a maximum $\mathrm{SNR}_{\mathrm{low}} = 13$ dB.

As expected the 'No sidelobes region' of Figure 42 is the one characterized by the worst performance (i.e. highest MSE). The absence of sidelobes stems from the fact that the main lobe occupies the whole angular sector examined: this results in a very poor estimation accuracy. As the baseline of the array is increased, the estimation accuracy enhances accordingly. However, there is also a progressive reduction of the spatial interval in which the central element can be placed: this means that positioning errors may lead to configurations with much worse performance than desired. Recurring to a uniformly spaced array (i.e. $d_{01}/d_{02} = 0{,}5$), the maximum baseline meeting the constraint is about $0{,}65\ m$; it could be longer if one recurs to smaller frequency channels. However, it can be noted that baseline diversity allows to greatly enlarge the array size thus obtaining better performance in terms of MSE.

Accepting a higher probability of outlier (i.e. $\bar{P}_o = 10^{-2}$) even larger baseline could be exploited thus enhancing the accuracy of the estimate.

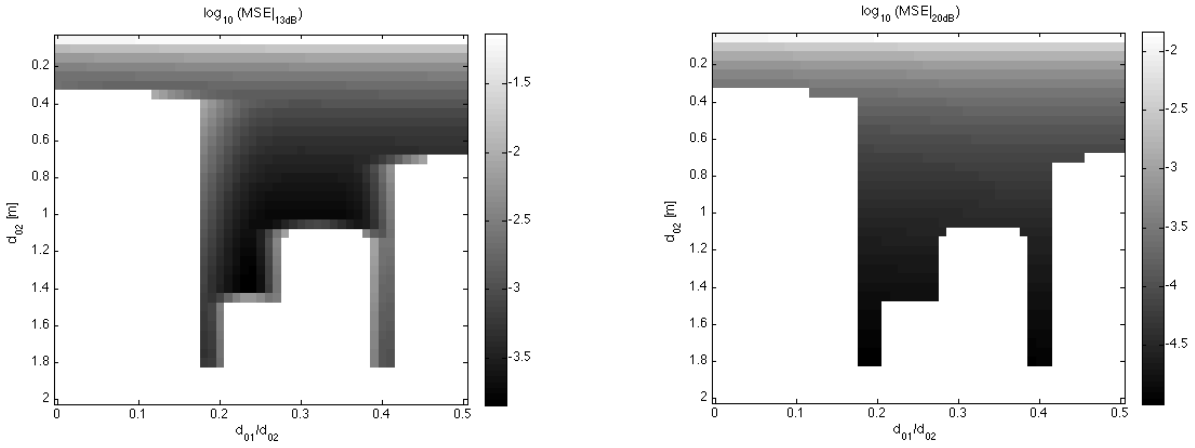

(a) (b)

Figure 44 MSE for a $K = 3$ elements array ($f_c = 786$ MHz) for SNR equal to 13 and 20 dB. Valid configurations are those providing a maximum probability of outlier $\bar{P}_o = 10^{-2}$ at a maximum $\mathrm{SNR}_{\mathrm{low}} = 13$ dB.

Based on the results of Figure 44, the best configuration has been individuated as the one having a d_{01}/d_{02} ratio equal to 0.4. With the objective of using such configuration in the acquisition campaigns along the Italian coastline, elements positions had to take into account the physical size of the antennas. The minimum inter-element distance is 0.63 m; thus the array baseline d_{02} corresponds to 1,55 m.

In this section a functional able to predict the performance of an ML estimator has been presented. Such functional may be used as a useful tool for finding the best position of the array elements. In the following section we present another approach for DoA estimation whose performance may be described by the same functional as well. It has the nice peculiarity of not needing any maximum research process in contrast to the ML estimator; this may result in a computational load saving that may be spent for other operation.

3.6.4 REMAINDER ESTIMATOR

ML estimate is found by looking for a maximum value by means of an extensive research over a grid, whose density is chosen as desired, or exploiting sequential search algorithms. Obviously, the choice on the type of research algorithm has a great impact on the computational load. The Remainder estimator turns out to be an efficient version of the ML estimator as it does not require any process for maximum research while providing similar performance.

Remainder estimator is based on the following observation: DoA estimates provided by couples of antennas positioned at different distance between them are ambiguous with a different period. Thus a disambiguation problem may be solved to retrieve the true target DoA. Such approach is similar to the idea behing the use of staggered PRF in conventional radars to extend the interval of unambiguous radial velocities.

The disambiguation is performed by periodically extending the estimate provided from each pair of antennas with a period given by the size of the unambiguous angular sector related to each couple. Comparing all the possible triples, target DoA estimate is the one corresponding to the smallest distance among the estimates. This allows to obtain unambiguous estimates in a wider angular sector with respect to the ones dictated by the individual pairs; in particular, the new unambiguous angular sector is given by the greatest common divisor (GCD) of the inter-element distances.

A brief example is presented here. Suppose to deal with a 3 element array; this means that up to 3 estimates can be obtained by combining the returns on the 3 pairs of antennas: $\hat{u}_{12}$, $\hat{u}_{23}$ and $\hat{u}_{13}$. Those estimates all belong to the unambiguous angular sector of each pair of antennas they derive from and are replicated according to the periodicity related to the considered pair, thus obtaining the vectors:

$$\left\{\hat{u}_{12_l}\right\}_{l=1:\mathrm{N}_{\mathrm{amb}_{12}}}, \left\{\hat{u}_{13_m}\right\}_{m=1:\mathrm{N}_{\mathrm{amb}_{13}}}, \left\{\hat{u}_{23_n}\right\}_{n=1:\mathrm{N}_{\mathrm{amb}_{23}}}$$

where $\mathrm{N}_{\mathrm{amb}}$ is the number of periods that each pair has within the whole 3 elements unambiguous angular sector. An error vector $\underline{e}_p$ can be defined as:

$$\underline{e}_p = \begin{bmatrix} \hat{u}_{12_l} & - & \hat{u}_{13_m} \\ \hat{u}_{12_l} & - & \hat{u}_{23_n} \\ \hat{u}_{13_m} & - & \hat{u}_{23_n} \end{bmatrix}$$

with dimension $3\mathrm{x}\prod_{l,m,n}\mathrm{N}_{\mathrm{amb}}$. The Remainder estimator consists in minimizing the norm of vector $\underline{e}_p$:

$$\min_p \left\{\left\|\underline{e}_p\right\|^2\right\} \quad \rightarrow \quad p \quad \rightarrow \quad [\hat{u}_{12_l}(p) \quad \hat{u}_{13_m}(p) \quad \hat{u}_{23_n}(p)] \tag{71}$$

3.6.4.1 PRATICAL EXAMPLE OF APPLICATION

ML and Remainder estimators are now applied on a practical example in order to better catch their operating principle. Figure 45 shows the configuration of the considered array; the elements position has been chosen on the

basis of the study conducted in the previous section. The unambiguous angular sector for the frequency 786 MHz ($\lambda = 0.3817\ m$) is equal to about $\pm 38°$.

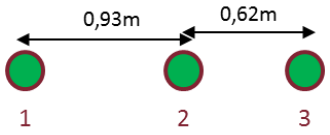

Figure 45 Elements positioning.

A target at $\theta_0 = 30°$ has been simulated. ML estimator performs an extensive research on the entire unambiguous angular sector and opts for the angle that maximizes the likelihood function. In a noise-free scenario, the estimated DoA coincides with the actual target DoA, as is apparent in Figure 46(a). Remainder estimator operates on the individual estimates provided by the 3 couples of antennas (1-2, 2-3, 1-3) within their unambiguous angular sectors; Figure 46(b) shows the likelihood function trends for each pair. Note that blue lines have been sketched to identify the unambiguous angular sectors. The wider sector is provided by the closest pair of elements at the expenses of a wider lobe which is synonym of low accuracy. As can be seen from the figure, separately using the three pairs of antennas one could not retrieve the true target DoA, which is marker with a red dashed line. However by (i) replicating the estimates of each pair with a period which is directly linked to the extent of the unambiguous angular sector and (ii) minimizing the difference between all the possible combinations of replicated estimates, it is possible to solve the ambiguity.

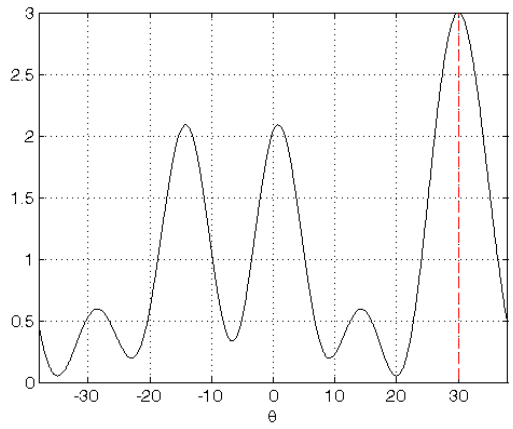

(a)

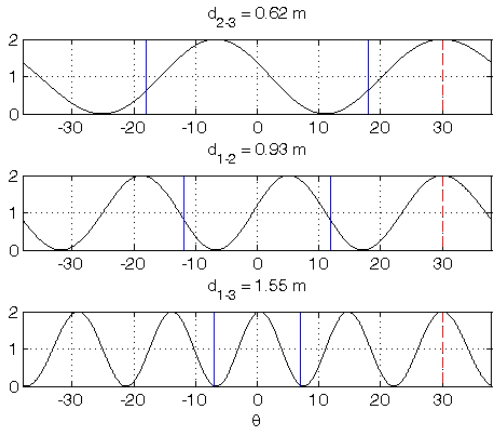

(b)

Figure 46 Likelihood functions trend for the estimate of the DoA of a target at $\theta_0 = 30°$. (a) ML estimator. (b) likelihood function for the three pairs of antennas; blue line represents the unambiguous angular sectors.

3.6.5 PERFORMANCE COMPARISON

The above techniques are now compared via Montecarlo simulations (3.6.5.1) and via application on experimental data sets (3.6.5.2). Some considerations on the elaboration time are also provided.

3.6.5.1 MONTECARLO SIMULATIONS

In this paragraph a performance comparison between the ML and the Remainder estimators is reported. In order to reduce the processing time needed by the Remainder estimator, it has been implemented in a simplified version with respect to the one described in 3.6.4; in this version the estimator processes just two out of the three available pair of

antennas. Performance obtained with the simpler version of the estimator are quite near to the one of the original version and thus it describes faithfully the potentialities of the approach.

Estimators' accuracy has been measured by means of Montecarlo simulations with 10^6 trials. A Swerling 0 target with DoA equal to 0° and 20° has been simulated. As a quality index of the estimators, the Mean Square Error (MSE) of the parameter $u = \sin\theta$ has been calculated. The estimate error is also compared with the CRLB which provides the lowest achievable accuracy of the estimate.

Figure 47 shows MSE of the estimators for DoA 0° and 20°. Blue line represents the CRLB, while black and green markers denote MSE of $\hat{u} = \sin\hat{\theta}_0$ for ML and Remainder estimator respectively. On the x-axis it is reported the SNR on a single antenna. As can be seen when SNR is low, both the estimators widely diverge from the CRLB; this behavior is well known in literature and, under some conditions, it can also be expected. It is important to note that performance of the two estimators are close each other both in high and in low SNR. When SNR is high the closeness of the performance is due to the fact that, once the ambiguity is resolved, the estimation accuracy is mainly driven by the pair of antennas with greater inter-element distance.

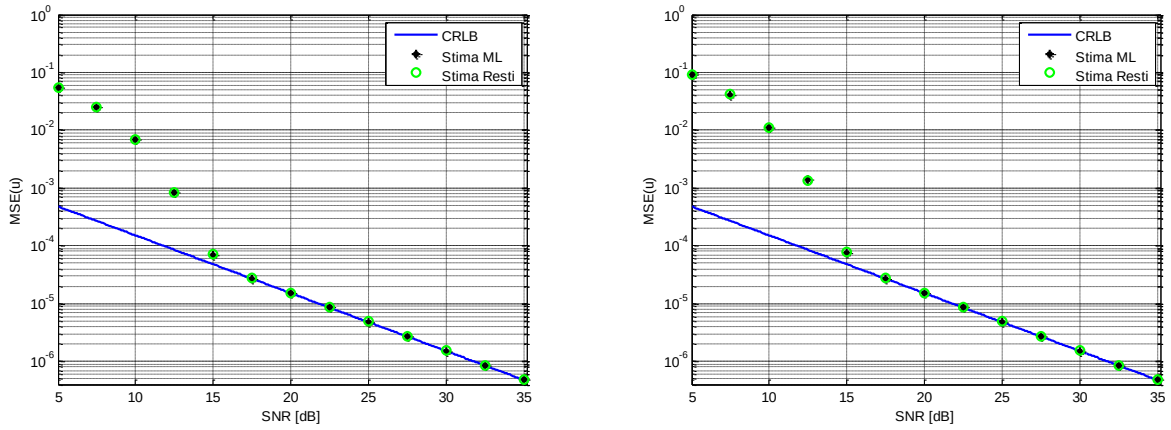

(a) (b)

Figure 47 MSE of $\hat{\mathbf{u}} = \sin\hat{\boldsymbol{\theta}}_0$ as a function of SNR for a target with DoA equal to: (a) 0° and (b) 20°.

3.6.5.2 EXPERIMENTAL DATA SET

In this paragraph an experimental data set is considered for performance comparison; it refers to a cooperative maritime target equipped with a GPS receiver. Due to uncertainties on the temporal alignment between PBR registrations and the GPS receiver, just a limited data set can be considered. For this reason, this analysis cannot be considered exhaustive. In addition, the comparison was performed by visual inspection of the detections of cooperative targets. Opportunity targets cannot be included in such analysis due to the low position accuracy provided by AIS.

Figure 48 shows a GPS track (red line) of a costal patrol boat approaching the receiver; black markers identify PBR detections over 50 consecutive scans. As already seen with simulated data, there is a great similarity between the results.

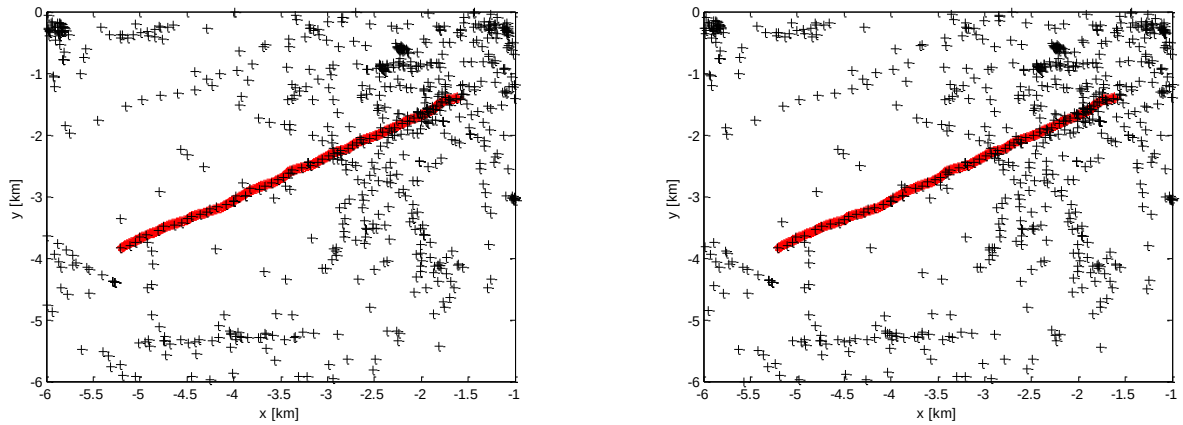

(a) (b)

Figure 48 Visual comparison of DoA estimation of a cooperative target equipped with a GPS receiver. Red line represents the GPS track; black markers denote PBR raw detection. (a) Remainder estimator, (b) ML estimator.

The mean time required by each approach to perform DoA estimation at each of the over 50 consecutive scan (for a mean number of detection amounting to 60) is equal to:

ML estimator	3.1146e-04 s
Remainder estimator	9.1534e-05 s

Even though both the times are quite small compared to execution times required by other blocks in the processing chain, it is important to note that ML estimator needs over three times the amount of time required by the other estimator.

3.6.6 UNBALANCED ARRAY

The two estimators are now compared in a further study aimed at testing their robustness whether an element of the array is characterized by a higher noise level or, equivalently, it captures a lower target amplitude. Another objective of the study was aimed at understanding, in one the situations described before, if it is better to use an interferometer based on the due elements not affected by the increased noise.

Additive noise corrupting the useful signal is still assumed to be white Gaussian noise, however the noise covariance matrix $\boldsymbol{Q}$ has the elements on the main diagonal different from each other. All the other elements are all zero, as the disturbance is assumed to be uncorrelated among the antennas.

For a 3-element array, the covariance matrix has the form:

$$\mathbf{Q} = \begin{bmatrix} \sigma_{n1}^2 & 0 & 0 \\ 0 & \sigma_{n2}^2 & 0 \\ 0 & 0 & \sigma_{n3}^2 \end{bmatrix} \tag{72}$$

Under this novel hypothesis, the ML estimator for unbalanced array has to be derived again. With some simple math, we obtain that the function to be maximized is now:

$$V_{unb}(u) = \frac{|\mathbf{x}^H \mathbf{Q}^{-1} \mathbf{s}|^2}{\mathbf{s}^H \mathbf{Q}^{-1} \mathbf{s}} \tag{73}$$

and the ML estimate is given by:

$$\hat{u}_{ML} \qquad \text{such that} \qquad \mathrm{V}_{\mathrm{unb}}(\hat{u}_{ML}) = \max\left(\mathrm{V}_{\mathrm{unb}}(u)\right) \tag{74}$$

This estimator leads back to the one in (66) whether the antennas are all characterized by the same noise power.

3.6.6.1 PERFORMANCE COMPARISON VIA MONTECARLO SIMULATIONS

Montecarlo simulations (10^6 trials) have been performed for performance comparison between (i) ML estimator, (ii) Remainder estimator and (iii) interferometer. The elements of the array are spaced as in Figure 45.

As a first test, one of the antennas is highly stressed and it is assumed that it catches a 15 dB higher noise power with respect to the others. Figure 49 – Figure 51 show estimators' performance varying the faulty antenna. It is apparent that the ML estimator – which is the ideal estimator under the considered hypothesis – provides better performance with respect to the Remainder estimator. For an unbalanced array, those techniques have not similar performance as it was in the balanced case.

Referring to Figure 49 – which represents a fault on antenna 1 – it is possible to make some considerations:

- the interferometric estimate even recurring to the two 'healthy' antennas is not able to reach the CRLB; that is because the first antenna has way more impact on the accuracy of the estimate that the second antenna.
- when the target lies within the unambiguous angular sector of the 'healthy' pair of antennas, the interferometric estimate is always more accurate than the ones obtained exploiting all the antennas' returns. However as soon as it falls outside of this sector, the estimate of its DoA becomes ambiguous and it does not attain the CRLB even at high SNRs

Figure 50 and Figure 51 show results in case of a fault on the second and third receiving antenna respectively. In case of a higher noise power on the second antenna, the performance of the interferometer gets highly close to the CRLB as the 'healthy' antennas are those at the edges of the array. On the other hand, this pair of antennas is characterized by a narrower unambiguous angular sector with respect to the ones of the other cases.

Actually as the SNR difference among the antennas might be much lower than 15 dB, it is important to investigate the estimators' performance even for cases of a lower unbalancing between the elements. Reasonable values of unbalance between one element and the others may be 3-6 dB. In such cases (see Figure 52-Figure 54 and Figure 55-Figure 57) performance of both ML estimator and Remainder estimator resemble those of 3.6.5.1. The interferometer is not recommended as it is characterized by a narrower unambiguous angular sector. In addition, its performance are better than those of the 'opponents' just for SNR values so low that it is not even guaranteed the detection of such a target level return.

ML estimator generally provides better performance that Remainder estimator, however it requires the a priori knowledge of the disturbance level on the antennas. Such level is estimated from the received data, so it will be affected by some errors. For this reason, additional studies should be performed to evaluate the impact of errors on the disturbance level estimation on the estimator performance. It is also important to notice that such estimation requires a higher computational load.

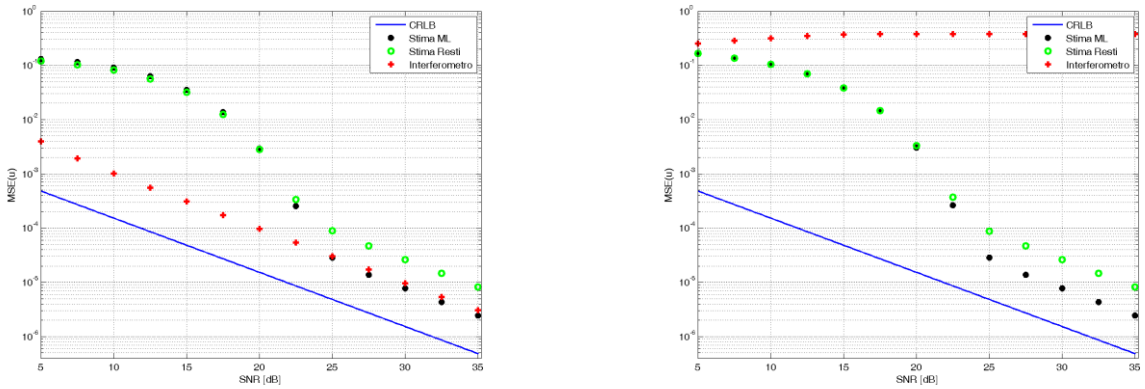

(a) (b)

Figure 49 Antenna #1 with a target loss equal to 15 dB. MSE as a function of SNR for performance comparison via Montecarlo simulation in case of unbalanced noise power on the receiving elements. DoA estimation of: (a) target at 0° and (b) target at 20°.

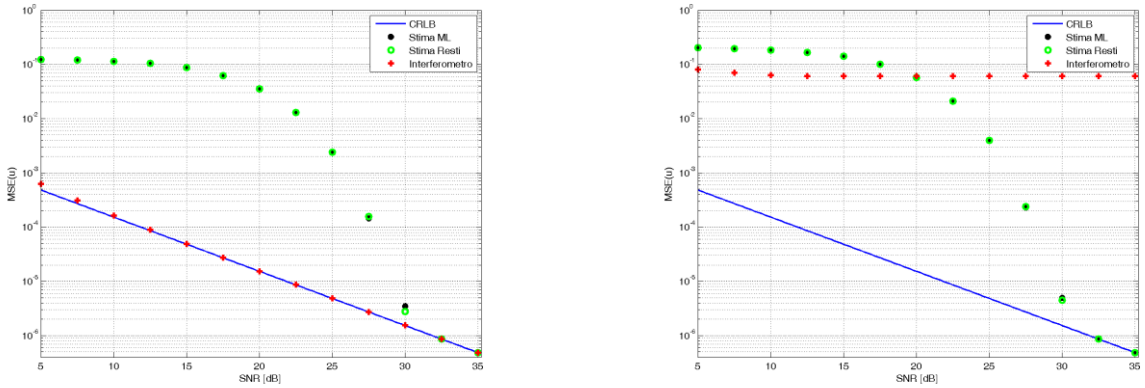

(a) (b)

Figure 50 Antenna #2 with a target loss equal to 15 dB.

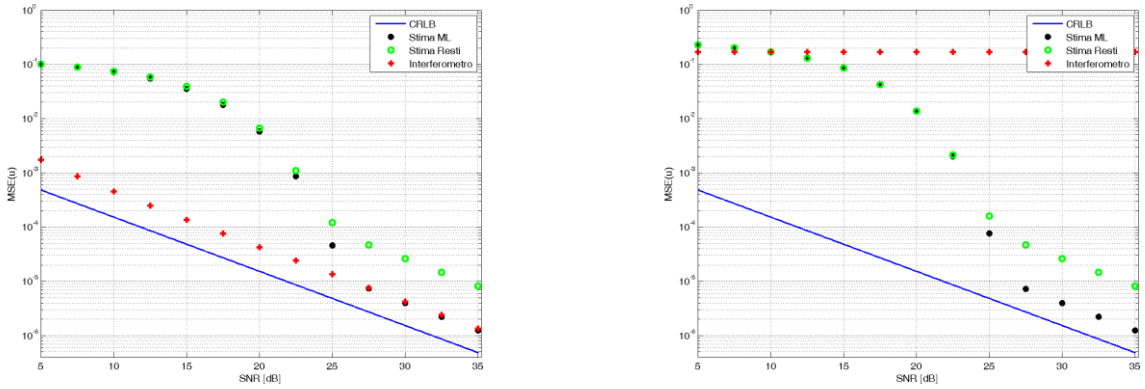

(a) (b)

Figure 51 Antenna #3 with a target loss equal to 15 dB.

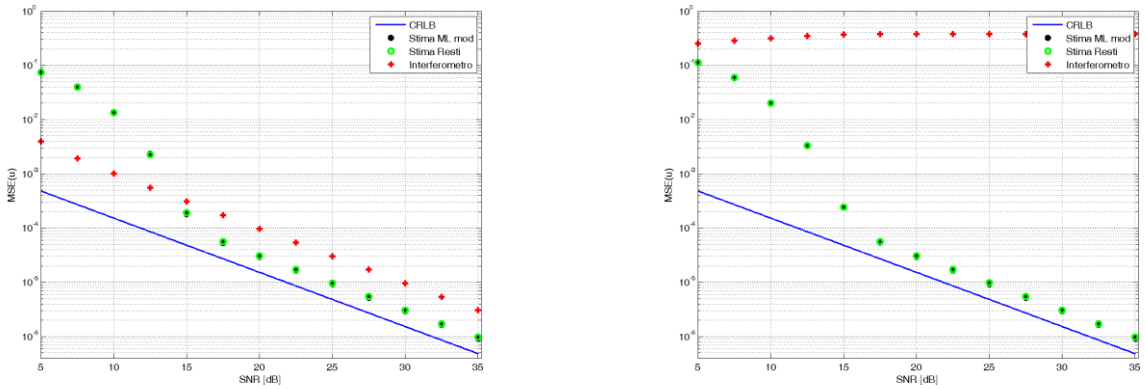

(a) (b)

Figure 52 Antenna #1 with a target loss equal to 3 dB. MSE as a function of SNR for performance comparison via Montecarlo simulation in case of unbalanced noise power on the receiving elements. DoA estimation of: (a) target at 0° and (b) target at 20°.

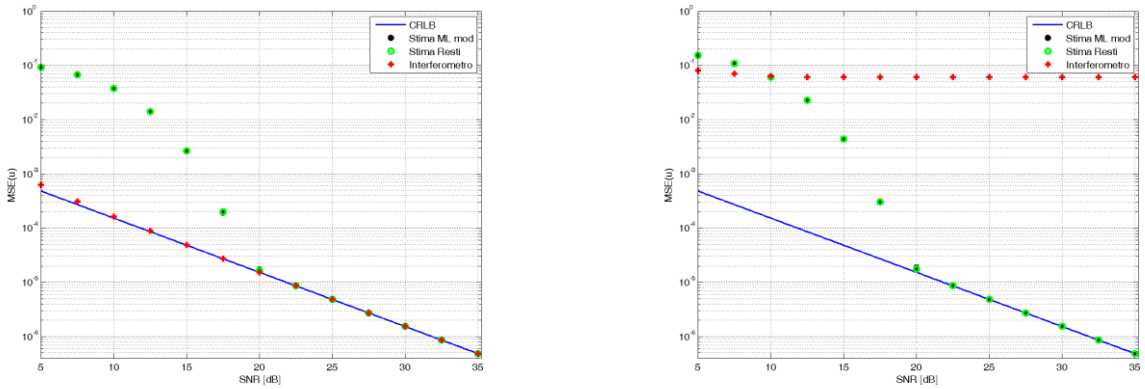

(a) (b)

Figure 53 Antenna #2 with a target loss equal to 3 dB.

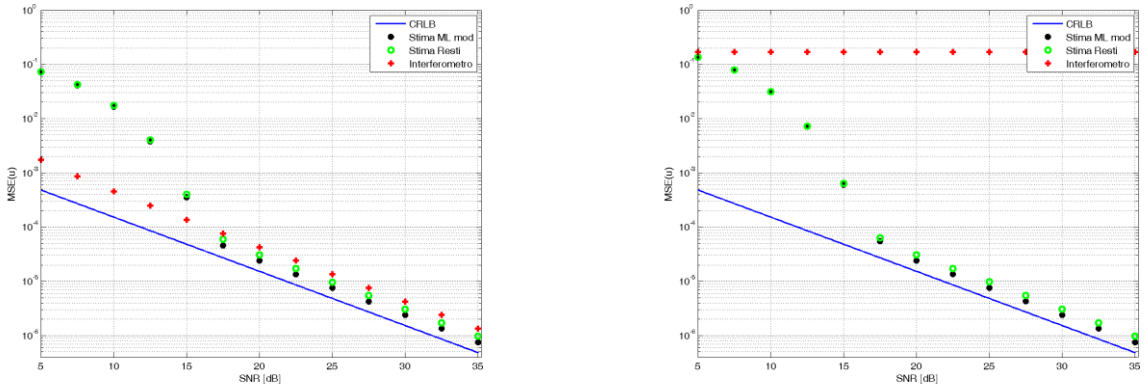

(a) (b)

Figure 54 Antenna #3 with a target loss equal to 3 dB.

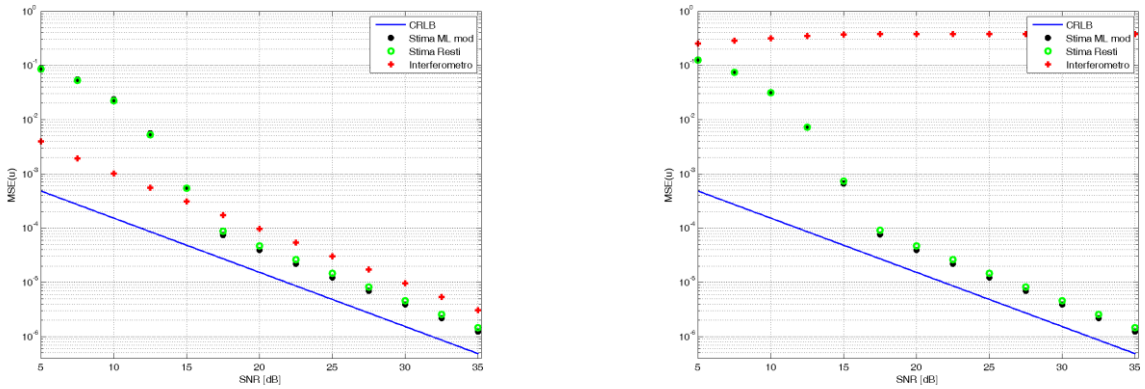

(a) (b)

Figure 55 Antenna #1 with a target loss equal to 6 dB. MSE as a function of SNR for performance comparison via Montecarlo simulation in case of unbalanced noise power on the receiving elements. DoA estimation of: (a) target at 0° and (b) target at 20°.

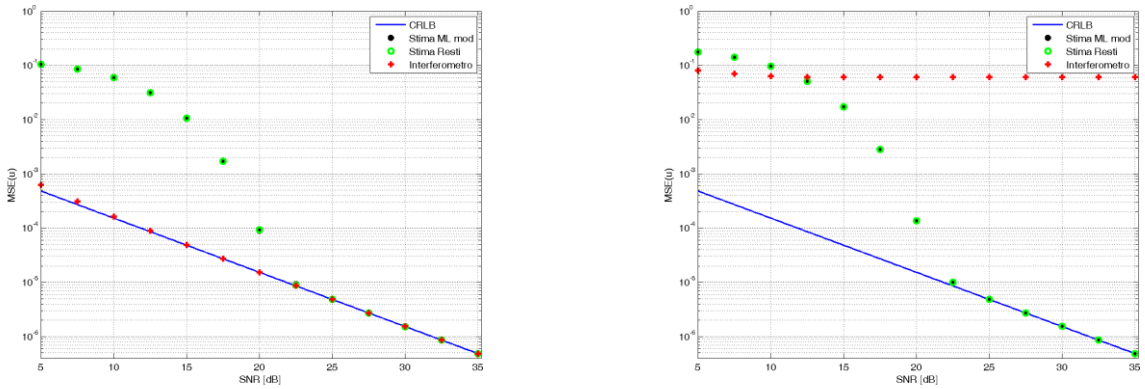

(a) (b)

Figure 56 Antenna #2 with a target loss equal to 6 dB.

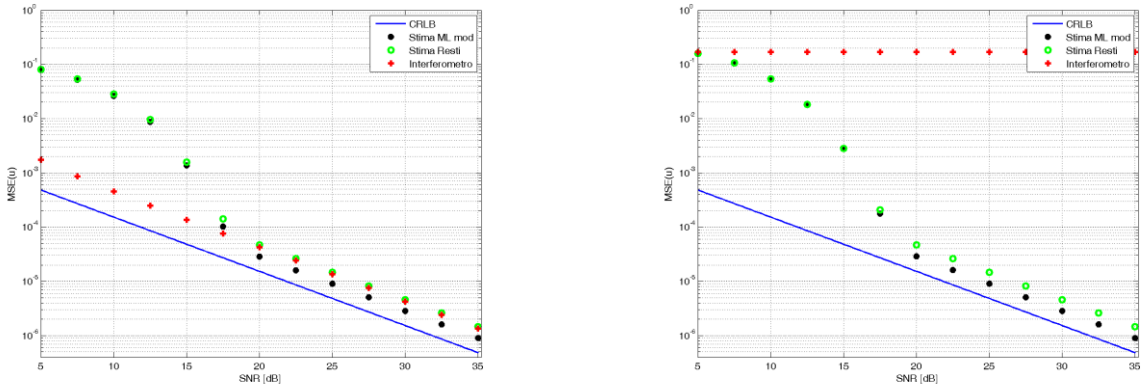

(a) (b)

Figure 57 Antenna #3 with a target loss equal to 6 dB.

3.6.7 RESULTS FROM THE ACQUISITION CAMPAIGNS

The study conducted in 3.6.3 has been the basis for the individuation of the best array configuration; the latter has been used during the acquisition campaigns along the Italian coastline. Results reported below show the effectiveness of multi-baseline diversity in increasing the unambiguous angular sector of the array. Comparison against performance obtainable with just two elements is also reported.

The best array configuration is the one depicted in Figure 45. As the greatest common divisor of the inter-element distances is equal to $0{,}31$ m, the unambiguous angular sector provided by the array collecting a signal with carrier frequency $f_c = 634$ MHz is equal to about $\pm 49°$. Performing interferometric DoA estimation recurring to two out of three elements, the resultant unambiguous angular sectors are: $\pm 14.7°$ for antennas #1-#2, $\pm 22.4°$ for antennas #2-#3 and $\pm 8.8°$ for antennas #1-#3.

Detections on the bistatic Range-Doppler and on the Cartesian planes are reported in Figure 58-Figure 61. With light colours (green, blue and and ochre) we denote true targets position based on AIS (Automatic Identification System) transmissions. Dark versions of the same colours identify PBR detections at the output of the tracker for an acquisition of 314 consecutive scans; in addition, two light grey tracks are visible and are likely to belong to ships not equipped with AIS. To help understand the impact of inter-element distance for DoA estimation, the unambiguous angular sector provided by each pair of antennas as well as the one by the full three elements array have been plotted with grey lines. Black circles on them identify a range of 20 km.

Comparing the results on the Cartesian plane, one notes that recurring to three receiving elements (placed exploiting baseline diversity) one is able to correctly locate all the targets moving within the relative angular sector. Antenna pair #2-#3, which provides the wider angular sector, is characterized by lower estimation accuracy; this can be noted from the higher 'noisiness' of the tracks. Indeed, adopting baseline diversity one obtains the nice advantage of enhancing the accuracy without giving up on the angular coverage.

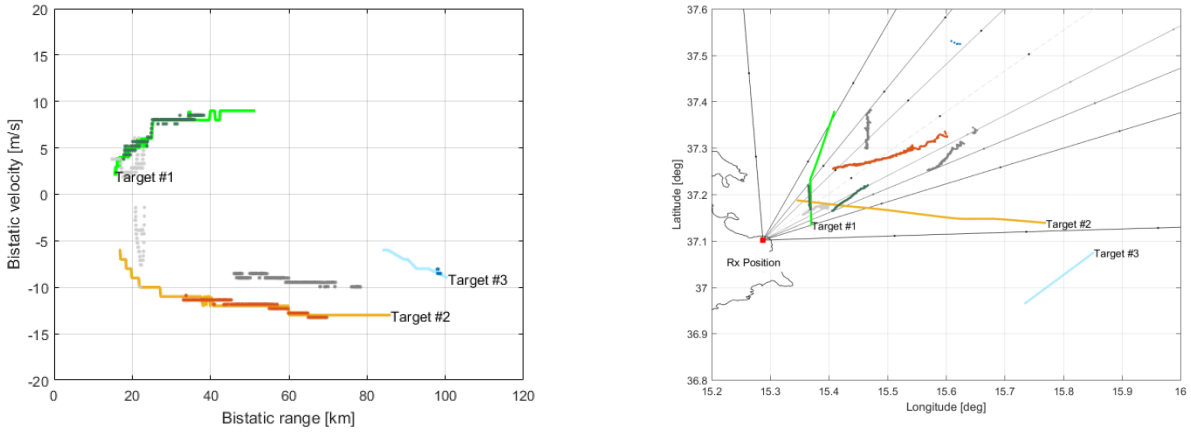

(a) (b)

Figure 58 DoA estimation with interferometric approach exploiting antennas #1-#2. (a) Bistatic plane, (b) Cartesian plane.

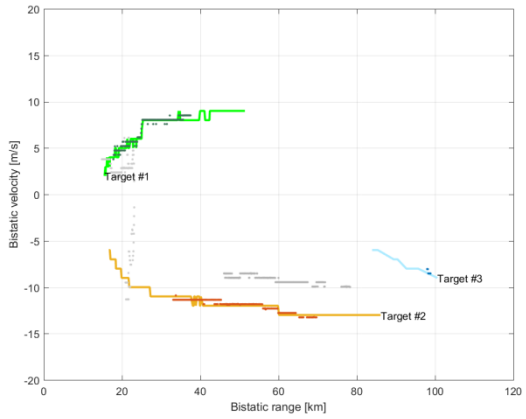

(a)

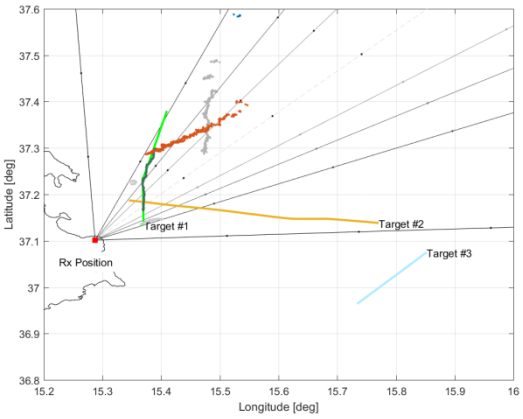

(b)

Figure 59 DoA estimation with interferometric approach exploiting antennas #2-#3.

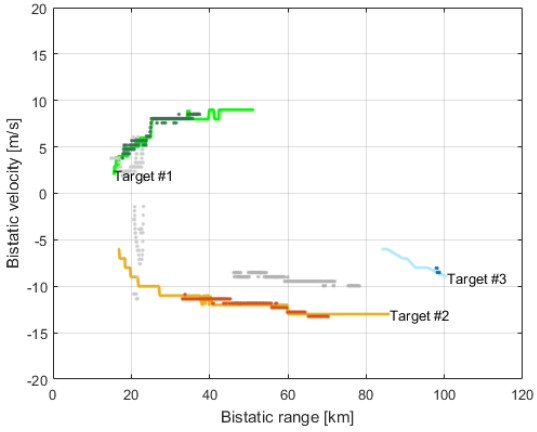

(a)

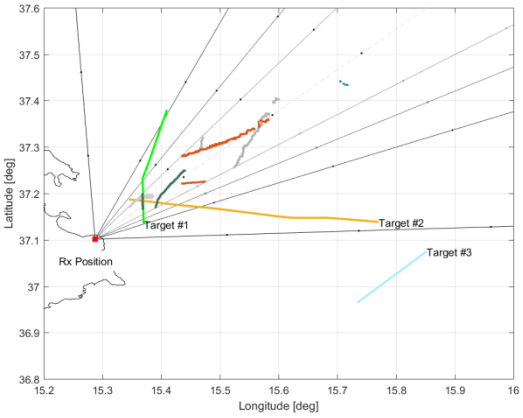

(b)

Figure 60 DoA estimation with interferometric approach exploiting antennas #1-#3.

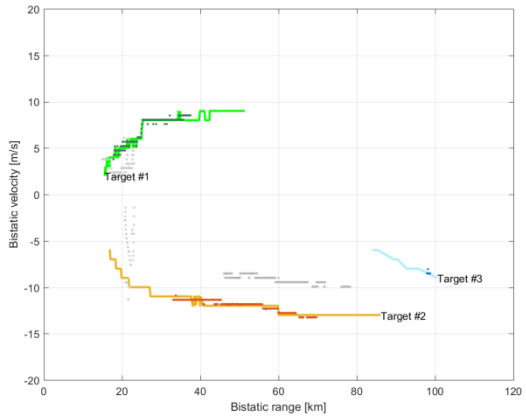

(a)

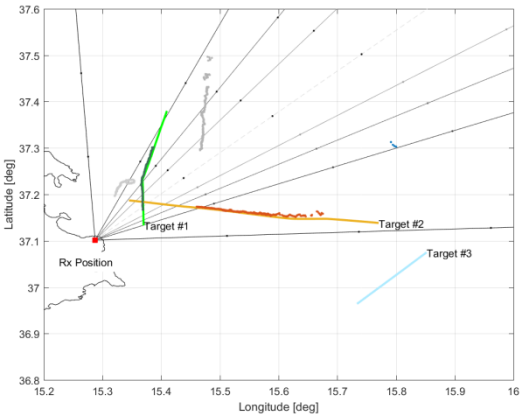

(b)

Figure 61 DoA estimation with Remainder estimator exploiting antennas #1-#2-#3.

Same results have also been summarized in Table 23. Each AIS equipped target has been labeled and information about its size and position on the bistatic plane have been reported. In particular, their angular location with respect to the array boresight (see column 'Case') has been tagged in the following way: tag 4 indicates DoA position within the unambiguous angular sector of the closest pair of antennas (i.e. #2-#3), 3 refers to a target lying inside the angular sector provided by #1-#2, tag 2 is applied for target's position within the angular sector of antennas #1-#3, tag 1 for targets within the angular sector of the whole three elements array and, finally, tag 0 is given to targets outside of each possible angular sector.

The only target tagged with 0 (Target #3) is effectively ambiguously folded within the angular sector of each considered configuration, as is confirmed by the figures above (light blue line indicates the ground truth and blue dots represent PBR detections).

Results for other acquisitions are shown Table 24 and Table 25. As can be seen, unambiguous DoA estimation is obtained even for very small targets (e.g. Target #2 of Acquisition 2 and Target #3 of Acquisition 3); it is a quite interesting result as those targets are likely to be characterized by low SNR.

Table 23 DoA estimation summary for Acquisition 1 (314 consecutive scans).

Scans	Target	Type	Dimension	Bistatic Range [km]	Bistatic Velocity [m/s]	DOA PCL [deg]	DOA AIS [deg]	Case	DoA Estimate	Detection Continuity
1-30	TARGET #1	Cargo	46.6m × 9m	18	4,5	-2,5 ÷ -3	-2,5 ÷ 5	4	Not Ambiguous	Excellent
30-60	TARGET #1	Cargo	46.6m × 9m	20	5	-2 ÷ -8	-4 ÷ -8	4	Not Ambiguous	Excellent
	TARGET #2	Tanker	249.99m × 44.05m	70	-13,3	37,5	39,5	1	Not Ambiguous	Poor
60-90	TARGET #1	Cargo	46.6m × 9m	22	5,6	-8,5 ÷ -12	-8 ÷ -12	3	Not Ambiguous	Excellent
	TARGET #2	Tanker	249.99m × 44.05m	67,5	-13,2	36,5	39,5	1	Not Ambiguous	Good
90-120	TARGET #1	Cargo	46.6m × 9m	24	6	-13 ÷ -16	-12 ÷ -15,5	2-3	Not Ambiguous	Excellent
	TARGET #2	Tanker	249.99m × 44.05m	61	-12,6	37	38,5	1	Not Ambiguous	Excellent
120-150	TARGET #1	Cargo	46.6m × 9m	26	8	-16,2 ÷ -17,4	-15,4 ÷ -16,8	2	Not Ambiguous	Excellent
	TARGET #2	Tanker	249.99m × 44.05m	57	-12,2	36	37	1	Not Ambiguous	Excellent
150-180	TARGET #1	Cargo	46.6m × 9m	29	8	-17,5 ÷ -18,8	-17 ÷ -18	2	Not Ambiguous	Excellent
	TARGET #2	Tanker	249.99m × 44.05m	53	-12	35	35,5	1	Not Ambiguous	Excellent
180-210	TARGET #1	Cargo	46.6m × 9m	32	8	-18,8 ÷ -19,4	-18,1 ÷ -18,9	2	Not Ambiguous	Excellent
	TARGET #2	Tanker	249.99m × 44.05m	49	-12	33	33,5	1	Not Ambiguous	Excellent
210-240	TARGET #1	Cargo	46.6m × 9m	34,5	8,3	-19,5 ÷ -20,5	-19 ÷ -19,8	2	Not Ambiguous	Excellent
	TARGET #2	Tanker	249.99m × 44.05m	44,5	-11,6	30,5	30,5	1	Not Ambiguous	Excellent
240-270	TARGET #1	Cargo	46.6m × 9m	37	8,4	-20,5	-20,2	2	Not Ambiguous	Discrete
	TARGET #2	Tanker	249.99m × 44.05m	40,5	-11,6	27,5	27,5	1	Not Ambiguous	Excellent
270-300	TARGET #2	Tanker	249.99m × 44.05m	36,5	-11,4	24	24,5	1-2	Not Ambiguous	Excellent
300-314	TARGET #2	Tanker	249.99m × 44.05m	33,8	-11,3	21,5	22	2	Not Ambiguous	Excellent
	TARGET #3	Cargo	176.6m × 26m	98,5	-8,5	21	51	0	Ambiguous	Excellent

Table 24 DoA estimation summary for Acquisition 2 (103 consecutive scans)

Scans	Target	Type	Dimension	Bistatic Range [km]	Bistatic Velocity [m/s]	DOA PCL [deg]	DOA AIS [deg]	Case	DoA Estimate	Detection Continuity
1-30	TARGET #1	Cargo	134.61m × 22.75m	36,5	7,6	5,5 ÷ 9	5,5 ÷ 10,5	3-4	Not Ambiguous	Excellent
	TARGET #2	Tanker	112m × 18.2m	20,5	9,5	24,5 ÷ 28	24,5 ÷ 28	1	Not Ambiguous	Very good
	TARGET #3	Tug	27m × 8.18m	17,5	-3	8 ÷ 16	8 ÷ 18	2-3-4	Not Ambiguous	Excellent
30-60	TARGET #1	Cargo	134.61m × 22.75m	39	8,5	4 ÷ 1,5	5,5 ÷ 1,5	4	Not Ambiguous	Excellent
	TARGET #3	Tug	27m × 8.18m	16,5	-2,5	18 ÷ 28	19 ÷ 29	1-2	Not Ambiguous	Excellent
60-90	TARGET #1	Cargo	134.61m × 22.75m	42,5	8,8	0,5 ÷ -2	1 ÷ -2	4	Not Ambiguous	Excellent
90-103	TARGET #1	Cargo	134.61m × 22.75m	44,2	9	-2,8	-3,2	4	Not Ambiguous	Excellent

Table 25 DoA estimation summary for Acquisition 3 (84 consecutive scans)

Scans	Target	Type	Dimension	Bistatic Range [km]	Bistatic Velocity [m/s]	DOA PCL [deg]	DOA AIS [deg]	Case	DoA Estimate	Detection Continuity
1-30	TARGET #1	Cargo	109.39m × 21m	73	-11	-9,5 ÷ -8,1	-9,4 ÷ -9	3-4	Not Ambiguous	Good
	TARGET #2	Sailing	12m × 2m	6,5	2	-22 ÷ -26	-22 ÷ -26	1	Not Ambiguous	Excellent
	TARGET #3	Tanker	115.3m × 16.8m	90-120	10	3,3 ÷ 3,8	4,5	4	Not Ambiguous	Poor
30-60	TARGET #1	Cargo	109.39m × 21m	70	-11	-10,8 ÷ -9,6	-10,1 ÷ -9,6	3	Not Ambiguous	Excellent
	TARGET #2	Sailing	12m × 2m	7,5	2,5	-27 ÷ -29	-25,5	1	Not Ambiguous	Very good
	TARGET #3	Tanker	115.3m × 16.8m	15	-8	18	80	0	Ambiguous	Good
60-84	TARGET #1	Cargo	109.39m × 21m	66	-11	-11 ÷ -10,4	-10,5 ÷ -10,4	3	Not Ambiguous	Good
	TARGET #3	Tanker	115.3m × 16.8m	1,2	-7	-20	65	0	Ambiguous	Poor

In Figure 62 further results from analysis on the experimental data set are shown. In this case a 90 scan long acquisition is considered; such data set was collected with just two surveillance antennas, as can be seen by the high trembling of the detected tracks on the Cartesian plane.

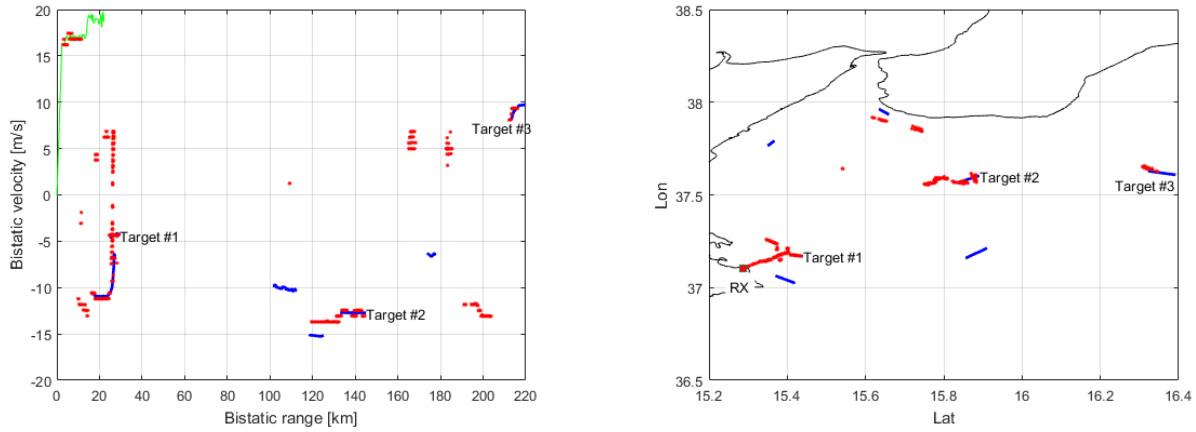

(a) (b)

Figure 62 Red dots stand for PBR detections where blue and green lines refer to ground truth of opportunity and cooperative targets, respectively. (a) Detections on the bistatic plane (b) Detections on the Cartesian plane.

Such results are reported to show the incredible performance obtained by the system in detecting targets at very long range (over 200 bistatic kilometres, about 100 monostatic kilometres). The system showed such performance more than once during the acquisition campaign. This means that the system is able, exploiting anomalous propagation effects, to detect over the horizon target. Red dots superimposed on the green line refers to detections of a small cooperative target equipped with a GPS receiver; this clearly shows the nice capability of the system in detecting both small targets at near range and large target at far range.

3.6.8 CONCLUSIONS

In this section, it has been described the strategy adopted to perform the dimensioning of the receiving array. The goal was to perform high accuracy target DoA estimation in a wide angular sector exploiting few receiving elements.

First of all, the ML estimator – which is one of the most widely used method for DoA estimation – has been derived. Then some consideration about its capacity to describe the achievable estimation accuracy has been provided. It turned out that performance of ML estimator is well described by CRLB when SNR is high; in contrast, CRLB is no longer useful when SNR lowers below a certain value. In order to predict, for each possible configuration of the array, performance of the estimator even at low SNR a better suited functional than CRLB has been exploited and described. Based on it, a dimensioning strategy could be developed in order to find the optimal configuration of the array.

Once found the best array configuration, whose performance are well described by the considered analytical functional, our goal has been to find another estimator that, in contrast to ML estimator, does not require any process for maximum research thus providing lower computational load. The described method goes under the name ‘Remainder estimator’.

Those estimators have been compared both via Montecarlo simulations and application on experimental data set; results show a very good performance agreement. A further comparison has been made with simulated data assuming the array was working in a more complicated scenario (the disturbance level on the receiving antennas is not the same). Under this conditions we saw that the Remainder estimator deviates from the ML, but such deviation is acceptable for an SNR unbalancing of the order of 3-6 dB.

Finally, the approaches have been applied to the data collected on several acquisition campaigns. Results showed that the array configuration found at the output of the dimensioning strategy provides, at the same time, wide unambiguous angular sector and appreciable estimation accuracy. Nice results have been obtained also for small targets (i.e. tug and sailing vessels) at medium range that are likely to have been detected with small SNR. Exploiting baseline diversity larger baseline could be obtained thus more faithful estimate of targets DoA as achieved.

3.7 MULTI-FREQUENCY INTEGRATION

3.7.1 INTRODUCTION

An experimental analysis carried over few data sets has been conducted trying to integrate the detections obtained exploiting multiple frequency channels transmitted from the same broadcasting site.

Multi-frequency integration is expected to enhance the performance of the system as it allows to face degradation due to instantaneous characteristics of the electro-magnetic environment. The signals received at multiple frequency channels might be jointly exploited to: (i) make the detection scheme robust with respect to the propagation channel conditions, and (ii) improve the detection and localization capabilities of the system by properly combining the measurements obtained using the signals transmitted at different carrier frequencies.

Some of the approaches described in [27] have been applied to a limited data set collected. It has been noted that due to the different case of application (maritime surveillance instead of aerial surveillance) and waveform (DVB-T instead of FM radio) such approaches cannot be directly applied. In fact, even though the exploited DVB-T channels were broadcasted by the same transmitter, detections of a target seen on all the frequencies appeared on the RDM at different ranges.

The section is organized as follows: approaches for multi-frequency integration are briefly described in 3.7.2; conducted experimental analysis is shown in 3.7.3 prior to derive conclusions in 3.7.4.

3.7.2 APPROACHES FOR MULTI-FREQUENCY INTEGRATION

Exploiting frequency channels that are transmitted from the same broadcaster has the nice advantage of observing a specific target at all channels with the same bistatic range and velocity. However different channels have different carrier frequencies so that the echo from the same target is received with different Doppler frequencies. Using the same integration time T_{int} at each carrier frequency f_n, one obtains the same Doppler resolution Δf, which in turn yields a slightly different velocity resolution Δv_n.

However it would be useful to obtain range-velocity maps that are directly comparable, thus it is necessary to use slightly different integration times $T_{int\,n}$ on the N_{ch} exploited channels, according to the criterion:

$$\boldsymbol{\Delta v_n} = \frac{c}{f_n} \cdot \frac{1}{T_{int}} = \text{costant} = \Delta v \quad \Rightarrow \quad T_{int\,n} = \frac{c}{\Delta v \cdot f_n} \quad n = 0, \dots, N_{ch} - 1 \tag{75}$$

In this way the range-velocity maps obtained over the different collected channels can be integrated pixel-by-pixel abd the coincides of the detections can be exploited both to increase the detection capability (reducing the undesired degradations of the single channel waveform/environment) and to reduce false alarms.

For the purpose a non-coherent integration may be considered. In the following, it will be presented some approaches for non-coherent integration; those may be categorized as centralized or decentralized approaches depending on whether data fusion occurs. Centralized approaches require the combination of the range-velocity maps prior to perform CFAR detection, on the other hand decentralized approaches perform data fusion after each map passes through a separate CFAR channel.

Centralized linear integration (SUM)

After having obtained a range-velocity map for each exploited channel, the value x_p of the p-th pixel in the integrated map is written as:

$$x_p = \sum_{n=0}^{N_{ch}-1} z_{n,p} \tag{76}$$

where $z_{n,p}$ is the p-th pixel of the map relative to channel n.

Assuming that most of the exploited channels yield a reasonable SNR at the range-velocity location of a given target, their maps are incoherently summed aiming at enhancing the resulting SNR on the integrated map. With this approach, the instantaneous characteristics of the bad channels are likely to be averaged with the good ones thus yielding a limited impact on the final detection performance.

Decentralized integration L/N_{ch} (DEC)

This is a binary integration approach that applies a first detection threshold separately on each channel. According to this strategy, a detection is declared at a given pixel when L detections out of N_{ch} channels are obtained for the considered pixel of the single channel maps. The advantage of such approach is given by the robustness against 'bad' channels characterized by high sidelobes or undesired structures in the map.

In addition to the standard integration approaches shown above, non-linear detection rules will be now described. those allow to remove the impact of 'bad' channels. In particular, the maximum and the minimum modulus can respectively be considered. The former guarantees that the highest value is always retained to avoid degrading good target echoes, whereas the latter aims at considering only very reliable targets, whose echoes are received with a reasonably high value at all the channels. So it can be defined also:

Centralized non-linear integration MAX

Assuming that only one or few exploited channels yield a significant SNR at the range-velocity location of a given target, the the p-th pixel in the integrated map is written as:

$$x_p = \max\{z_{n,p}\}_{n=0,\dots,N_{ch}-1} \tag{77}$$

This approach has the drawback of preserving the sidelobes structures.

Centralized non-linear integration MIN

Aiming at significantly reducing the high peaks in the map due to 'bad' channels, a minimum approach should be implemented by selecting, for each map location, the minimum value among the corresponding pixels on the single channel maps. In this case, the pixel after integration can be written as:

$$x_p = \min\{z_{n,p}\}_{n=0,\dots,N_{ch}-1} \tag{78}$$

This approach is expected to yield reasonable detection performance only when all the exploited channels yield reasonable SNR at the range-velocity location of a given target.

3.7.3 EXPERIMENTAL ANALYSIS

Those approaches are now compared exploiting an experimental data set collected on June, 2015. Data were acquired with two surveillance antennas and were processed with a conventional processing scheme comprising: (i) sidelobe level control (ii) disturbance cancellation via ECA (iii) evaluation of the RDM with CPI of 1 second (iv-a) frequency integration and CFAR detection when employing centralized approaches or (iv-b) CFAR detection and frequency integration for decentralized approaches and, finally, (v) '2-out-2' integration criterion among surveillance channels.

Best of the acquired channels are those at 482 MHz (hereafter indicated as F1) and at 650 MHz (F2). Raw detections over 90 consecutive scans are reported in Figure 63. Red dots represent PBR detections, while blue and green lines stand for ground truth of opportunity and cooperative targets, respectively.

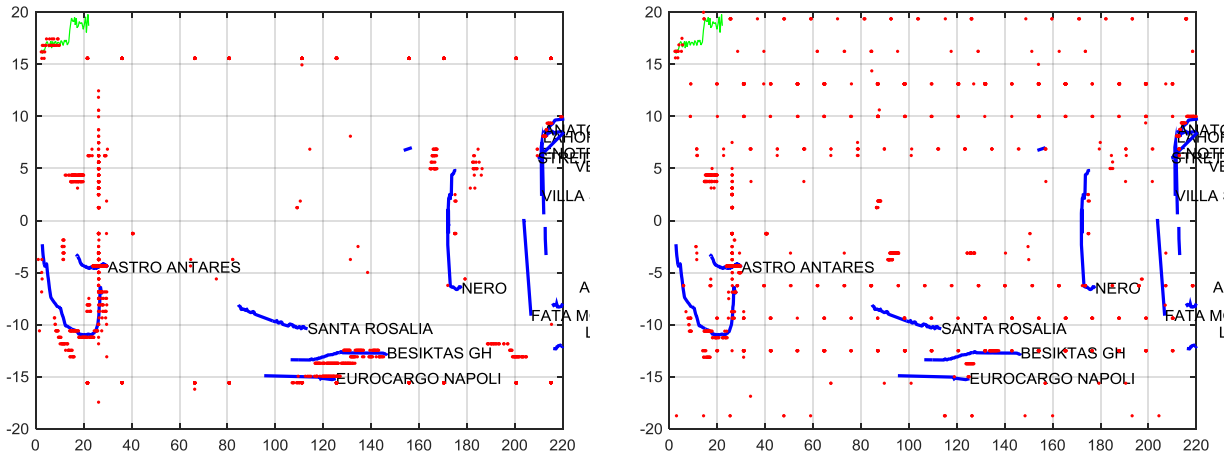

(a) (b)

Figure 63 Raw detections over 90 consecutive scans for: (a) 482 MHz and (b) 650 MHz.
(x-axis: bistatic range [km] y-axis: bistatic velocity [m/a])

Those target that are not detected at all by any frequency channel are likely to lie outside of the surveillance region.

F2 is much noisier of F1, however those frequencies provide good detection continuity for almost all of the targets in the scene. In particular, F1 better acts against the near cooperative target, while F2 exhibits more detections for targets at far range (see Figure 64 and Figure 65 where beside each detection is reported the scan index).

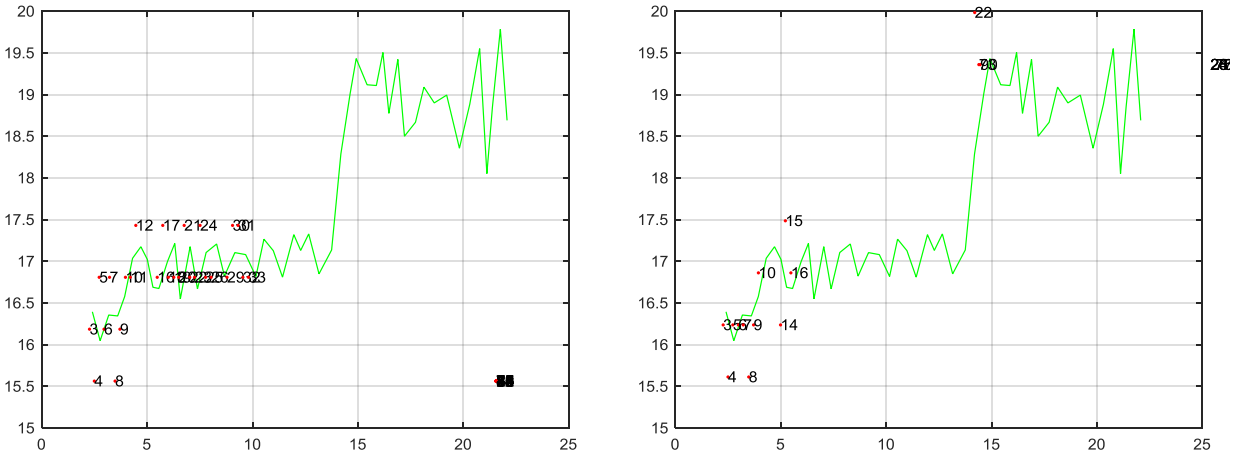

(a) (b)

Figure 64 Zoom over a cooperative target at near range for: (a) 482 MHz and (b) 650 MHz.
(x-axis: bistatic range [km] y-axis: bistatic velocity [m/a])

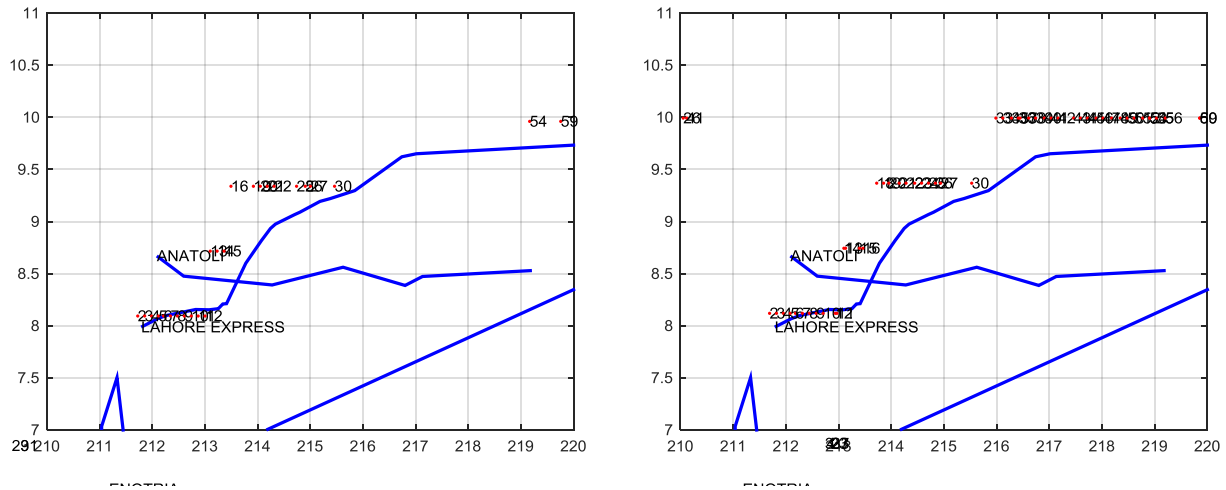

(a) (b)

Figure 65 Zoom over an opportunity target at far range for: (a) 482 MHz and (b) 650 MHz.
(x-axis: bistatic range [km] y-axis: bistatic velocity [m/a])

Centralized multi-frequency integration based on 'SUM' and 'MAX' approaches provide the results of Figure 66. Such approaches allow to maintain and possibly enhance detection continuity of the system, however they both grab on to the noisy detections of F2. To minimize the number of false alarm in the scene, more conservative approaches such as 'Min' or 'Decentralized 2-out-of-2' should be applied: results are those of Figure 67. Indeed, the number of false alarm drops drastically, however it catches the eye the lack of detections for the far range target as well as for those at about (130 km, -15 m/s) that were detected with good continuity from both F1 and F2.

At a closer inspection it resulted that each frequency provided detection of the same target at a different range, thus the integration did not end up in a performance improvement. This is clearly visible in Figure 68.

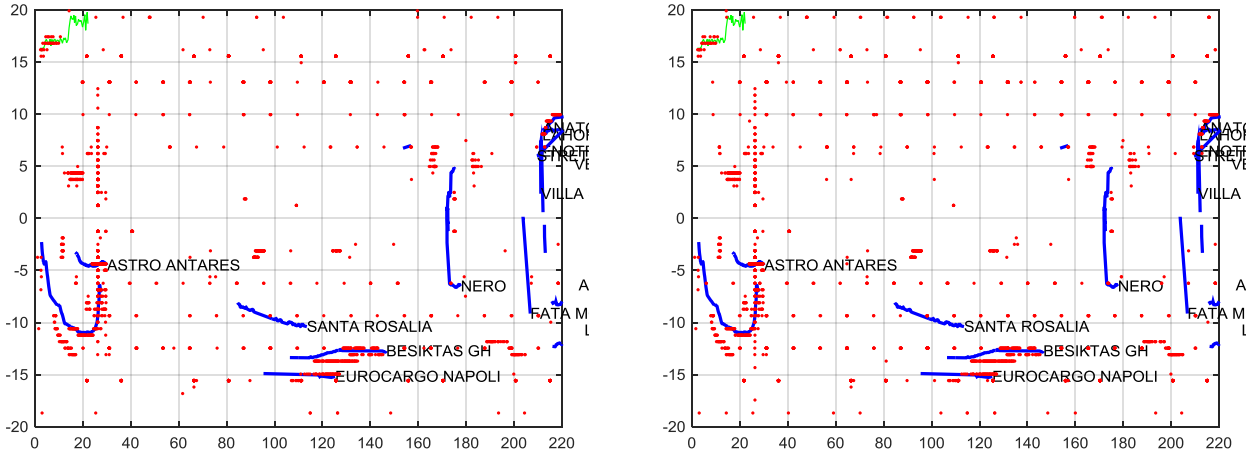

(a) (b)

Figure 66 Raw detections over 90 consecutive scans for multi-frequency integration via: (a) 'Sum' approach and (b) 'Max' approach. (x-axis: bistatic range [km] y-axis: bistatic velocity [m/a])

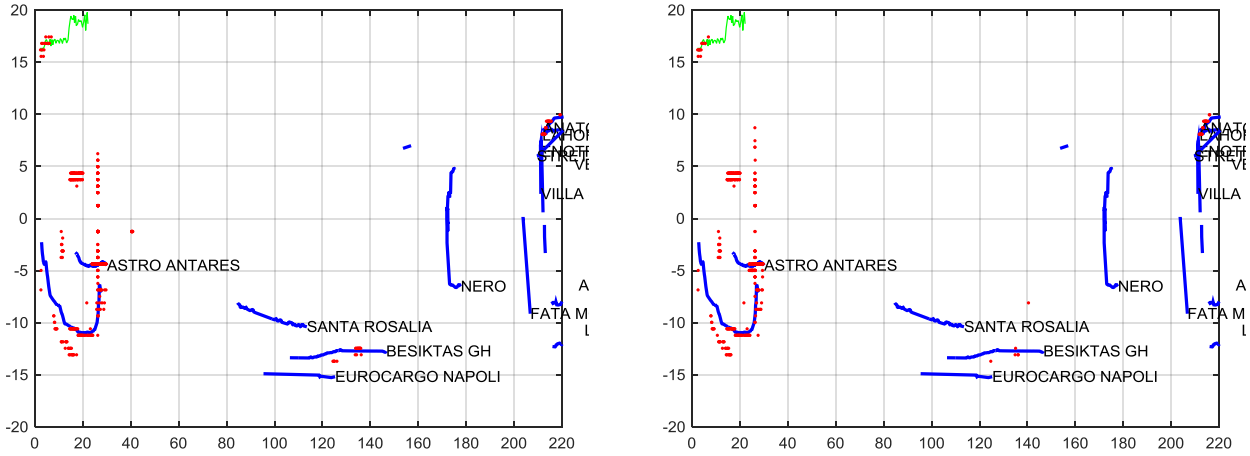

(a) (b)

Figure 67 Raw detections over 90 consecutive scans for multi-frequency integration via: (a) 'Min' approach and (b) 'Decentralized 2-out-of-2' approach. (x-axis: bistatic range [km] y-axis: bistatic velocity [m/a])

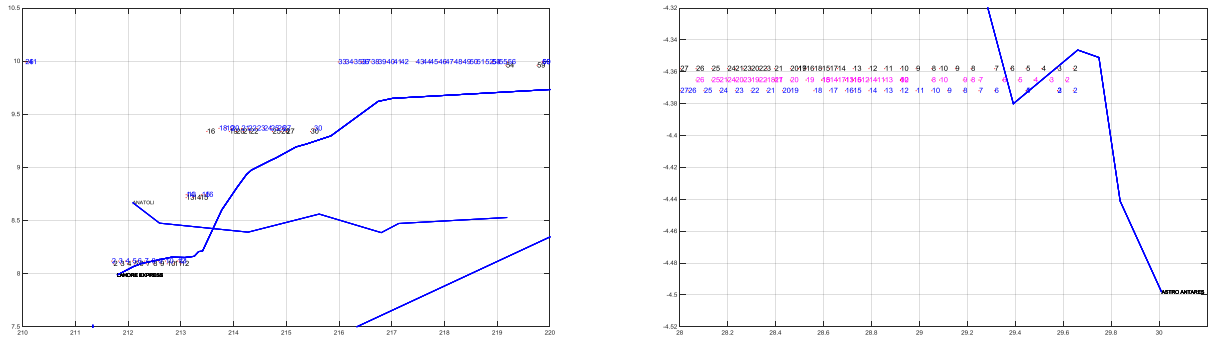

(a) (b)

Figure 68 Range detection misalignment. Black numbers represent scan index for detection with F1 while blue numbers refer to F2. Magenta numbers represent detection of a third acquired channel.
(x-axis: bistatic range [km] y-axis: bistatic velocity [m/a])

This behavior may be due to two factors:

- large targets, as those in the figures, may provide different responses at different frequencies. However this is not confirmed by the detections reported by magenta numbers in Figure 68 as they refer to the frequency channel at 490 MHz which is quite close to channel F1 (at 482 MHz);
- considered channels are broadcasted from the same transmitter site, however they may be transmitted from different masts which distance may differ of several tens of meters. In such case the misalignment depends on the target position with respect to the line joining the transmitters and it cannot be aligned if transmission masts position is known.

Under this conditions, centralized integration criteria (i.e. those summing the RDM of each frequency prior to perform CFAR detection) cannot be used. It is necessary to find a way to cope with this problem using decentralized integration criterion.

This is clear by analyzing CFAR outputs at scan #54 for each frequency on each of the two surveillance channels. As is clear from the left and center panels of Figure 69 a strong target is detected at about 135 bistatic kilometers. However applying the '2-out-of-2' criterion on the frequencies for each surveillance channel give rise to just a single confirmed detection for the first surveillance antenna (right panel of Figure 69(a)). When the surveillance channel are integrated with another '2-out-of-2' criterion, no detection is obtained at the end of the process even though the region of detections appeared to be quite large for each single CFAR output.

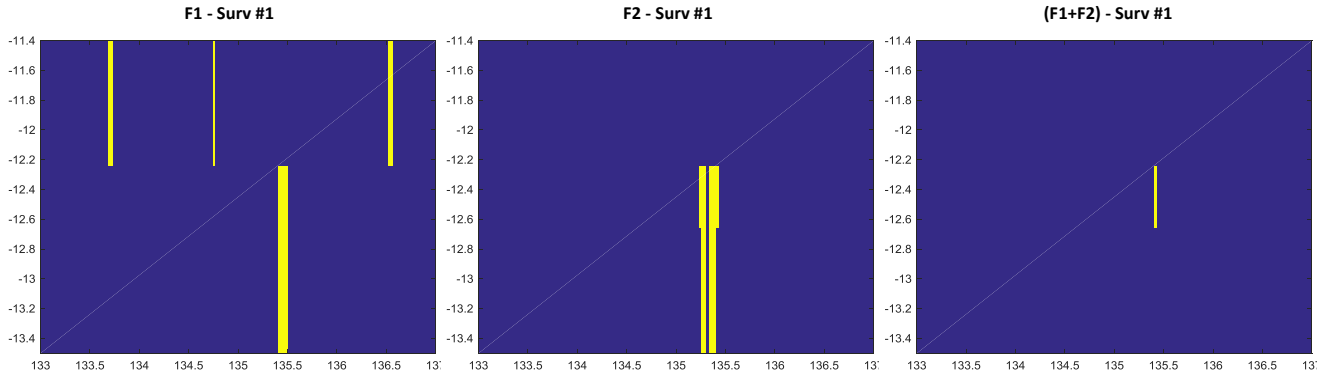

(a)

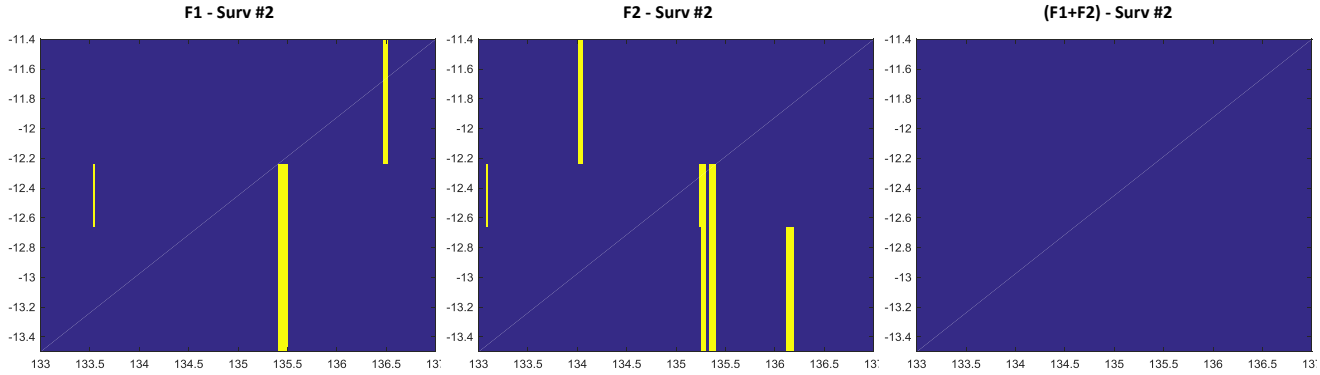

(b)

Figure 69 CFAR outputs from left to right: F1, F2, integration F1+F2 via '2-out-of-2' decentralized approach for: (a) Surv #1, (b) Surv #2. (x-axis: bistatic range [km] y-axis: bistatic velocity [m/a])

Proposed quick fix relies on degrading the resolution of each CFAR output prior to perform the integration of the detection. With this remedy the output of the '2-out-of-2' integration criterion among surveillance channel would result in a confirmed detection as is clearly imaginable looking Figure 70.

Appling this remedy to the whole scans of the acquisition one would obtain the results of Figure 71. As can be seen detections of targets at about (130 km, -15 m/s) are now visible again.

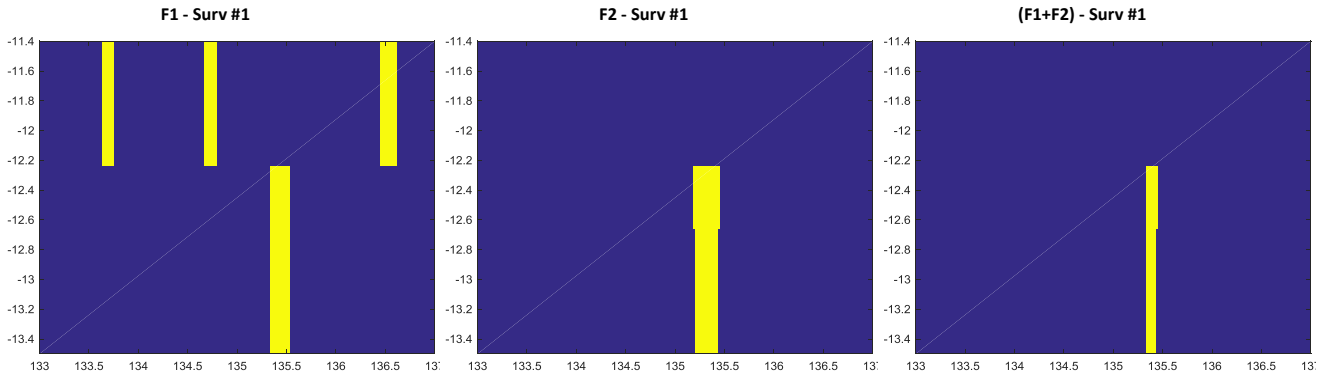

(a)

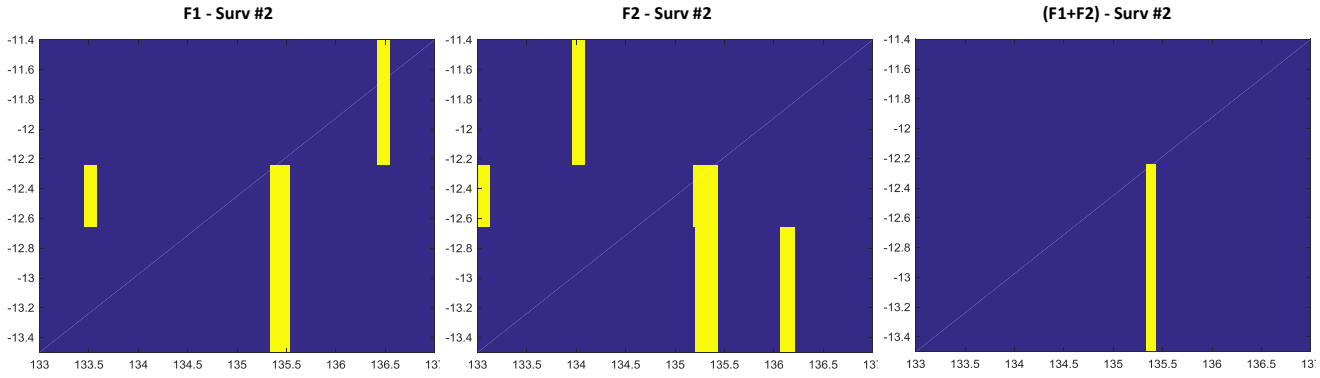

(b)

Figure 70 CFAR outputs with resolution degradation from left to right: F1, F2, integration F1+F2 via '2-out-of-2' decentralized approach for: (a) Surv #1, (b) Surv #2. (x-axis: bistatic range [km] y-axis: bistatic velocity [m/a])

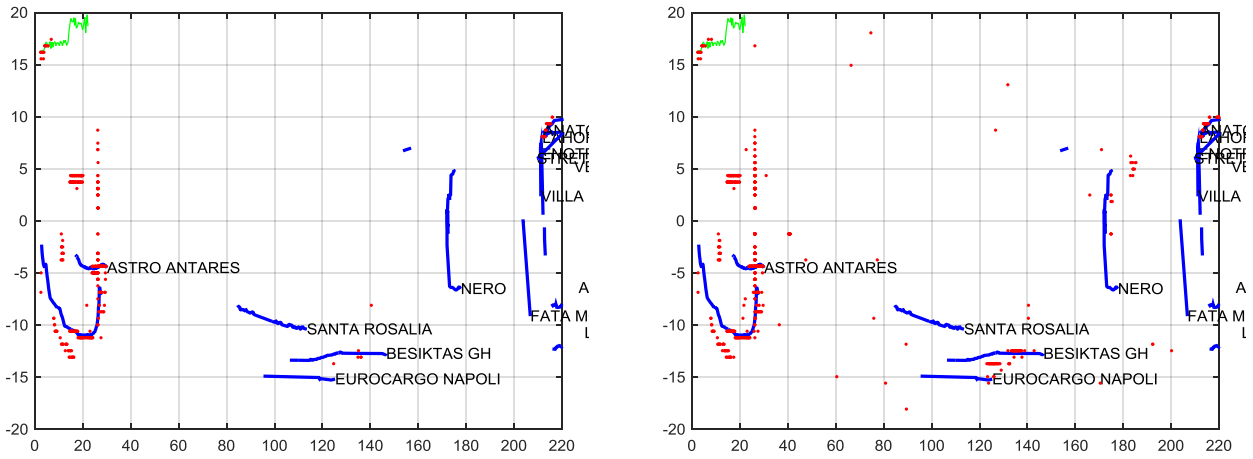

(a) (b)

Figure 71 Raw detections over 90 consecutive scans with 'Decentralized 2-out-of-2' approach: (a) without resolution degradation (b) degrading the resolution. (x-axis: bistatic range [km] y-axis: bistatic velocity [m/a])

3.7.4 CONCLUSIONS

It has been seen that many of the approaches for multi-frequency integration described in [27] cannot be directly applied in the processing chain of a DVB-T based passive radar. In fact, there is a misalignment in the range dimension between detections of the same target with DVB-T channels broadcasted from the same transmission sites. This has been attributed to the possible event of DVB-T channels transmitters located on different masts which may be located at tens of meters from each other.

A quick fix has been found for decentralized multi-frequency integration approach; it practically consists in degrading the resolution of each CFAR output prior to perform the integration among different frequency channels. This allows to hook detections of the same target that occurred on slightly different range bins.

It is worth noticing that the degradation of resolution may increase the probability of false alarm because it essentially consists in increasing the number of point of the RDM exceeding the CFAR threshold. This aspect needs special care when setting the threshold of the CFAR.

3.8 GPU CODE IMPLEMENTATION

In order to enable the quasi-real-time operation of the system, implementation of the most demanding algorithms blocks on GPU has been considered. In this section some words are spent on the advantages provided by such code implementation; the final version of the processing code has resulted in two different versions: an implementation on the CPU and an hybrid CPU/GPU version. The former was mainly used to perform analysis when a GPU equipped calculator was not available, while the latter was used in all the other cases including tests performed in some sites along the Italian coastline. At the end of this section a comparison of the execution times between the two implementation is also provided in order to verify the great improvement obtained.

3.8.1 GPU COMPUTING

GPU computing consists in using a graphics processing unit (GPU) together with CPU to accelerate engineering applications. A simple way to understand the difference between a CPU and a GPU is to compare how they process tasks, [61]. A CPU consists of a few cores optimized for sequential serial processing while a GPU has a massively parallel architecture consisting of thousands of smaller, more efficient cores designed for handling multiple tasks simultaneously (see Figure 72(a)).

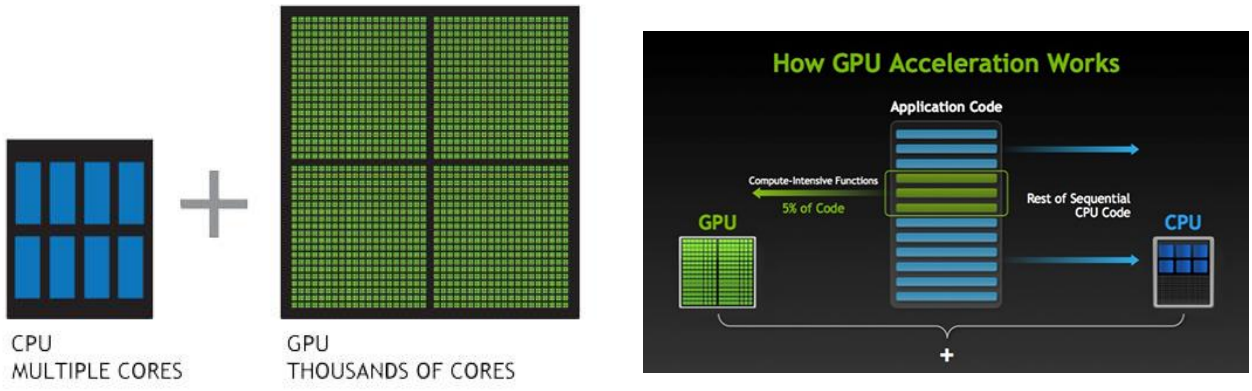

(a) (b)

Figure 72 (a) Comparison between CPU and GPU, (b) Example of code running on both CPU and GPU.

Based on this brief description the best way to run faster a code is to make work together a CPU and a GPU, as depicted in Figure 72(b). In particular, the sequential part of the application is demanded to the CPU, while the more demanding one is executed on the GPU.

NVIDIA created a parallel computing platform and programming model that goes under the name of CUDA. Operations to be performed prior and after the execution of the code are: (i) data transfer from CPU's DRAM to GPU's DRAM, (ii) GPU 'education' by the CPU unit via CUDA for code execution, (iii) parallel execution of the code and (iv) output transfer from GPU to CPU.

It is worth noticing that despite the faster execution of code on GPUs, data transfers, from and to the CPU, introduce latencies that may limit the overall execution time of the application; thus a careful attention should be devoted to design of the code and data transfers.

An alternative to CUDA programming is provided by Mathworks that starting from the MATLAB version R2010b supports the usage of GPUs by means of the Parallel Computing Toolbox package. MATLAB supports CUDA technology whether the used GPU has a computing capability greater than 1.3. It is also possible to exploit other tools – such as

GPUmat or Jacket – that allow to utilize a GPU as an external special purpose device through appropriate commands and constructs.

3.8.2 EFFECTS ON THE EXECUTION TIME

In Table 26, the execution time for each of the blocks described in the previous sections is reported. The two developed version of the code are compared: CPU-only version and a hybrid CPU/GPU version. Functions tagged with an asterisk shall be executed for each surveillance channel; reported time refers to the execution time of a single surveillance channel. Thus for those functions, exploiting two surveillance channels, one needs about twice the time.

Table 26 Execution time comparison between CPU-only and CPU/GPU versions of the code.

	CPU [s]	CPU/GPU [s]
PE	0,37	0,16
RPR	4,49	0,50
*ECA	3,44	0,97
*RDM optimum	67,45	5,05
*RDM sub-optimum	3,45	0,29
*CFAR	1,45	0,19
PLOTS EXTRACTION	0,11	0,04

It can be noted the huge computational load saving obtained for the most demanding functions of the processing chain. This definitely enables the quasi real-time capability of the system, meaning that aa sufficiently rapid update of the maritime traffic can be provided.

4 DAB BASED PBR

4.1 INTRODUCTION

In this chapter the experimental prototype of a DAB based PBR system for aerial surveillance is presented. The system has been developed and fielded at DIET Department. As already mentioned in 2.3.1, DAB transmissions are still in an experimental stage in Italy; unfortunately, this had an unfavorable impact on the research activity, as the uncertainties around the transmitters did not allow to fully exploit this waveform of opportunity. However, this activity has given an insight on the potentialities of DAB signal for surveillance purposes and can be a push to resume the research activity as soon as the signal transmission will be regulated and information about transmitting sites will be available.

The chapter is organized as follows. The state of the art regarding exploitation of DAB signals is treated in 4.2; in 4.3 it is presented the DAB signal simulator that has been implemented prior to perform acquisitions of the real signal. This activity allowed to look for similarity with DVB-T transmission, as OFDM modulation reckons on the insertion of fixed patterns in the signal to be transmitted that may infer with target detection. Section 4.4 provides some details on the receiver architecture; finally the acquisition campaigns and the obtained results are presented in 4.5. Conclusions are drawn in 4.6.

4.2 STATE OF THE ART

The progressive transition to digital broadcasting has increased the interest of the research community to exploit such kind of signal for surveillance applications.

In [19] a DAB based PBR was exploited for aerial surveillance. The system shows the potentialities of DAB signal; however, it was unable to show a consistent sequence of observations that could be interpreted as radar tracks.

In [22] performance of a DAB based PBR are investigated exploiting a SFN channel. In order to face the direct signal interference coming from all the transmitters broadcasting the channel of interest, authors recurred to analog beamforming to cause nulls in the direction of the illuminators. Additional robustness against the interference is obtained cross-polarizing the surveillance antennas; even though this process slightly decreases target return, the achieved reduction of the interference is said to be much greater. Finally, in the digital domain the reference channels are properly combined to further lower the interference. Experimental results showed that aerial targets could be detected at up to 30 km from the receiver for an acquisition length of 4 seconds.

In [60] the interference issue is addressed by not using any reference antenna and performing the evaluation of the range Doppler map by cross-correlating the surveillance signal with a reconstructed reference signal. Such approach has the nice property of not being dependent on the location of the transmitters; in fact, approaches described earlier may fail when receiver antenna cannot adequately isolate contributions from two or more transmitters thus impeding conventional interference suppression.

4.3 DAB SIGNAL GENERATOR

Prior to evaluate the performance of such prototype, a DAB signal generator has been developed for analyzing the characteristics of the signal ambiguity function (AF).

AF is defined as the absolute value of the envelope of the output of a matched filter when the input to the filter is a Doppler-shifted version of the original signal, to which the filter was matched. Thus the origin of the AF represents the output when the input signal is returned from a point target at the nominal delay and Doppler shift for which the filter was matched.

As well-known it represents a useful mean to investigate the potential range and Doppler resolution achievable with the exploited waveform. In addition, it allows to evaluate the impact on the AF of the periodic structures introduced within the OFDM symbol for proper demodulation at the receiver site.

The block diagram of Figure 5 is duplicated for convenience in Figure 73; in addition information about the size of the words travelling in the channels is provided for all the transmission modes.

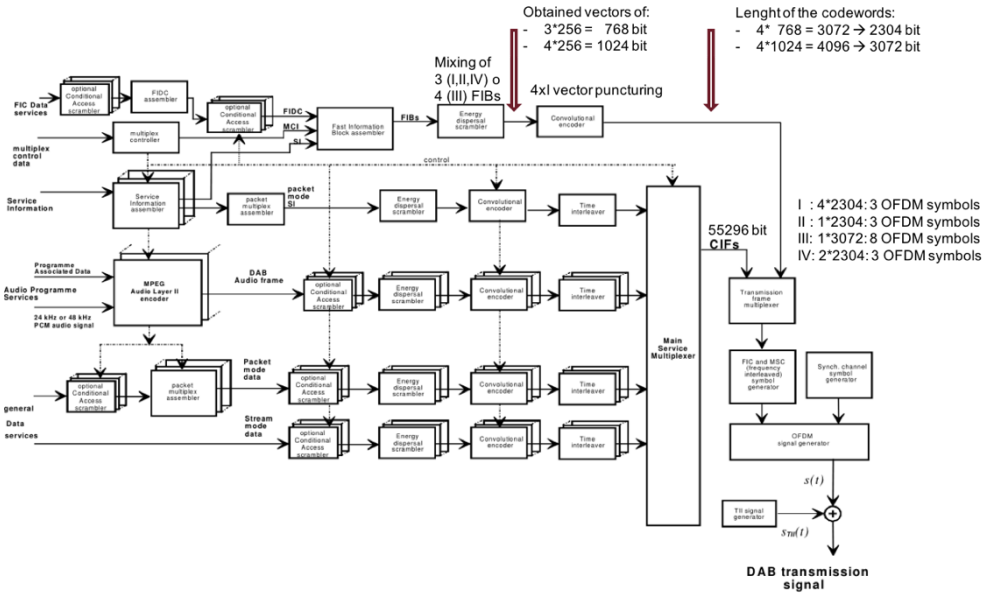

Figure 73 Block diagram of DAB signal generation. Size of the words travelling in the channels are provided for all the transmission modes.

Starting from the block diagram of Figure 73, a signal generator has been implemented in MATLAB. The transitions inside the time-interleaver and scrambler blocks cause the noise-like appearance in the DAB signal. For this reason, from a radar point of view, the block diagram can be synthesized as the one in Figure 75 where the output streams of FIC and MSC have been replaced by two random sequences of bits.

OFDM signal generator block of Figure 73 has been decomposed into smaller blocks to better highlight the crucial steps of the modulation. The only channel that cannot be simplified is the synchronization channel: it has a fixed pattern and is used for basic demodulator functions, such as transmission frame synchronization, automatic frequency control, channel state estimation and transmitter identification.

Synchronization channel consists of the first two OFDM symbols of each transmission frame. The first symbol is the null symbol, during the time interval $[0, T_{null}]$ the main signal shall be equal to 0. The second OFDM symbol is the phase reference symbol and constitutes the reference for the differential modulation for the next OFDM symbol. Differential modulation is obtained by multiplying each OFDM symbol to the previous one.

In [25] details about the generation of the reference symbol for each sub-carrier are provided. The differential modulation results in different constellations applied to even or odd symbols. Those are shown in Figure 74.

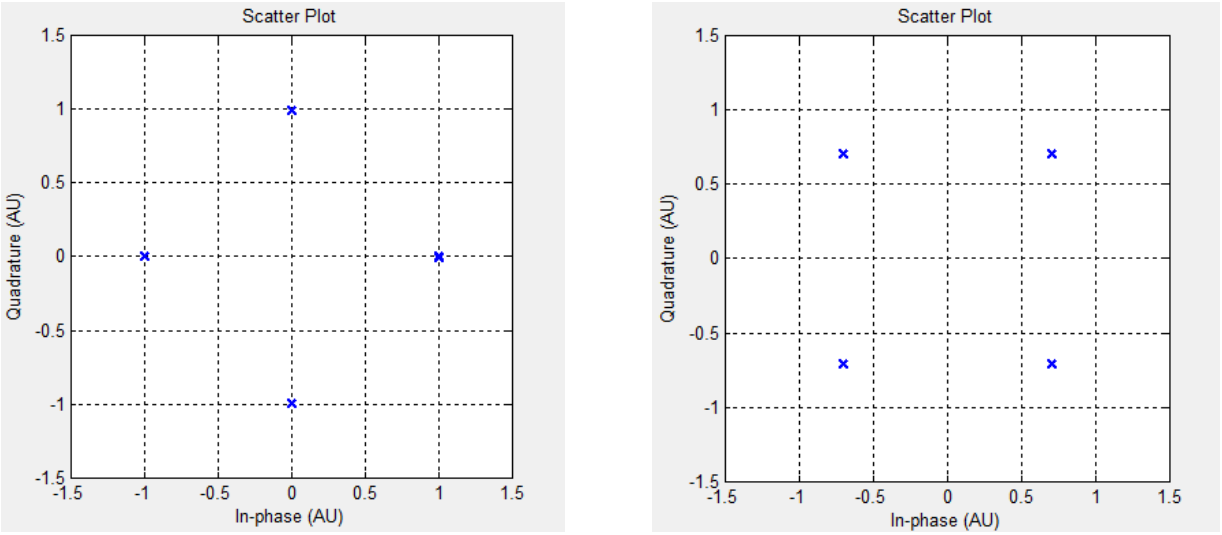

(a) (b)

Figure 74 (a) Even symbol constellation, (b) Odd symbol contellation.

The transmitted signal is built up around a transmission frame structure corresponding to the juxtaposition in time of the synchronization channel, the FIC and the MSC.

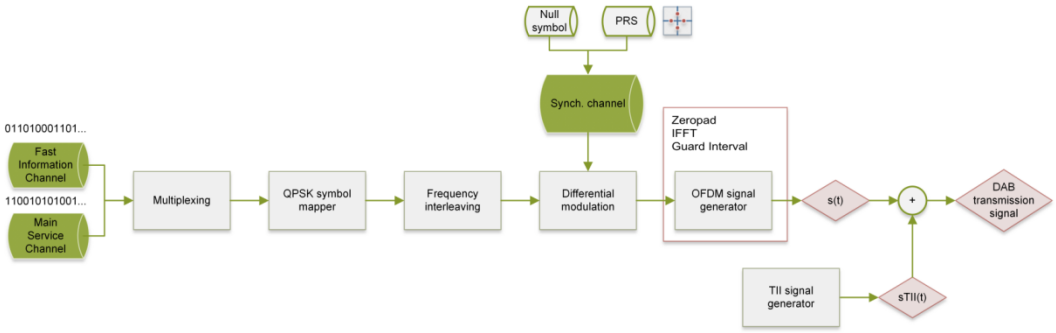

Figure 75 Simplified DAB emission block diagram.

Signals for each transmission modes have been simulated and cuts (delay and Doppler) of their ambiguity function are shown in Figure 76 and Figure 77. TM2 and TM3 simulated signals both show a sidelobe in the zero-delay cut: this is due to the usage of the guard interval which causes a high energy level in the signal autocorrelation when the delay is equal to the duration of the useful part of the symbol.

As the ratio of the number of guard samples to the number of the samples contained in an OFDM symbol is the same for each transmission mode, the amplitude of the undesired peak in the range dimension is expected to be the same. Due to their higher frame duration, TM1 and TM4 simulated signals would show such sidelobe at a delay which lies outside of the considered interval, however the sidelobes level would be the same of those of TM2 and TM3. In particular, has the guard interval for all the transmission modes is always 19,74% of the entire symbol duration, the energy level (SLL – sidelobe level) contained at the delay of the sidelobe is equal to:

$$\mathrm{SLL} = 20\log_{10}\left(\frac{T_g}{T_s}\right) = 20\log_{10}(0{,}1974) = -14{,}09\ \mathrm{dB}$$

and this is confirmed by the datatips in the figures below. The result can be mathematically verified operating on the parameters of Table 27.

Table 27 Parameters for transmission modes I, II, III and IV.

Parameter	Transmission mode I	Transmission mode II	Transmission mode III	Transmission mode IV
L	76	76	153	76
K	1536	384	192	768
T_F	196 608 T 96 ms	49 152 T 24 ms	49 152 T 24 ms	98 304 T 48 ms
T_{NULL}	2 656 T ~1,297 ms	664 T ~324 µs	345 T ~168 µs	1 328 T ~648 µs
T_S	2 552 T ~1,246 ms	638 T ~312 µs	319 T ~156 µs	1 276 T ~623 µs
T_u	2 048 T 1 ms	512 T 250 µs	256 T 125 µs	1 024 T 500 µs
Δ	504 T ~246 µs	126 T ~62 µs	63 T ~31 µs	252 T ~123 µs

On the other hand, the insertion of the null symbol at the beginning of each DAB frame is equivalent to the generation of a sampled-like spectrum which gives rise to high peaks in the Doppler domain. The periodicity of such peaks is related to the inverse of the frame duration, while their amplitude is given by:

$$\mathrm{SLL}_{\mathrm{null}} = 20\log_{10}\left(\frac{T_{\mathrm{Null}}}{T_F}\right)$$

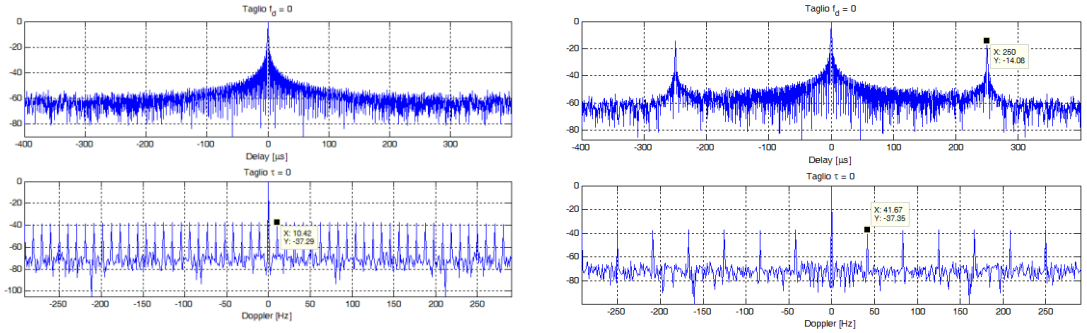

(a) (b)

Figure 76 Delay and Doppler cuts of the AF of DAB signal for the transmission mode: (a) TM1, (b) TM2.

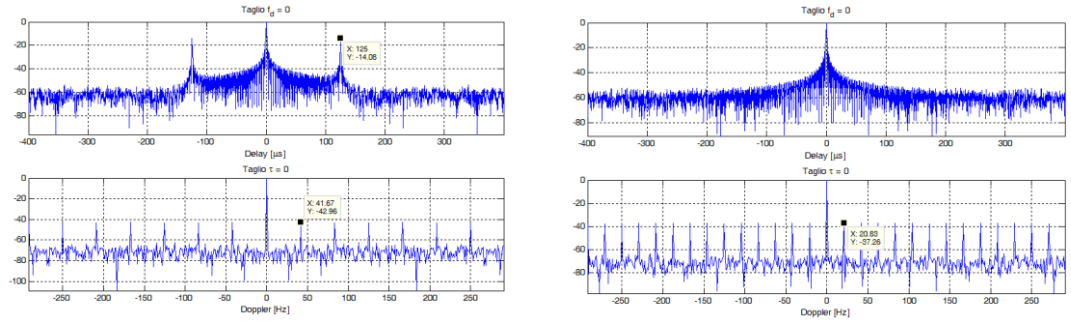

(a) (b)

Figure 77 Delay and Doppler cuts of the AF of DAB signal for the transmission mode: (a) TM3, (b) TM4.

A TM 1 DAB signal has been acquired and its cuts in the delay and Doppler dimension have been plotted and compared with those of the respective simulated data. Comparison shows the consistency of the developed signal generator, thus allowing its usage for further analysis.

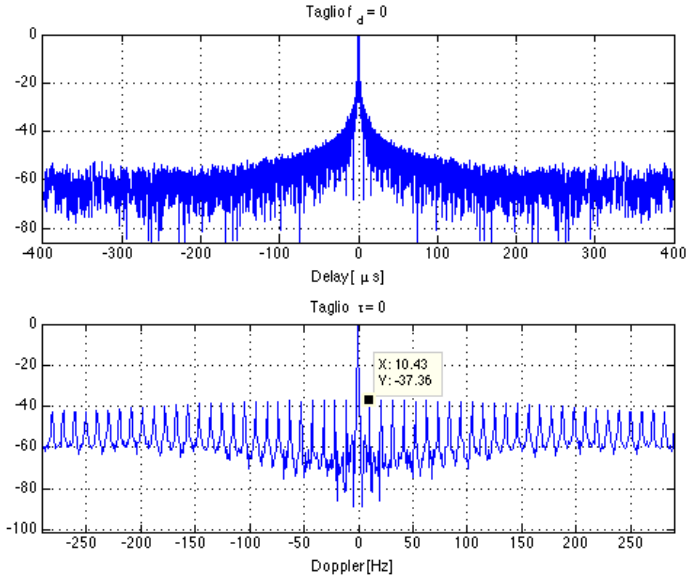

Figure 78 AF cuts of an acquired TM1 DAB signal.

4.4 RECEIVER ARCHITECTURE

As the prototype has been entirely developed by our research group a more detailed description of the receiver architecture can be provided with respect to the DVB-T based system.

During my research activity I was involved in configuring the acquisition board in order to make it capable of making long enough acquisitions for both surveillance and imaging applications. This work allowed our research group to carry activities focused on target recognition.

The receiver architecture of the prototype – fully made of commercial off-the-shelf (COTS) components – is depicted in Figure 79. The system is based on a direct RF (Radio Frequency) sampling approach, therefore, the tuning and the filtering is performed by digital signal processing.

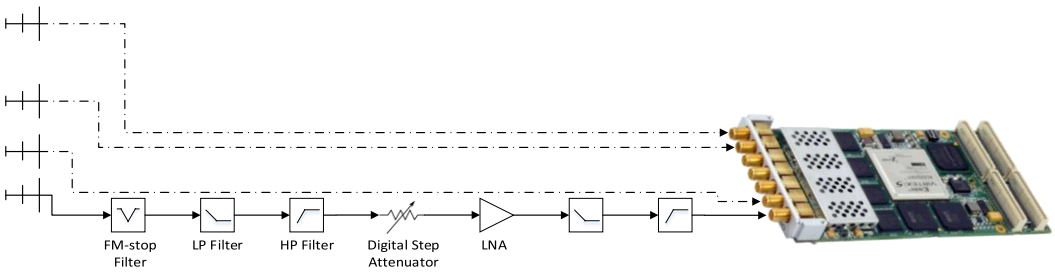

Figure 79 Experimental setup of the DAB-based PBR.

Log-periodic antennas with a front-to-back ratio greater than 16 dB and an azimuth plane beamwidth of about 64 degrees have been used to collected the reference and surveillance signals. Band filtering is performed recurring to an FM band-stop filter and a cascade of a low- and a high-pass filter to synthetize a pass-band filter around the frequency band of interest. Next, a cascade of adjustable attenuator and Low Noise Amplifier (LNA) to match the dynamic of the acquisition board's ADCs. Further filtering is performed at the output of the amplifier to reduce the amplitude of out-of-bound components.

The analogue front end is composed of the following components:

- **Band-stop filter ZBSF-95-N+ by Mini-Circuits**

It is a band-stop filter built into a rugged connectorized package offering a good rejection in the band 88 - 105 MHz. It is useful in Radio broadcast systems to minimize spurious signal and avoid system jamming. However in our application the utilization of such component was necessary in order to heavily reduce FM signals captured by the log-periodic antennas.

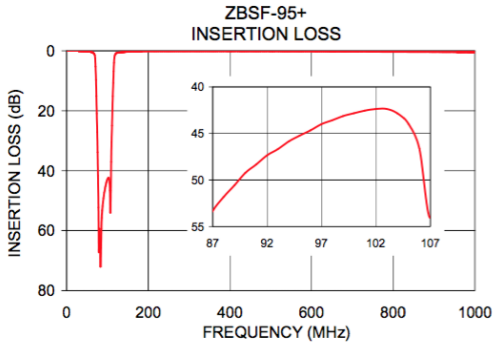

- **ZX75LP-264-S+ by Mini-Circuits**

ZX75LP-264-S+ is a 50 Ω low pass filter in a connectorized package. It covers DC-264 MHz bandwidth providing good matching within the passband and high rejection in stopband.

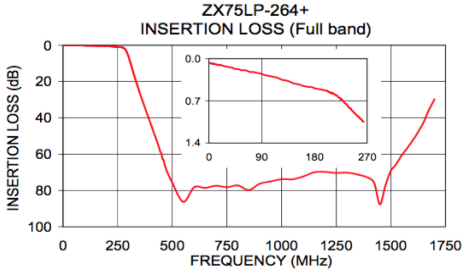

- **ZX75HP-110-S+ by Mini-Circuits**

ZX75HP-110-S+ is a high pass filter in a ruggered connectorized package covering 185 to 2500 MHz. This filter finds application in TV broadcast, point-to-point military radio and cordless telephones. It is characterized by low insertion loss and good rejection in the stopband.

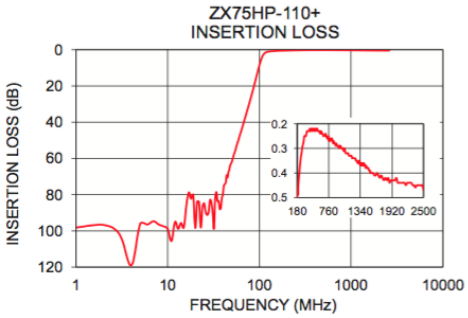

- **Variable attenuator ZX76-31R5-PN+ by Mini-Circuits**

ZX76-31R5-PN+ is a 50 Ω digital step attenuator that offers an attenuation range up to 31.5 dB in 0.5 dB steps. The control is a 6-bit parallel interface. The model operates on a single +3V supply.

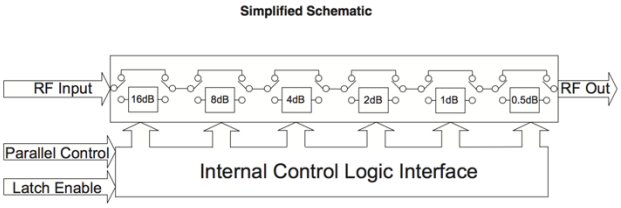

- **LNA ZHL-2010+ by Mini-Circuits**
- **LNA ZHL-1010+ by Mini-Circuits**

ZHL-2010+ and ZHL-1010+ by Mini-Circuits are wideband low noise amplifier (50 to 1000 MHz) providing 10 dB and 20 dB amplification, respectively.

- **ICS 1555 by GE Intelligent Platforms**

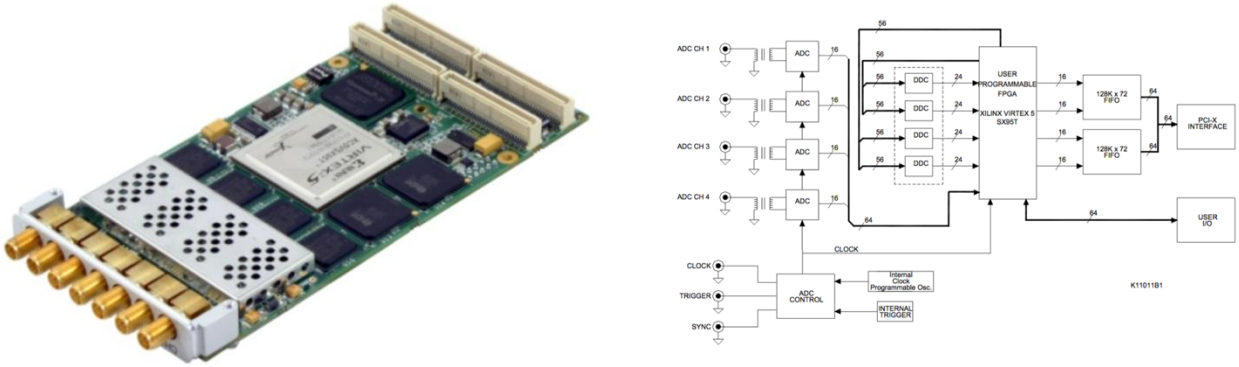

Figure 80 ICS1555 and its simplified block diagram.

The A/D conversion is performed via ICS-1555 PMC module, produced by GE Intelligent Platforms. The ICS-1555 is a four channel, 16-bit A/D module in a PMC format. The simplified block diagram of the ICS-1555 is presented in Figure 80 with four ADC, four DDC, a user programmable Virtex-5 FPGA, a 64-bit/133 MHz PCI-X interface and 64-bit User FPGA Pn4 I/O.

Four SMA coaxial connectors (marked CH1, CH2, CH3, and CH4) are provided on the front panel for connecting the single-ended analogue input signals. Three SMA coaxial connectors (marked CLK, TRIG and SYNC) are provided on the front panel for connecting the External Clock, Trigger and Synchronization.

The ICS 1555 supports two modes of operation. In continuous mode, data is converted on all selected channels and supplied to one of the two output interfaces until the acquisition is disabled. In capture mode, a fixed number of samples are acquired upon each application of the trigger. The number of samples acquired at each application of the trigger is programmable with a resolution of four samples per channel or less, up to the maximum capacity of the buffer. The programmable ADC output decimator can reduce the output data rate by a factor of up to thirty-two.

The acquisition board uses four 16-bit Linear Technology LTC2209 ADCs that sample synchronously at conversion rates up to 180 MSPS. The sampling clock can be generated internally using the on board Silicon Labs Si571, a modern Crystal oscillator with programmable frequency and a stability of ± 20 ppm or sourced externally by powering down the onboard oscillator and providing a clock input on the front panel connector. The external clock can be a sine wave or a LVTTL signal with a frequency in the range of 32 MHz to 180 MHz. All the data collected by means of this receiver have been performed using the on-board oscillator.

The ICS-1555 also provides programmable decimation of the ADC data stream by a factor of up to 256, making the effective minimum sampling rate 3.90625 KHz. Decimation is accomplished by storing 1 out of every N samples where N is programmable from 1 to 256. Note that no filtering is performed prior to decimation when the DDC is bypassed. The full-scale input signal level, which is software selectable, is 1.48 dBm (0.75 Vpp) or 5dBm (1.125 Vpp) into 50 Ω. The maximum safe input level of ICS-1555 is 3.9Vpp (+15.8 dBm) at 50 Ω termination. It applies to both full-scale input ranges (1.48 dBm or 5dBm). AC coupling is affected using transformers on the inputs to the converters.

The outputs of the ADCs are passed to the FPGA. The selection of whether data is taken from the ADCs, from the Graychip DDC outputs, or from the FPGA internal WB DDC outputs is made within the FPGA. When ADC output is selected, the data is presented as 2's complement (signed) 16-bit samples. When Graychip DDC output is selected, the standard FPGA firmware writes the DDC output data as 2's complement (signed) 24-bit samples. When FPGA internal WB DDC output is selected, the standard FPGA firmware writes the DDC output data as 2's complement (signed) 32-bit samples. The User FPGA output is buffered in two 128 K x 72 FIFO memories. PCI Bus interrupts are available for a

programmed threshold level and overflow conditions of the FIFOs as well as other conditions such as temperature alerts, ADC Overrange and more. The FIFO outputs are connected to the PCI-X interface.

Our acquisitions of DAB signals exploited Graychip GC4016 ASIC DDC chip, which contains four identical down-conversion circuits, giving up to 16 individual output channels. A block diagram of a single GC4016 device is shown in Figure 81.

The data inputs to each of the GC4016 chips consist of four independent 14-bit data buses or three independent 16-bit data buses routed from the User FPGA. Any of the input channels to the GC4016 chips may use any of the A/D input channels as its data source, or use digital data received from outside the card via the User I/O Pn4 interface. Each GC4016 output channel can be configured to select and down convert a signal band from the input data stream centred on a specific input frequency (the IF or carrier frequency).

Each of the four identical down-converters on the DDC chip accepts a real sample rate up to 100 MHz, down-converts a selected IF frequency to zero, filters the signal, decimates the signal rate by a programmable factor ranging from 32 to 16,384 and then optionally resamples the channel to adjust the sample rate up or down by an arbitrary factor.

A Numerically Controlled Oscillator (NCO) and mixer are used to quadrature down convert a signal from the tuning frequency to baseband. A positive tuning frequency is normally used to down convert the signal; however, a negative tuning frequency can be used to invert the output spectrum.

Each down converter channel contains three filters in sequence to low pass filter and isolate the down converted signal(s). Users have the option to download filter coefficient sets provided by GE Intelligent Platforms Ltd. with the software device drivers for the ICS-1555, or to use their own custom filter coefficients. The CIC filter decimates the inputs from the NCO by a factor of N, where N is from 8 to 4K, and has a gain equal to N5. The inputs have to be scaled before this filter to prevent overflow. This scaling is done in the shift down block. Coarse gain is set for each channel in the CFIR register (bits 4-6) and it can be used to boost the channel's gain by up to 42 dB. This is accomplished by shifting up the output of the CIC filter by 0 to 7 bits before rounding to 24 bits. The output of the coarse gain circuit is filtered in the CFIR filter stage. This stage is a 21-tap decimate by 2 filter with programmable 16-bit coefficients. Since this filter decimates by two, a stopband must be created in that portion of the spectrum that would alias into the signal of interest. The second stage decimate by two filter is a 63-tap decimate-by-2 filter with programmable 16-bit coefficients. Fine gain is applied at the output of the PFIR and rounded to 24 bits. The resampler will independently filter and change the data rate of each channel. The most common application of the resampler is to increase the sample rate of the data so that it will match a desired symbol or bit rate.

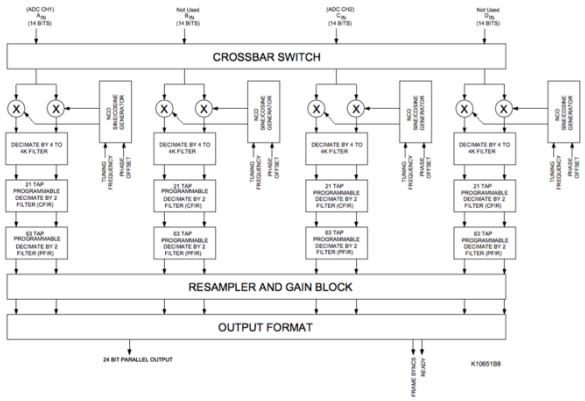

Figure 81 GC4016 Block Diagram.

The DDCs in the Graychips contain multichannel mode functionality. The maximum single channel output bandwidth is approximately 2.5 MHz. This output bandwidth can be doubled by combining two channels using the Split-I/Q mode.

Four channels may be combined to provide three to four times the single channel output bandwidth. Two channels can be combined to process complex input data, doubling the input bandwidth. Four channels can be combined to both process complex input data and to double the output bandwidth of the chip. Two or four multichannel modes may also be used in the complex to real mode. Table 28 gives a summary of the channel output formats for each GC4016 mode.

Table 28 DDC operating modes.

DDC Mode	Signal Bands Stored in FIFO Memory
Narrowband complex output	1,2,3,4,5,6,7,8
Narrowband real output	2,4,6,8
Split-I/Q complex output	2,4
Split-I/Q real output	2,4
Wideband complex output	1,2
Wideband real output	1,2
Narrowband pairs of complex input & complex output	2,4
Narrowband pairs of complex input & real output	2,4
Split-I/Q complex input & complex output	1,2
Split-I/Q complex input & real output	1,2

Some details are now provided about some of the different DDC module configurations.

16-Channel Narrow Band Configuration

Since each GC4016 chip contains four down converter paths, the ICS-1555 can be configured for up to 16 down converter channels in this mode. Each down converter channel has individual input selection, tuning frequency, tuning phase, CFIR coefficients, PFIR coefficients and gain settings. The decimation of each channel is from 32 to 16384 and CIC decimation factor is from 8 to 4096. The outputs are normally complex sample pairs. Double rate real output can also be generated by using complex to real conversion.

8-Channel Split-I/Q Configuration

Two channels work together in the Split-I/Q mode to double the output bandwidth of the Down converter. In the Split-I/Q mode, the real half of the complex output data is processed in one channel and the imaginary half in the other. The CIC has a minimum decimation of 4 instead of 8, which allows to double the sample rate of the output. The two channels being combined in the Split-I/Q mode should be programmed identically, including the tuning frequency, except that the imaginary channel should have a +90° phase shift. The decimation of each channel is from 16 to 8192 and CIC decimation factor is from 4 to 2048. Typically, the chip is configured in the Split-I/Q mode so that channels A and B are combined as one Down converter and C and D are combined as the other. Double rate real output can be generated by combining Split-I/Q and complex to real conversion. Note: in Split-I/Q and real output mode, the minimal CIC decimation factor is 5, while the minimal CIC decimation factor is 4 in Split-I/Q and complex output mode. The ICS-1555 provides up to 8 Split-I/Q down converter channels.

4-Channel Wideband Configuration

Even wider output bandwidth is possible than is available using the modes described previously, by combining all four channels of a DDC. This is done by noticing that PFIR decimates the signal by two. If one pair of channels in the Split-I/Q mode are used to generate even time sample outputs and the other pair are used to generate odd time sample outputs, then the PFIR filter effectively does not decimate the signal. This allows a wider bandwidth filter to be used in the CFIR and PFIR. Double rate real output can be generated by combining wideband and complex to real conversion. The decimation of each channel is from 8 to 4094 and CIC decimation factor is from 4 to 2048. Note: in wideband and

real output mode, the minimal CIC decimation factor is 5, while the minimal CIC decimation factor is 4 in wideband and complex output mode. The ICS-1555 provides up to 4 wideband down converter channels.

After having described the DAB based experimental setup Front-End, focus is now given to the choices made regarding sampling frequency used to digitize the signals of interest. This aspect is covered in the following section.

4.4.1 SELECTION OF THE SAMPLING FREQUENCY

The acquisition board is able to work with a maximum sampling frequency equal to 100 MSPS; thus, given the values of the DAB carrier frequencies, the 'undersampling' technique is adopted. It exploits the aliasing phenomenon to enable the ADC to sample DAB signal with a rate that intentionally aliases the modulated carrier into the operating range of the ADC.

To work properly, undersampling technique requires a careful sampling frequency selection and adequate filtering has to be performed before digitizing the signal. One of the easiest way to understand the principle behind this sampling technique is the 'fan-fold' paper method ([62]). Start with a small stack of semi-transparent fan-fold computer printer paper. Holding the papers with the folds in the vertical direction, the frequency axis should be plotted from left to right along the bottom edge with the inward creases at multiples of the ADC sampling frequency, f_s, and the outward creases at odd multiplies of $f_s/2$, as shown in Figure 82.

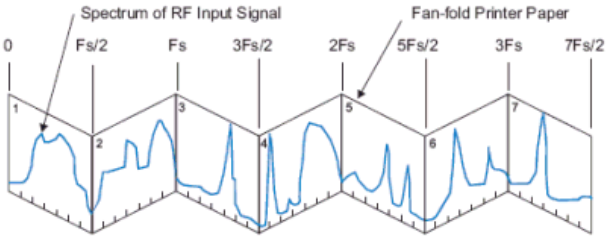

Figure 82 Fan-fold paper showing the spectrum of a RF signal.

The vertical axis is used to plot the spectral amplitude of the signal. In order to see what happens after sampling, simply collapse the stack of fanfold paper, hold it up to a light and look through the stack. Spectra from all sheets appear superimposed on top of each other, which represents the exact frequency content in the A/D output samples. As shown in Figure 83, signals on all of the sheets above $f_s/2$ are effectively "folded" down into sheet 1 between 0 Hz and $f_s/2$.

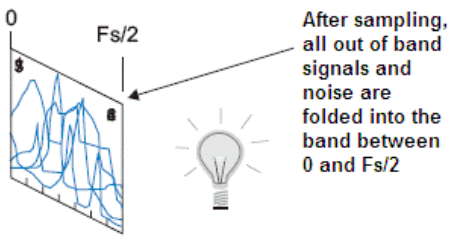

Figure 83 Looking through the collapsed stack reveals the resulting spectrum.

For the signals on every odd numbered sheet, the effect is a frequency translation by a multiple of f_s. For the signals on even numbered sheets, there is a reversal of the frequency axis on that sheet, followed by a translation by an odd multiple of $f_s/2$.

By adequately choosing the sampling frequency, one can exploit such approach for sampling bandpass signals. For example, if one is interested in sampling a signal whose spectral components are at frequencies comprised between $2 \cdot f_s$ and $5f_s/2$, after sampling all of the signal energy on sheet 5 will fold down onto sheet 1 (see Figure 84). The signal can be represented in the output sample stream as if it were a baseband signal between 0 and $f_s/2$. In this case the undersampling process results in a downward frequency translation by $2 \cdot f_s$ with no spectral reversal. If the bandpass spectrum of the input signal lied entirely on sheet 4 instead, the frequency axis would be reversed and then translated down by $3 \cdot f_s/2$.

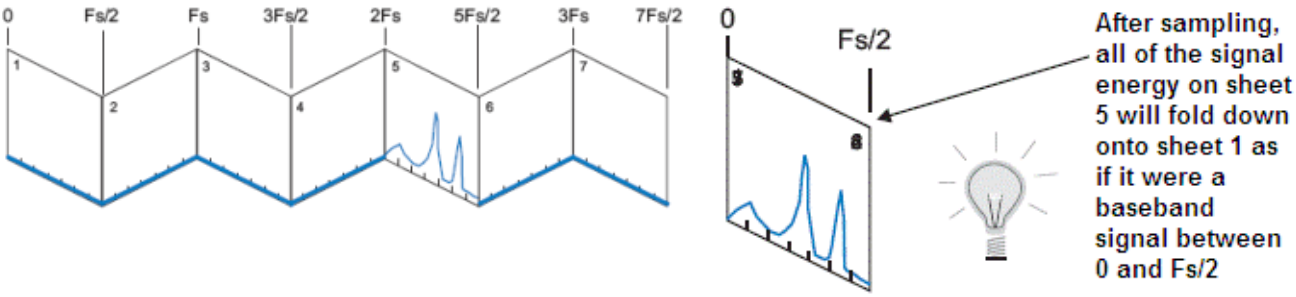

(a) (b)

Figure 84 (a) Bandpass signal of interest. (b) Translation of the bandpass signal down to baseband.

Thus in order to use undersampling, one should use f_s so that the entire band of the bandpass signal falls on a single sheet. Such approach has been used to digitize DAB signals.

Figure 85 shows the spectrum of the acquired signal after being passed through the analogue front end of Figure 79. As can be seen, despite band filtering, undesired components are still present in the spectrum; thus special care has to be taken when choosing the sampling frequency to avoid the folding of those undesired contributions on the signal components of interest.

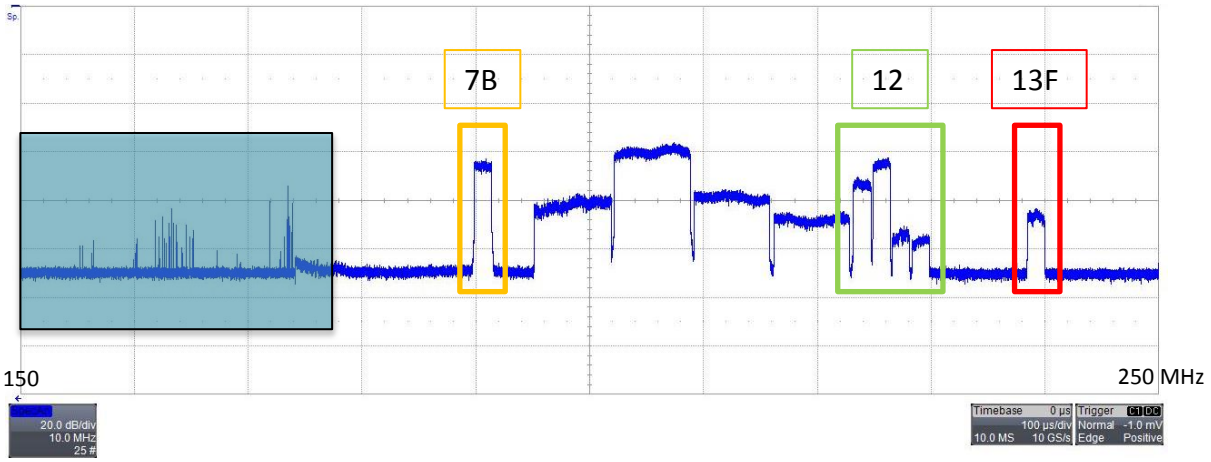

Figure 85 FM radio signal residuals after FM band filtering.

4.5 PRELIMINARY PERFORMANCE EVALUATION

4.5.1 ACQUISITION GEOMETRIES

During the research activity several acquisition campaigns with different geometries have been performed. Geometries are shown in Figure 86 where yellow and blue markers identify the alleged location of the transmitters of opportunity, blue straight lines stand for the pointing direction of the reference antenna and red straight lines indicate the pointing direction of the surveillance antennas. In both cases receiving antennas were located of the roof of the Faculty of Engineering in Rome.

In the acquisition geometry of Figure 86(a) the reference antenna was steered toward Città del Vaticano while the surveillance antenna was pointed at about 220° to collect the echoes from targets along their landing path for (or departing from) Fiumicino airport. Figure 86(b) shows the reference antenna pointed toward a transmitter located on Monte Cavo and the surveillance antenna steered toward Città del Vaticano.

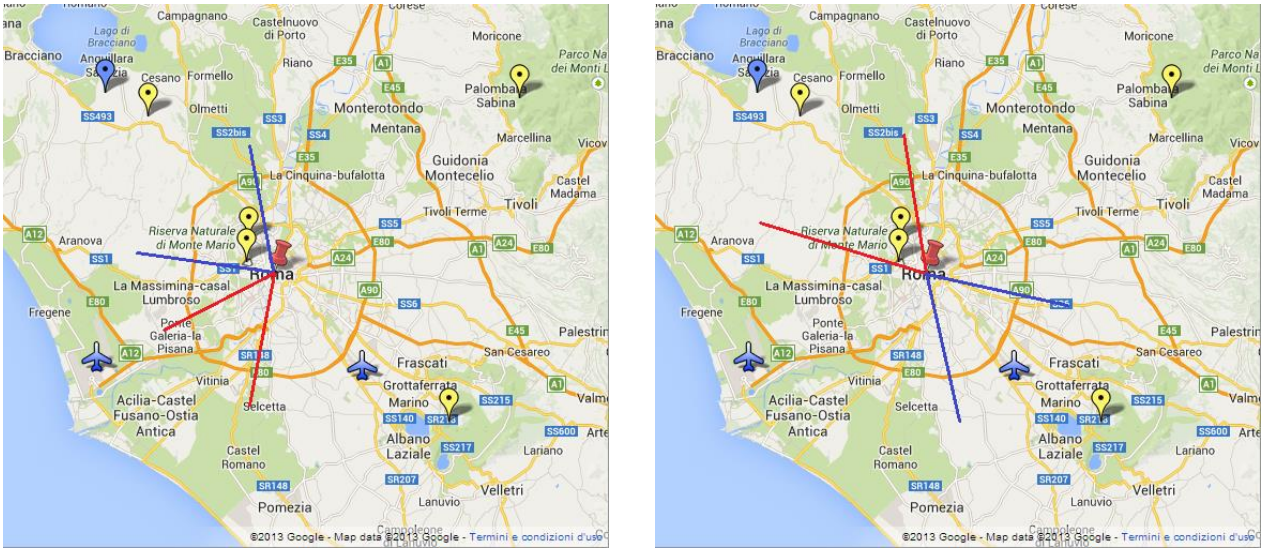

(a) (b)

Figure 86 Acquisition geometries.

4.5.2 ACQUISITION CAMPAIGNS

Acquired data has been treated with a conventional processing chain comprising: disturbance cancellation from surveillance channels via ECA-B, evaluation of the RDM recurring to the optimum efficient Correlation-FFT algorithm and target detection with a cell averaging – constant false alarm rate (CA-CFAR) with a nominal probability of false alarm rate equal to 10^{-4}.

4.5.2.1 ACQUISITION #1

This acquisition (about 400 seconds length) has been made with the geometry of Figure 86(a) for DAB channels 7B (190,64 MHz) and 13F (239,2 MHz). RDM is evaluated with a Coherent Processing Interval of 1 second.

Figure 87 shows RDM for channel 7B after tracking filtering. PBR detections are represented as red dots, while grayscale dots represent available air truth of the targets provided by ADSB (Automatic dependent surveillance –

broadcast) receiver. As can be seen the system presents good detection capability at up to 40 bistatic km; in addition, channel 7B is transmitted in a Single Frequency Network configuration, i.e. the same content is transmitted at the same time by transmitters covering overlapping regions. This is the reason why ADSB bistatic tracks have been reported with respect to two distinct transmitters. Since DAB signal is still under an experimental phase, there is no exact information regarding the position of the broadcast transmitters. For this reason it has been necessary to perform several trials prior to find the likely position of the transmitters and derive the bistatic ground truth tracks. For the considered acquisition, the estimated transmitters should be located somewhere near Città del Vaticano and nearby Ciampino airport.

When dealing with a SFN channel, a single target in the supervised area gives rise to more than one detection on the bistatic map. The position onto the map differ and is a function of the particular bistatic geometry between receiver, target and the particular transmitter. Our interest was to exploit SFN channels to perform target localization on the Cartesian plane only exploiting detections occurred with multiple transmitters. Unfortunately lack of information of real position of DAB transmitters did not allow to complete such task. Enough to think that no one of the receiver positions listed on the document for the DAB frequency allocation plane provided perfect alignment of the bistatic air truth tracks with the PBR detected tracks. In our mind it was reasonable to assume that the location of the test transmitters was quite near to the sites of DVB-T transmitters. For this reason, a list containing all the DVB-T transmitters (even the gap fillers) covering Roma's land was used to find the best alignment of the tracks on the bistatic plane.

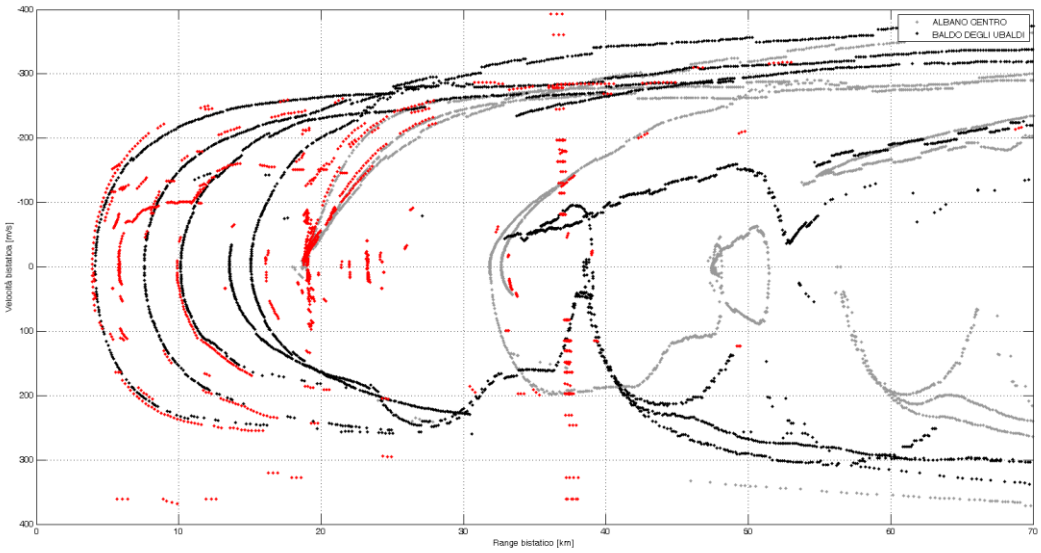

Figure 87 RDM for Acquisition #1 (190,64 MHz).

Figure 88 shows results for the same acquisition; however, the air truth has been now represented on the bistatic plane for two other transmitters. Even though there is a certain closeness between the real and the detected tracks, such discordance do not allow to localize the target via triangulation.

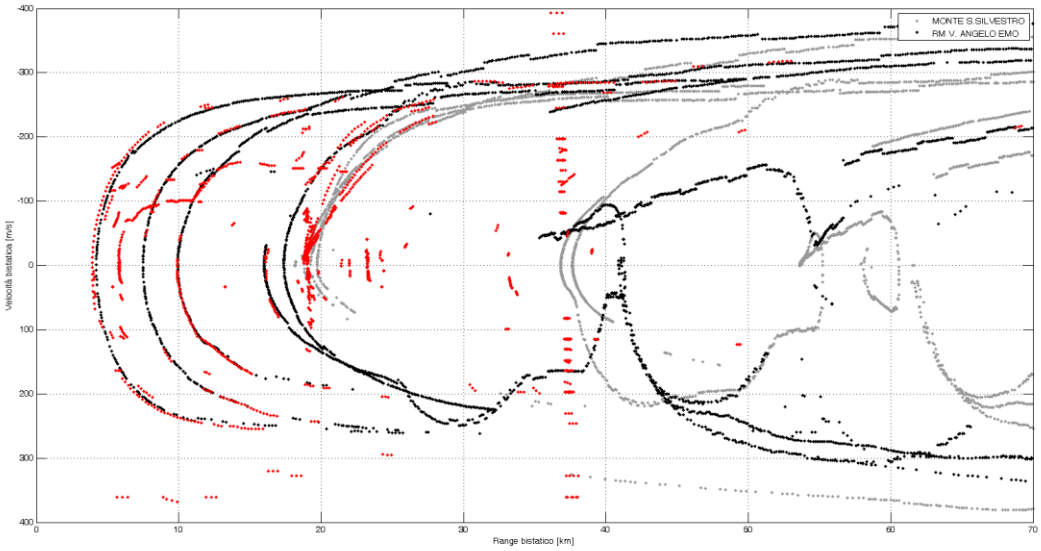

Figure 88 RDM for Acquisition #1 (190,64 MHz).

Regarding channel 13F, results are those reported in Figure 89. In this case only one transmitter – located on Monte Gennaro – broadcasts the signal; a much cleaner map is obtained with a maximum coverage of about 25 km.

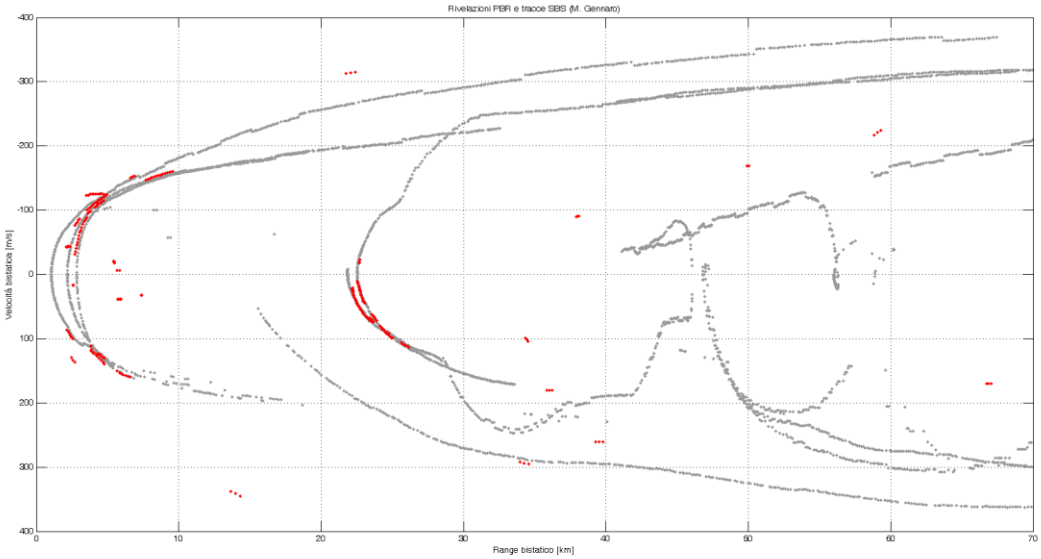

Figure 89 RDM for Acquisition #1 (239,2 MHz).

4.5.2.2 ACQUISITION #2

Same channels of Acquisition #1 have been captured with the geometry of Figure 86(b). Again, RDM is evaluated with a Coherent Processing Interval of 1 second. This time, two surveillance antennas were used with orthogonal polarization. It allowed to verify whether it was possible to enhance the performance of the system by making one of the surveillance antennas cross-polarized with respect to the transmitter (see Figure 90(a)).

Surveillance channels have been separately processed with the conventional chain described before; results are shown in Figure 90(b). For channel 13F, due to the remoteness of the transmitter from the receiving site, no evident performance improvement is obtained with the vertically polarized surveillance antenna; the only exception is the track at about (10 km, 150 m/s) which is better detected by the cross-polarized channel. This track as well as other tracks at about (17 km, 50 m/s) that are not associated with air truth tracks have been assumed to be detections of target not equipped with the transponder, even though no certainty exist on the non-SFN nature of the channel. However, it is important to note that for this acquisition, a coverage of over 80 bistatic kilometres was obtained.

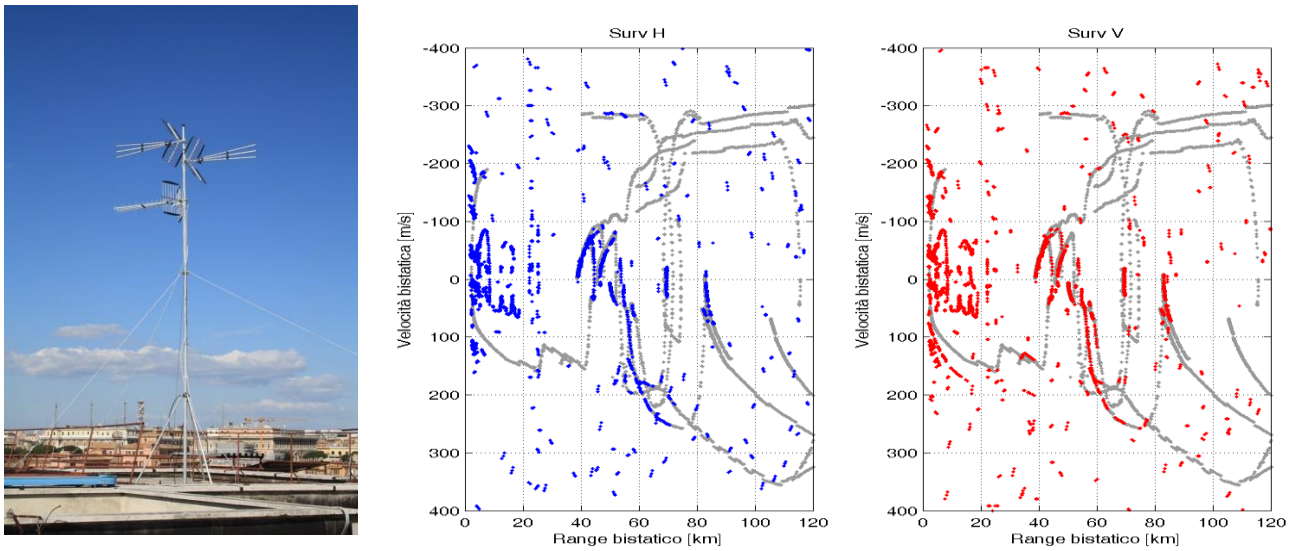

(a) (b)

Figure 90 (a) Antennas configuration for cross-polarized acquisitions. (b) RDM for Acquisition #1 (239,2 MHz) with two surveillance antennas

4.6 CONCLUSIONS

In this chapter an experimental setup for ATC applications based on DAB transmission has been presented. Results from several acquisition campaigns show the potentialities of the system in detecting aerial target at short and medium range. However, some limitations due to the SFN functionality have been faced; in particular, obtained Range-Doppler map presented many residues of interference from transmitters thus limiting the dynamic range of the receiver. In addition, the lack of information regarding the position of all the transmitters covering Roma land did not allow to properly associate each track (obtained in the Range-Doppler plane) to a transmitter. Thus SFN transmissions could not be used to perform target localization via triangulation.

Since this work has been conducted in the first part of the research activity, it did not benefit of novel processing technique used for DVB-T. In fact, due to the high similarity of the waveforms, technique for sidelobes control and for disturbance cancellation in highly non stationary scenarios could be applied. Thus it is plausible of obtaining much better results once the processing chain is properly modified.

Obtained results show however the goodness of the yet simple processing chain; in fact, very good detection continuity has been achieved for target flying at about 40 km from the receiver. These results, if compared with those of [19] and [22], further increase the ambitions of DAB based PBR systems for ATC applications.

5 CONCLUSIONS

In this thesis, two different PBR systems based on OFDM modulated signals have been presented. In particular, those were a DVB-T based PBR system for maritime surveillance and a DAB based experimental setup for ATC applications.

In Section 2, standards of transmission of both DVB-T and DAB have been described along with their main characteristics when used for radar purposes. It was shown that, with respect to FM radio that has been extensively used for long range surveillance applications), OFDM modulated signals provide much better range accuracy due to their higher bandwidth. Throughout the thesis also the range coverage provided by such waveforms turned to be much more than acceptable despite being transmitted with lower power than FM radio.

The signal processing chain developed for a DVB-T based PBR has been described in detail in Section 3. All the main issues highlighted in the introduction have been addressed. In particular, the main limitation of nowadays passive radars for maritime surveillance were:

(1) Disturbance cancellation in highly non stationary scenarios

A novel technique (ECA-S) for disturbance cancellation has been presented as existing ones may be inadequate when dealing with highly varying disturbance scenarios in presence of slowly moving targets or targets moving mainly along the cross-range direction. Exploiting several experimental data sets accounting for quite different PCL applications, ECA-S was demonstrated to provide a better trade-off between disturbance cancellation and the capability of preserving low Doppler target echoes thus improving the detection performance of the radar.

(2) Computational load reduction for real time detection capability

The huge amount of data to be processed hinders a constant update of the maritime traffic in the observed scene. As the system is required to work in real time, special care has been given to the implementation of all the algorithms in the processing chain. Efficient implementation of several techniques for disturbance cancellation has been addressed. It is based on the adoption of proper expedients for the calculation of the filter coefficients and their application to the surveillance signals allowing to contain the increase of the computational load required by ECA-S and making ECA and ECA-B approaches more attractive with respect to other existing techniques.

Evaluation of the RDM is another computationally extensive algorithm; thus proper selection of the technique to be implemented in the processing chain should be done. For the purpose comparison of several existing algorithms for RDM evaluation has been done in two practical demanding scenarios. Results have shown the need of reexamine the way an algorithm is used in a way that it provides a better trade-off between computational load and the SNR losses introduced to obtain cost saving.

All the algorithms of the processing chain have been implemented in MATLAB. Besides the efficient implementation of the algorithm, the high computational capability of GPU has been exploited to further lower the execution time of the code. The obtained computational load saving allowed to deal with a greater amount of data thus it was possible to start the investigation of multi-frequency integration approaches for system performance enhancement. Conducted analysis was carried on a reduced set of experimental data and, though it showed some potentialities, full exploitation of different frequency channels could not be achieved due to misalignment on the detections from each frequency channel.

(3) DoA estimation in a wide angular sector

Maritime surveillance as well as air traffic control application require, together with good target detection continuity, accurate estimation of the position in the Cartesian plane. Exploiting multiple receiving elements aligned in the

horizontal dimension allowed to perform DoA estimation for target localization. However the most important prerogative of a passive radar is the low cost of development; thus one cannot recur to substantially increase the number of receiving elements to enhance the estimation accuracy.

Conducted study had the objective of defining an array dimensioning strategy that allowed to obtain high accuracy estimates in a wide angular sector exploiting few receiving elements. This was allowed by the exploitation of baseline diversity in the dimensioning of the array. Once found the best array configuration, two approaches for DoA estimation have been presented and compared against simulated data. Finally, obtained results against experimental data sets have been presented.

In Section 4, an experimental setup of a DAB based PBR has been described. The characteristics of this waveform of opportunity have been initially studied after the MATLAB development of a signal generator. In particular, it was of interest the recognition of periodic structures in the signal ambiguity function due to the insertion of regular patterns from the OFDM modulation. Such structures may impede target detection if proper signal conditioning is not performed.

During the research activity, efforts have been spent on the assembly of the analogue front-end of the experimental setup; in addition, the acquisition board has been programmed to make very long acquisitions (order of tens of minutes for FM and DAB signals). This allowed other components of the research group to perform target imaging.

A simple data processing scheme has been applied to the experimental data set recorded in several acquisition campaigns and RDM have been produced. Detection performance has been evaluated by comparing the results with the detection of an ADSB receiver which collects returns emitted by the nearby airplanes. Results from several acquisition campaigns show the potentialities of the system in detecting aerial target at short and medium range. However, some limitations due to the SFN functionality have been faced; in particular, obtained RDM presented many residues of interference from transmitters thus limiting the dynamic range of the receiver. In addition, the lack of information regarding the position of all the transmitters covering Roma land did not allow to properly associate each track (obtained in the Range-Doppler plane) to a transmitter.

Obtained results show however the goodness of the yet simple processing chain; in fact, very good detection continuity has been achieved for target flying at about 40 km from the receiver. These results, if compared with those of [19] and [22], further increase the ambitions of DAB based PBR systems.

Since this work has been conducted in the first part of the research activity, it did not benefit of novel processing technique used for DVB-T. In fact, due to the high similarity of the waveforms, technique for sidelobes control and for disturbance cancellation in highly non stationary scenarios could be applied. Thus it is plausible of obtaining much better results once the processing chain is properly modified.

Concluding, this activity has given an insight on the potentialities of DAB signal for surveillance purposes and can be a push to resume the research activity as soon as the signal transmission will be regulated and information about transmitting sites will be available.

REFERENCES

[1] A. Farina and H. Kuschel, Special Issue on Passive Radar (Part I&II) – *IEEE Aerospace and Electronic Systems Magazine*, vol. 27, no. 10-11, 2012.

[2] P. Howland, Special Issue on Passive Radar Systems – *IEE Proceedings on Radar, Sonar and Navigation*, vol.152, no. 3, June 2005.

[3] A. Farina and M. Lesturgie, Special issue on Bistatic and MIMO radars and their applications in surveillance and remote sensing – *IET Radar, Sonar & Navigation*, vol. 8, no. 2, 2014.

[4] C. Bongioanni, F. Colone, P. Lombardo, "Performance Analysis of a Multi-Frequency FM Based Passive Bistatic Radar", 2008 IEEE Radar Conference, Rome, Italy, May 26-30, 2008.

[5] R. Saini, M. Cherniakov, V. Lenive, "Direct path interference suppression in bistatic system: DTV based radar", Proc. of the Int. Radar Conference 2003, pp. 309-314.

[6] C. Coleman, H. Yardley, "Passive bistatic radar based on target illuminations by digital audio broadcasting", IET Radar, Sonar & Navigation, 2008, Vol. 2, Issue 5 , pp. 366-375.

[7] R. Saini and M. Cherniakov, "DTV signal ambiguity function analysis for radar application", IEE Proceedings on Radar, Sonar and Navigation, Vol. 152, Issue 3, June 2005, pp. 133-142.

[8] C. Bongioanni, F. Colone, D. Langellotti, P. Lombardo, T. Bucciarelli, "A New Approach for DVB-T Cross-Ambiguity Function Evaluation", Proceedings of European Radar Conference (EURAD 2009), Rome, Italy, 30 September-2 October 2009.

[9] P.E. Howland, D. Maksimiuk, and G. Reitsma, "FM radio based bistatic radar," *IEE Proc. on Radar, Sonar and Navigation*, vol. 152, no. 3, June 2005.

[10] D. Poullin, "Passive detection using digital broadcasters (DAB, DVB) with COFDM modulation," *IEE Proc. on Radar, Sonar and Navigation*, vol. 152, no. 3, June 2005.

[11] Sun Hongbo, D. K P Tan, Lu Yilong and M. Lesturgie, "Applications of passive surveillance radar system using cell phone base station illuminators", IEEE Aerospace and Electronic Systems Magazine, vol. 25, no. 3, pp. 10-18, 2010

[12] R. Zemmari, M. Daun, M. Feldmann and U. Nickel, "Maritime surveillance with GSM passive radar: Detection and tracking of small agile targets", 2013 14th Int. Radar Symposium (IRS), pp. 245-251

[13] P. Krysik and K. Kulpa, "The use of a GSM-based passive radar for sea target detection", 2012 9th European Radar Conf. (EuRAD), pp. 142-145

[14] D. W. O'Hagan *et al*., "Passive Bistatic Radar (PBR) for harbour protection applications," *2012 IEEE Radar Conference*, Atlanta, GA, 2012, pp. 0446-0450.

[15] D. Langellotti, F. Colone, P. Lombardo, M. Sedehi and E. Tilli, "DVB-T based Passive Bistatic Radar for maritime surveillance," *2014 IEEE Radar Conference*, Cincinnati, OH, 2014, pp. 1197-1202.

[16] D. Langellotti, F. Colone, P. Lombardo, E. Tilli, M. Sedehi and A. Farina, "Over the horizon maritime surveillance capability of DVB-T based Passive Radar," *European Radar Conference (EuRAD), 2014 11th*, Rome, 2014, pp. 509-512.

[17] F. Colone, C. Bongioanni, and P. Lombardo, "Multi-Frequency Integration in FM Radio Based Passive Bistatic Radar. Part I: Target Detection," *IEEE Aerospace and Electronic Systems Magazine*, vol. 28, no. 4, 2013.

[18] F. Colone and P. Lombardo, "Polarimetric passive coherent location," in *IEEE Transactions on Aerospace and Electronic Systems*, vol. 51, no. 2, pp. 1079-1097, April 2015.

[19] D. Poullin, "Passive detection using digital broadcasters (DAB, DVB) with COFDM modulation," in *IEE Proceedings - Radar, Sonar and Navigation*, vol. 152, no. 3, pp. 143-152, 3 June 2005.

[20] D. Poullin and M. Flecheux, "Recent progress in Passive Coherent Location (PCL) concepts and technique in France using DAB or FM broadcasters," *2008 IEEE Radar Conference*, Rome, 2008, pp. 1-5.

[21] C. J. Coleman, R. A. Watson and H. Yardley, "A practical bistatic passive radar system for use with DAB and DRM illuminators," *2008 IEEE Radar Conference*, Rome, 2008, pp. 1-6.

[22] C. Coleman and H. Yardley, "DAB based passive radar: Performance calculations and trials," *2008 International Conference on Radar*, Adelaide, SA, 2008, pp. 691-694.

[23] http://rfmw.em.keysight.com/wireless/helpfiles/89600b/webhelp/subsystems/wlan-ofdm/Content/ofdm_basicprinciplesoverview.htm

[24] European Telecommunications Standard Institute, "Digital Video Broadcasting (DVB); framing structure, channel coding and modulation for Digital Terrestrial Television", 2009

[25] European Broadcasting Union, "Radio Broadcasting Systems; Digital Audio Broadcasting (DAB) to mobile, portable and fixed receivers", 2006

[26] H. D. Griffiths and C. J. Baker, "Measurement and analysis of ambiguity functions of passive radar transmissions," *IEEE International Radar Conference, 2005.*, 2005, pp. 321-325.

[27] P. Lombardo and F. Colone, "Advanced processing methods for passive bistatic radar systems," in *Principles of Modern Radar: Advanced Radar Techniques*, W. L. Melvin, and J. A. Scheer, Raleigh, NC: SciTech Publishing, 2012.

[28] F. Colone, D. Langellotti, and P. Lombardo, "DVB-T signal ambiguity function control for passive radars," *IEEE Trans. on Aerospace and Electronic Systems*, vol.50, no.1, Jan. 2014.

[29] C. Zhou, J. D. Sahr, M. G. Meyer, and D. M. Gidner, "Ground clutter subtraction algorithm for VHF passive radar observation of the upper atmosphere," URSI 2002, Maastrict, Aug. 2002.

[30] A. Guner, M.A. Temple, and R.J. Claypoole, Jr., "Direct-path filtering of DAB waveform from PCL receiver target channel," *Electronic Letters*, vol. 39, no. 1, 2003.

[31] S.R.J. Axelsson, "Improved clutter suppression in random noise radar," URSI 2005 Commission F Symposium on Microwave Remote Sensing of the Earth, Oceans, Ice, and Atmosphere, April 2005.

[32] K. Kulpa and Z. Czekala, "Masking effect and its removal in PCL radar," *IEE Proc. on Radar, Sonar and Navigation*, vol. 152, no. 3, June 2005.

[33] D.W. O'Hagan, C.J. Baker, and H.D. Griffiths, "Signal and Interference Analysis: Proposed Analogue Signal Suppression Techniques for PCL Radar," *3rd European Radar Conference, EuRAD 2006*, Sept. 2006.

[34] Wan Hong, Li Shentang, and Wang Zhigang, "Direct Path Interference Cancellation in FM Radio-Based Passive Radar," *8th Int. Conf. on Signal Processing*, vol.1, 2006.

[35] R. Cardinali, F. Colone, C. Ferretti, and P. Lombardo, "Comparison of clutter and multipath cancellation techniques for passive radar," *IEEE Radar Conference 2007*, Boston, Massachusetts, USA, April 2007.

[36] F. Colone, D. W. O'Hagan, P. Lombardo, and C. J. Baker, "A multistage processing algorithm for disturbance removal and target detection in Passive Bistatic Radar," *IEEE Transactions on Aerospace and Electronic Systems*, vol. 45, no. 2, April 2009.

[37] J.E. Palmer and S.J. Searle, "Evaluation of adaptive filter algorithms for clutter cancellation in Passive Bistatic Radar," *IEEE Radar Conference 2012*, Atlanta, May 2012.

[38] M. Meller, "Processing of noise radar waveforms using block least mean squares algorithm," *IEEE Trans. Aerosp. Electron. Syst.*, vol. 48, no. 1, 2012.

[39] Y.D. Zhao, Y.K. Zhao, X.D. Lu, and M.S. Xiang, "Block NLMS cancellation algorithm and its real-time implementation for passive radar," *IET International Radar Conference 2013*, April 2013.

[40] B. Demissie, "Clutter cancellation in passive radar using GSM broadcast channels," *IET Radar, Sonar & Navigation*, vol. 8, no.7, Aug. 2014.

[41] Guan Xin, Hu Dong-hui, Zhong Li-hua, and Ding Chi-biao, "Strong Echo Cancellation Based on Adaptive Block Notch Filter in Passive Radar," *IEEE Geoscience and Remote Sensing Letters*, vol. 12, no. 2, Feb. 2015.

[42] Z. Zhao, X. Wan, Q. Shao, Z. Gong, and F. Cheng, "Multipath clutter rejection for digital radio mondiale-based HF passive bistatic radar with OFDM waveform," *IET Radar, Sonar & Navigation*, vol. 6, no. 9, Dec. 2012.

[43] M. John, M. Inggs, and D. Petri, "Real time processing of networked passive coherent location radar system," International Journal of Electronics and Telecommunications, vol. 57, no. 3, 2011.

[44] M.R. Inggs and C.A. Tong, "Commensal radar using separated reference and surveillance channel configuration", *Electronics Letters*, vol. 48, no. 18, 2012.

[45] H.-W. Li and J. Wang, "Particle filter for manoeuvring target tracking via passive radar measurements with glint noise," *IET Radar, Sonar and Navigation*, vol. 6, no. 3, 2012.

[46] Zhixin Zhao, Xianrong Wan, Delei Zhang, and Feng Cheng, "An Experimental Study of HF Passive Bistatic Radar Via Hybrid Sky-Surface Wave Mode," *IEEE Transactions on Antennas and Propagation*, vol. 61, no. 1, Jan. 2013.

[47] D.K.P. Tan, M. Lesturgie, H. Sun, and Y. Lu, "Space–time interference analysis and suppression for airborne passive radar using transmissions of opportunity," *IET Radar, Sonar & Navigation*, vol. 8, no. 2, Feb. 2014.

[48] L. Xiao-Yong, W. Jun, and W. Jue, "Robust direction of arrival estimate method in FM-based passive bistatic radar with a four-element Adcock antenna array," I*ET Radar, Sonar and Navigation*, vol. 9, no. 4, 2015.

[49] H. Wang, J. Wang, and L. Zhong, "Mismatched filter for analogue TV-based passive bistatic radar," *IET Radar, Sonar and Navigation*, vol. 5, no. 5, 2011.

[50] R. Zemmari, M. Broetje, G. Battistello, and U. Nickel, "GSM passive coherent location system: Performance prediction and measurement evaluation," *IET Radar, Sonar and Navigation*, vol. 8, no. 2, 2014.

[51] J. Brown, K. Woodbridge, H. Griffiths, A. Stove, and S. Watts, "Passive bistatic radar experiments from an airborne platform," *IEEE Aerospace and Electronic Systems Magazine*, vol. 27, no. 11, 2012.

[52] F. Colone, C. Bongioanni, and P. Lombardo, "Multi-Frequency Integration in FM Radio Based Passive Bistatic Radar. Part II: Direction of Arrival Estimation," *IEEE Aerospace and Electronic Systems Magazine*, vol. 28, no. 4, 2013.

[53] H. Kuschel, M. Ummenhofer, P. Lombardo, F. Colone, and C. Bongioanni, "Passive radar components of ARGUS 3D," *IEEE Aerospace and Electronic Systems Magazine*, vol. 29, no. 3, March 2014.

[54] F. Colone, P. Falcone, C. Bongioanni, and P. Lombardo, "WiFi-Based Passive Bistatic Radar: Data Processing Schemes and Experimental Results," *IEEE Trans. on Aerospace and Electronic Systems*, vol. 48, no. 2, April 2012.

[55] D. Pastina, F. Colone, T. Martelli, and P. Falcone, "Parasitic Exploitation of Wi-Fi Signals for Indoor Radar Surveillance," *IEEE Trans. on Vehicular Technology*, vol.64, no. 4, April 2015.

[56] G. H. Golub and C. F. Van Loan, "Matrix Computations (3rd ed.)," Johns Hopkins University Press, Baltimore, MD, 1996.

[57] C. Palmarini, F. Colone, P. Lombardo and E. Tilli, "Block based channelization technique for Delay-Doppler map evaluation in passive radar," *2015 16th International Radar Symposium (IRS)*, Dresden, 2015, pp. 65-70.

[58] D. Poullin and M. Flecheux, "Passive 3D tracking of low altitude targets using DVB (SFN Broadcasters)," in *IEEE Aerospace and Electronic Systems Magazine*, vol. 27, no. 11, pp. 36-41, November 2012.

[59] F. Athley, "Threshold region performance of maximum likelihood direction of arrival estimators," in *IEEE Transactions on Signal Processing*, vol. 53, no. 4, pp. 1359-1373, April 2005.

[60] D. W. O'Hagan, H. Kuschel, J. Heckenbach, M. Ummenhofer and J. Schell, "Signal reconstruction as an effective means of detecting targets in a DAB-based PBR," *11-th INTERNATIONAL RADAR SYMPOSIUM*, Vilnius, Lithuania, 2010, pp. 1-4.

[61] http://www.nvidia.com/object/what-is-gpu-computing.html

[62] http://www.eetimes.com/document.asp?doc_id=1275354

LIST OF PUBLICATIONS

1. Macera A., Bongioanni C., Colone F., Palmarini C., Martelli T., Pastina D., Lombardo P., "*FM-based Passive Bistatic Radar in ARGUS 3D: Experimental results*", Annual Meeting of the Italian Group of Telecommunications and Information Technologies - Gtti 2013, Ancona, Italy, June 24-26, 2013

2. Palmarini, C.; Colone, F.; Lombardo, P.; Tilli, E., "*Block based channelization technique for Delay-Doppler map evaluation in passive radar*," in Radar Symposium (IRS), 2015 16th International , vol., no., pp.65-70, 24-26 June 2015

3. Marongiu, V.; Palmarini, C.; Pastina, D.; Colone, F.; Lombardo, P., "*VHF cross-range profiling of aerial targets via passive ISAR: Preliminary experimental results*," in Radar Symposium (IRS), 2015 16th International , vol., no., pp.83-88, 24-26 June 2015

4. C. Palmarini, T. Martelli, F. Colone and P. Lombardo, "*Disturbance removal in passive radar via sliding extensive cancellation algorithm (ECA-S)*," *2015 IEEE Radar Conference*, Johannesburg, 2015, pp. 162-167.

5. F. Colone, C. Palmarini, T. Martelli and E. Tilli, "Sliding extensive cancellation algorithm for disturbance removal in passive radar," in *IEEE Transactions on Aerospace and Electronic Systems*, vol. 52, no. 3, pp. 1309-1326, June 2016.

6. Technical Report for Selex-ES, "*Radar passivi PCL in banda DVB-T per la rivelazione ed il tracciamento di bersagli navali*", 2015